THE UNIVERSITY OF WARWICK

Development and Application of Pipet-Based Electrochemical Imaging Techniques

Neil Ebejer

A thesis submitted for the degree of Doctor of Philosophy

The University of Warwick, Chemistry Department

September 2012

Nixtieq niddedika dan it-teżi lil familja tiegħi

Table of Contents

List of figures

List of tables

Acknowledgements

I would like to thank Professor Patrick Unwin, for his great supervision, guidance and importantly his patience. He has made my project truly enjoyable and I am really grateful for all the times I was pushed and steered in the right direction, none of this would have been possible without him. I would also like to thank Professor Julie Macpherson for her helpful discussions and supervision, providing criticism which I now truly appreciate.

I would laike to thank everyone on the Warwick Electrochemistry and Interfaces group for making my time here such an enjoyable one. We have had alot of laughs and experiences which I will never forget.

I thank Paul Kirkman and Robert Lazenby, for all the fun times and joking around, but also for always being around when no one else was. James Iacobini and Tom Miller thank you for your endless humour and for all the enjoyable times both at work and socially. Dr. Stanley Lai should be noted for his patience and for bringing stroopwafels. I would laike to thank Jon Newland for our endless gaming nights and helpful advice with photography and Dr. Petr Dudin for all the fun times.

I would especially like to thank Dr. Aleix Güell for mentoring me throughout the last few years. He has been a great source of inspiration, a fountain of knowledge when having scientific discussions and most importantly a great friend.

I would like to thank my sponsors at NPL, most notably Dr. Andy Pollard and Dr. Charles Clifford who were very helpful and welcoming, during my internship.

Last but not least, I would like to thank my parents for their constant support and for believing in me. I would also like to thank my sister Sarah who was always there when I needed a break, have a good laugh and alot of fun.

Declaration

I declare that thesis consists of my own work except the following collaborations: *i*) Chapter 3. Simulations were carried out by Dr. Michael E. Snowden and experimental data was perfomed jointly with Dr. Aleix G. Güell. *ii*) Chapter 4. The synthesis and characterisation of the graphene samples were performed by Dr. Aleix G. Güell and the simulations were performed by Dr. Michael E. Snowden. *ii*) Chapter 5. SWNT forest samples were synthesised and characterised by Mr. Thomas S. Miller and the 2D SWNT networks were synthesised and characterised by Dr. Aleix G. Güell and the simulations were performed by Dr. Michael E. Snowden.

I declare that this thesis has not been submitted for a degree at any other university.

Parts of this thesis have appeared in the following publications:

Chapter 1 - Scanning Electrochemical Cell Microscopy – N. Ebejer, A. G. Güell, S. C. S. Lai, K. McKelvey, M. E. Snowden, P. R. Unwin - *Annu. Rev. Anal. Chem* (submitted)

Chapter 3 - Localized High Resolution Electrochemistry and Multifunctional Imaging: Scanning Electrochemical Cell Microscopy - N. Ebejer, M. Schnippering, A. W. Colburn, M. A. Edwards & P. R. Unwin, *Anal. Chem.,* **2010**, 82 (22), 9141-9145.

Chapter 3 - Scanning Electrochemical Cell Microscopy (SECCM): Theory and Experiment for Quantitative High Resolution Spatially-Resolved Voltammetry and Simultaneous Ion-Conductance Measurements – M. E. Snowden, A. G. Güell, S. C. S. Lai, K. McKelvey, N. Ebejer, Michael A. O'Connell, Alex W. Colburn, and Patrick R. Unwin, *Anal. Chem.,* **2012**, 84 (5), 2483-2491.

Chapter 4 - Structural Correlations in Heterogeneous Electron Transfer at Monolayer and Multilayer Graphene Electrodes – A. G. Güell, N. Ebejer, M. E.

Snowden, J. V. Macpherson, P. R. Unwin, *J*. *Am*. *Chem*. *Soc*., **2012**, 134 (17), 7258-7261. 6.

Chapter 5 - Nanoscale Visualization of Heterogeneous Electron Transfer Rates in 2-D carbon nanotube networks – A. G. Güell, N. Ebejer, M. E. Snowden, K. McKelvey, J. V. Macpherson, P. R. Unwin – *Proc*. *Natl*. *Acad*. *Sci*. *USA*, **2012**, *109*, 11487

Chapter 5 - Electrochemistry at Carbon Nanotube Forests: Sidewalls and Closed Ends Allow Fast Electron Transfer – T. S. Miller, N. Ebejer, A. G. Güell, J.V. Macpherson, P. R. Unwin – *Chem*. *Comm*., **2012**, *48*, 7435

Chapter 6 - Multifunctional Nanoprobes for Nanoscale Chemical Imaging and Localized Chemical Delivery at Surfaces and Interfaces - Y. Takahashi, A. I. Shevchuk, P. Novak, Y. Zhang, N. Ebejer, J. V. Macpherson, P. R. Unwin, A. J. Pollard, D. Roy, C. A. Clifford, H. Shiku, T. Matsue, D. Klenerman and Y. E. Korchev, *Angew*. *Chem*. *Intl*. *Ed*, **2011**, 50 (41), 9638-9642.

Abstract

This thesis describes the development of an electrochemical scanned probe microscope, SECCM, outlining the need for such a development, by highlighting previous techniques and their limitations. SECCM consists of a double barrel capillary pulled to small dimensions, filled with electrolyte solution and a redox mediator of choice, with a QRCE is inserted into each channel. A potential is applied between the QRCEs, whilst modulating the pipet normal to the surface. The probe is translated towards the surface and once contact is established, a modulation in the ion current arises due to the physical oscillation of the probe, which is then used as a feedback parameter for imaging. The potential at the working electrode substrate is also controlled. SECCM is introduced using a model test substrate, gold bands on glass, showing that the probe is able to track topographical features, making simultaneous electrochemical measurements. Ion conductance measurements between the two QRCEs, are shown to be sensitive to the nature of the substrate investigated. The fundamental electrochemical behaviour of CVD graphene and SWNT is investigated. A multimicroscopy approach is used for CVD graphene studies, correlating surface structure and activity, deducing heterogeneous electron transfer kinetics through simulation. The SWNT samples are studied in two different morphologies: as 3D forests; and, as a 2D network. In the forests, the probe is positioned at the ends and sidewalls, making spot measurements. The voltammetric behaviour shows very similar responses, whilst in the network, a nanosized probe is scanned across the surface, showing relatively uniform activity across an entire tube. These new insights indicate that SWNTs are highly active electrode materials. The fabrication and characterisation of SECM-SICM probes, in a straightforward manner is also presented. These types of probes were found to be ideal for the investigation of biological samples, being extremely easy and quick to fabricate.

Abbreviations

ADC	analog to digital converter
AC-SECM	alternating current – scanning electrochemical microscopy
AFM	atomic force microscopy
CNT	carbon nanotube
CPU	central processing unit
CV	cyclic voltammetry
CVD	chemical vapour deposition
DAC	digital to analog converter
DAQ	data acquisition
DBCNP	dual barrel carbon nanoprobe
EC-STM	electrochemical scanning tunnelling microscopy
ET	electron transfer
FE-SEM	field emission – scanning electron microscope
FIB	focussed ion beam
FPGA	field programmable gate array
GUI	graphical user interface
HET	heterogeneous electron transfer
HOPG	highly oriented pyrolytic graphite
IC-SECM	intermittent contact scanning electrochemical microscopy
LIA	lock-in amplifier

LSV	linear sweep voltammogram
LUMO	lowest unoccupied molecular orbital
MWNT	multiwalled carbon nanotube
NP	nanoparticle
NSOM	near field scanning optical microscopy
PC	personal computer
QRCE	quasi reference-counter electrode
SECCM	scanning electrochemical cell microscopy
SECM	scanning electrochemical microscopy
SECM-AFM	scanning electrochemical microscopy – atomic force microscopy
SECM-SICM	scanning electrochemical microscopy – scanning ion conductance microscopy
SECM-STM	scanning electrochemical microscopy – scanning tunnelling microscopy
SEM	scanning electron microscope
SG-TC	substrate generation – tip collection
SICM	scanning ion conductance microscopy
SMCM	scanning micropipette contact method
SPM	scanned probe microscopy
STM	scanning tunnelling microscopy
SWNT	single walled carbon nanotube
TEM	transmission electron microscopy
TG-SC	tip generation – substrate collection

TPM-SECM	tip position modulation – scanning electrochemical microscopy
UME	ultramicroelectrode
VI	virtual instrument

CHAPTER 1

Introduction

This thesis is concerned with the invention of a novel electrochemical scanned probe technique. To put the work into context, this introductory chapter provides a brief overview of dynamic electrochemistry and electrochemical methods and highlights some of the main previous methods used for electrochemical imaging. Technical features, attributes and limitations are identified from which a new electrochemical imaging technique, termed SECCM, is proposed.

1.1 Dynamic Electrochemistry

Dynamic electrochemistry, generally, refers to the study of charge transfer processes at electrode surfaces with reactant molecules. A number of factors are known to influence the dynamics of an electrochemical reaction and the rate of charge transfer processes, these being; electrode potential, mass transport of species towards the electrode, reactivity of the molecule under investigation, the activity of the electrode material and the structure of the interfacial region where electron transfer occurs,[1] shown in Figure 1-1.

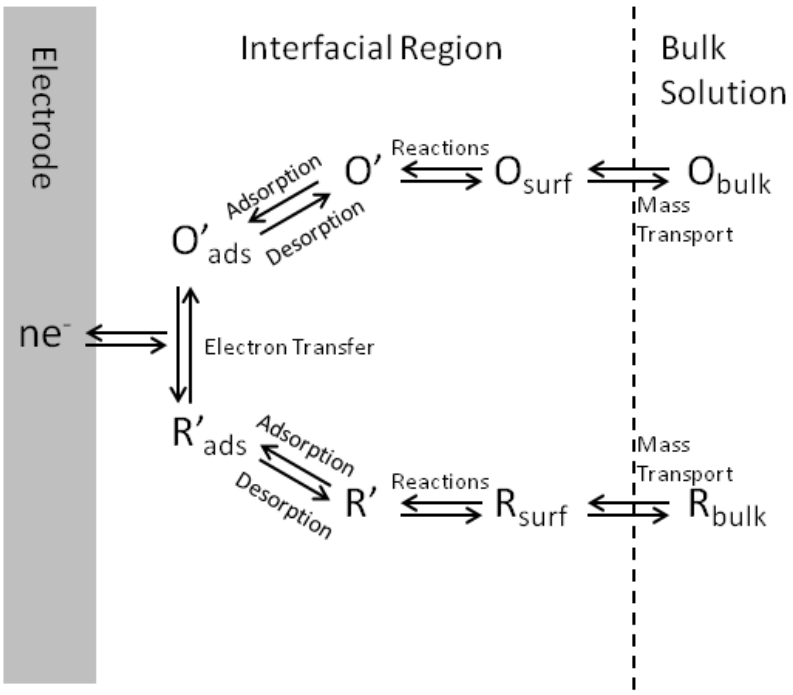

Figure 1-1: *A schematic of the processes undergone in basic dynamic electrochemistry*

1.1.1 Electron transfer at the electrode

In an electrode material, which is usually metallic, the overlap of atomic orbitals allows for electrons to move freely within the crystal lattice. These electrons occupy a number of energy levels with a maximum state known as the Fermi level. The position of the Fermi level can be tuned using an electric potential, either increasing or decreasing the energy. Electron transfer from an electrode to a reactant molecule only occurs if the Fermi level in the electrode material, is at a higher energy than the lowest unoccupied molecular orbital (LUMO) of the electroactive species.[1]

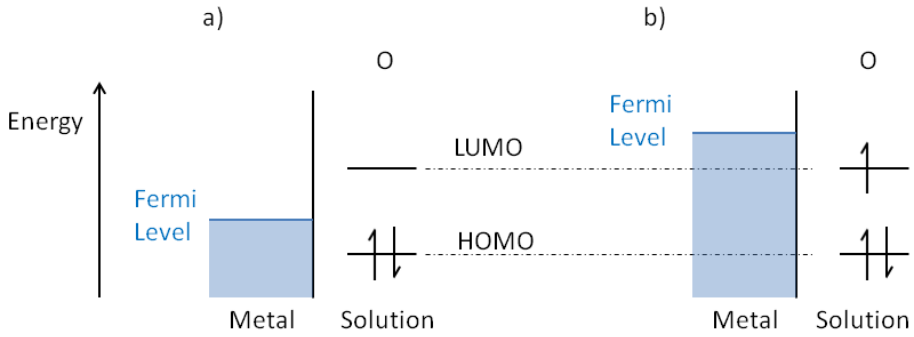

Figure 1-2: *Energy level diagram. In case a) there is insufficient energy to reduce species, O, by tuning the Fermi level with an applied potential there is now sufficient energy for electron transfer between the metal electrode and O to occur as in case b).*

For a system at equilibrium depicted in equation 1.1, the Nernst equation (1.2), can be used to relate potential to the concentration of the molecule being oxidised or reduced.[2]

$$O + ne^- \rightleftharpoons R \qquad 1.1$$

$$E = E^{0'} - \frac{RT}{nF} \ln \frac{a_R}{a_O} \qquad 1.2$$

$$a = \gamma c \qquad 1.3$$

Where E is the potential at the electrode, $E^{0'}$ is the standard electrode potential, R is the molar gas constant, F is Faraday's constant, n is the number of electrons transferred determined form the stoichiometry of the reaction in equation 1.1, a is the activity of the species defined by the activity coefficient γ and the concentration c of the species.[2]

None of the systems studied in dynamic electrochemistry are at equilibrium, but in some instances electron transfer kinetics are so fast that the response will be governed by mass transport. In this case it is reasonable to assume Nernstian behaviour or reversible kinetics at the electrode surface.

When Nernstian behaviour no longer holds at the electrode and electron transfer kinetics dominate, the simplest relationship is that defined by Butler and Volmer and so the rate of the forward reaction k_f and backward reaction k_b are defined in equations 1.5 and 1.6.

$$O + ne^- \underset{k_b}{\overset{k_f}{\rightleftharpoons}} R \qquad 1.4$$

$$k_f = k^0 \exp\left(\frac{-\alpha nF(E - E^{0'})}{RT}\right) \qquad 1.5$$

$$k_b = k^0 \exp\left(\frac{(1-\alpha)nF(E - E^{0'})}{RT}\right) \qquad 1.6$$

where k^0 is the standard rate constant, α is the electron transfer coefficient, with the remaining variables being previously defined. The equations defined arise from transition state theory and are used most in electrochemistry for the analysis of electrode kinetics. Although more complex models are available they were not considered in this work.[2]

1.1.2 Mass transfer

In the context of the work herein, mass transfer describes the motion of species in solution, and particularly between bulk solution and an electrode surface. It can arise from differences in electrical or chemical potentials, or from the physical

motion of a portion of solution. Thus, the variants of mass transfer can be categorised into diffusion, migration and convection. It is the combination of all three processes which governs the overall mass transfer and can be described by the Nernst-Planck equation.[2]

$$J_i = J_{i,d} + J_{i,m} + J_{i,c} = -D\nabla C_i - \frac{z_i F}{RT} D_i C_i \nabla \phi + C_i \underline{v} \qquad 1.7$$

$J_{i,d}$, $J_{i,m}$ and $J_{i,c}$ denote the diffusive, migrative and convective components of the flux of species i; D_i represents the diffusion coefficient; C_i represents the concentration; z_i represents the charge on the species; ϕ represents the electric potential; v is the velocity of the solution; T is the absolute temperature and the other terms have been defined. Mass transfer will be described in more detail in the following sections.

1.1.2.1 Diffusion

Diffusion occurs due to thermal movement of species in solution for both charged and neutral species.[1] The rate of net diffusion depends on the concentration profile at a specific location and can be described by Fick's first 1.8 and second 1.9 laws.[2]

$$J_{i,d} = -D\nabla C_i \qquad 1.8$$

$$\frac{\partial C_i}{\partial t} = D_i \nabla^2 C_i \qquad 1.9$$

The first law describes the net flux in terms of a concentration gradient, within a system, towards an electrode, considering the variation in concentration in a specific location within a specific time. Equation 1.8 has a negative sign because species move from a region of high concentration to regions with a lower one. The second law merges the general conservation equation with the first law, which describes the variation in concentration with time due to diffusion.[1] This is the equation that is normally solved to predict the current at an electrode.

The driving force for diffusion of species within a solution is the gradient in chemical potential of the species, Fick's first law can be rearranged to yield and describes the case where the species is electrically neutral:[2]

$$J_i = -\frac{D_i C_i}{RT} \nabla \mu_i \qquad 1.10$$

$$\mu_i = \mu_i^{\alpha} + RT \ln a_i \qquad 1.11$$

where μ_i is the chemical potential of the species, μ_i^{α} is the standard chemical potential in phase α and all other variable have been previously defined. For charged species the electrochemical potential is given as:

$$\bar{\mu}_i^{\alpha} = \mu_i^{\alpha} + z_i F \phi^{\alpha} \qquad 1.12$$

Where $\bar{\mu}_i^{\alpha}$ is the electrochemical potential and all other parameters have been previously defined.[2]

1.1.2.2 Migration

Migration refers to the movement of charged species due to a potential gradient exerted by an electric field existing at the electrode solution interface. This exerts an electrostatic force on charged species within solution pushing ions towards or away from the electrode. The migratory flux is described in equation 1.12 and is dependent on ion mobility, concentration of the ion and the electric field.

$$J_m = -\frac{z_i F}{RT} D_i C_i \nabla \phi \qquad 1.12$$

The term $\frac{z_i F}{RT} D_i$ describes the mobility of the ion and is usually denoted as u_i.[2]

1.1.2.3 Convection

Convection occurs due to mechanical forces acting on the solution, causing motion in the fluid. There are two types of convection: natural which arises, for example, from thermal gradients within the solution and / or variations in density; and forced which arises from stirring or pumping of the solution.[1] The convective flux of a species, *i*, in solution is given by the equation:

$$J_{i,c} = C_i \underline{v} \qquad 1.13$$

1.1.3 Experimental electrochemistry

1.1.3.1 Macro electrodes

Macroelectrodes are ones which have dimensions from the millimetre to the centimetre range. Due to its large size these electrodes experience planar diffusion fields shown in Figure 1-3 and also due to the large currents passed, greater than 1

µAmp, they have to be used in a 3 electrode configuration where the counter electrode compensates for Ohmic drop in solution.

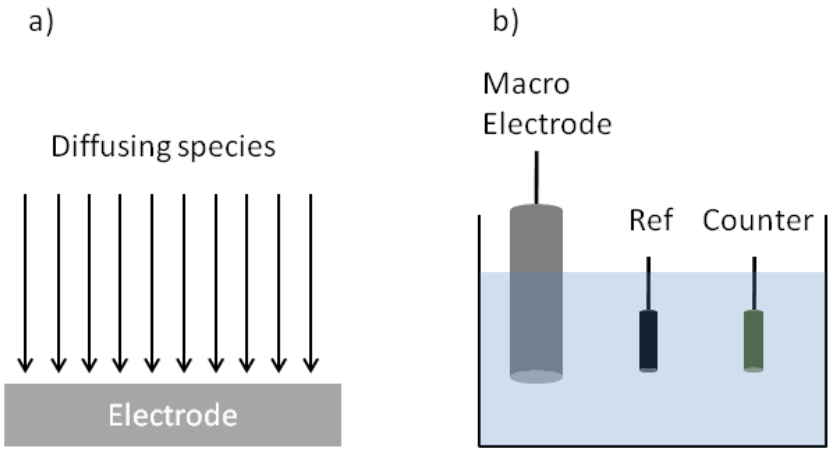

Figure 1-3: *a) shows the linear diffusion profile towards a macroelectrode and b) shows a 3 electrode system where ref is the reference electrode and counter is the counter electrode bathed in solution and connected to a potentiostat.*

1.1.3.2 Cyclic Voltammetry

Cyclic voltammetry (CV) utilizes a potential scanned backed and forth between two preset potentials, E_1 and E_2 at a steady scan rate v / Vs^{-1}. This gives a triangular waveform, shown in Figure 1-4:

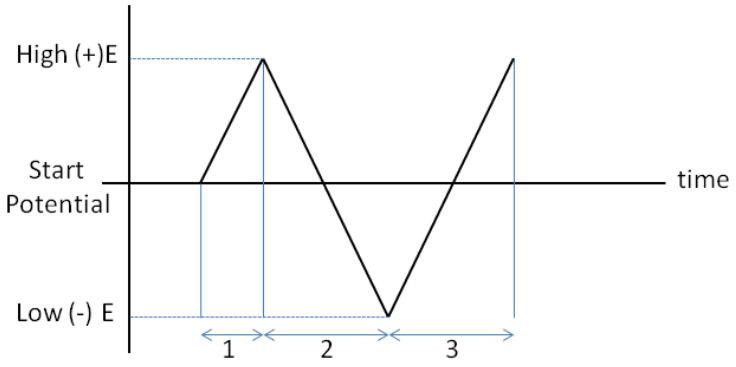

Figure 1-4: *A typical waveform for a CV broken up into segments. The cycle goes from a negative potential to a positive one and vice versa.*

Experiments are usually conducted in stationary solutions and hence rely on the diffusion of the reactants. This can be determined by Fick's second law shown in equation 1.9, for a species *i*.

Cyclic voltammetry is the most widely used technique for the characterisation of redox systems[1]. It provides qualitative information about the number of oxidation states and their stability,[1] also giving information about surface reaction mechanisms.

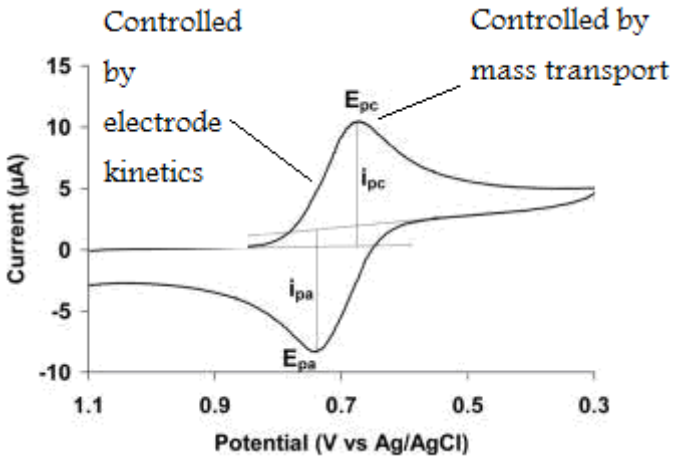

Figure 1-5: *Initially the chemical reaction is governed by kinetics of the heterogeneous electron transfer across the electrode / solution interface. At the maximum the current response is due to diffusion.*[1]

The shape of the voltammogram depends on the reversibility of the redox couple, and/or the electrostatic repulsive or attractive forces between the redox centres (the voltammogram described here is only valid for a macroelectrode). The peaks in the voltammogram occur because mass transport cannot compete with electrode kinetics and so a depletion of species occurs.

1.1.3.3 Amperometry

Amperometry is defined as the measurement an electrical current or a change in electrical current, with an applied, fixed potential.[2] In this case a fixed dc potential is applied to the working electrode, with respect to a reference electrode, and a net current flows due the oxidation or reduction of an electroactive species. This technique is commonly used in electrochemical titration methods and is described elsewhere.[2]

1.1.3.4 Potentiometry

In a potentiometric experiment no net current flows, *i.e*. no electrochemical (Faradaic) reaction occurs. The measured potential is usually dependent on the thermodynamics of the system, but not always[2] and is used to determine the concentration of an analyte in solution. This analytical method is the basis for ion selective electrodes.[2]

1.2 Scanning Electrochemical Microscopy (SECM)

SECM is a completely different means of performing dynamic electrochemistry.[3] The technique is based on the utilization of a mobile ultramicroelectrode (UME), placed in close proximity to a surface, which can provide quantitative information on interfacial physicochemical processes.[3,4] A UME can be used either as a potentiostatic or potentiometric probe, to determine the properties of a sample interface. The type of electrode used depends on the process being investigated. In amperometry, where a target species is consumed or generated

by electrolysis, the probe can be used to induce and monitor a specific interfacial process, or simply to detect a particular species involved in an interfacial process.[4-5] If the SECM measurement involves a non-invasive detection process, then potentiometry also becomes a possibility, greatly extending the range of species and processes that can be investigated.[6] The use of a UME greatly improves the spatial resolution and implementation of electrochemical techniques, and allows for investigation of activity and topography at an interface at a localized scale.[4,7-9] Due to the dimensions of the UME (typically a disc electrode of 25 μm diameter or smaller), it is also possible to minimize the influence of many sources of experimental errors, namely, resistive potential drops in solution and charging currents. This allows for scrutinous investigation of minute electrochemical processes (with currents normally in the nA - pA range), such as ion exchange reactions at polymer – electrolyte interfaces[10-11] and immobilized enzymes.[3,7,12-15] The investigation of biological samples is a common application for SECM, being able to monitor activity[4,12] also attempting to perform topographical imaging, which is a major challenge.[7, 8] Figure 1-6 shows the information which can be extracted from amperometric UME used in SECM. The arrows represent the flux of electrochemically active species towards the probe.

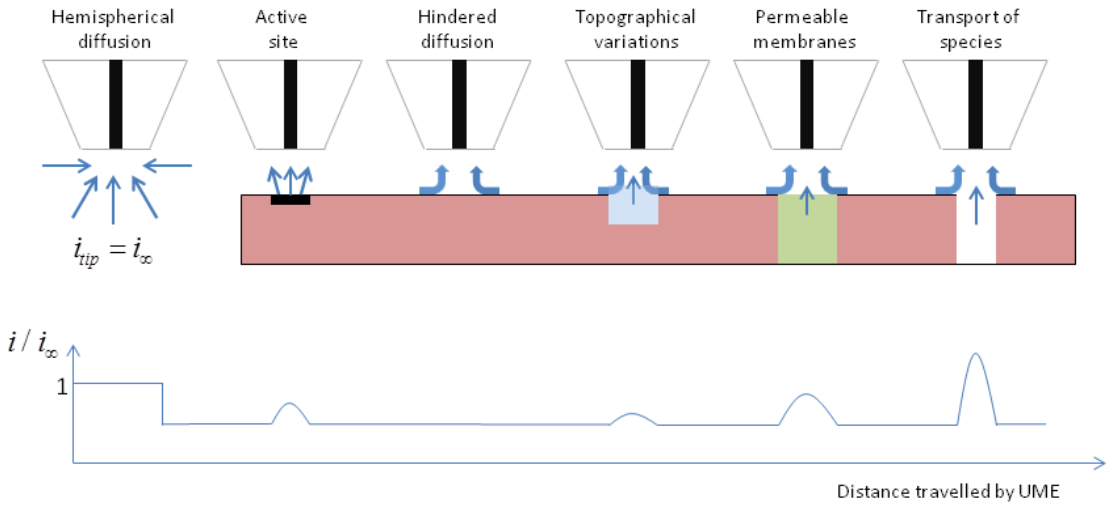

Figure 1-6: *Schematic of the varied modes of application of SECM (top) and the current response observed in each (bottom), as normalised by the current far from the surface.*

1.2.1 Instrumentation

The basic elements of an SECM setup are depicted in Figure 1-3 and will be discussed in the following sections.

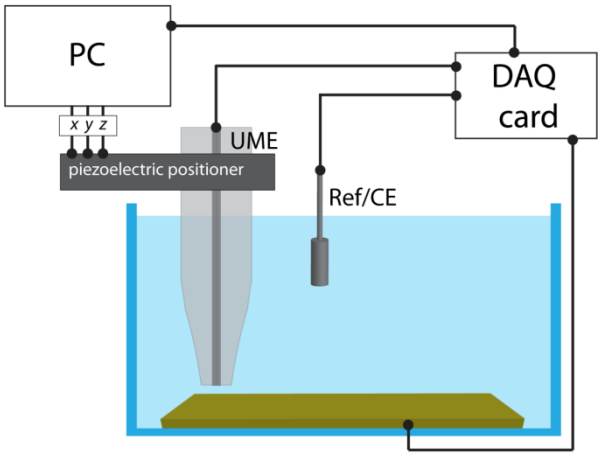

Figure 1-7*: A schematic of an SECM rig.*

1.2.1.1 Ultramicroelectrodes (UMEs)

Several definitions of a UME are available such as: 'an electrode which is smaller than the scale of the diffusion layer in readily achievable experiments,[16] and 'experimentally a UME can be defined as an electrode having at least one dimension, the critical dimension, less than 100 μm.[16] In essence a UME is one which shows non – linear (edge) diffusion on the time scale of a typical voltammetric experiment, which puts the length scale in the range identified in these definitions. Unlike macroelectrodes UMEs are usually used in a 2 electrode arrangement (Figure 1-7) due to the magnitudes of currents passed are usually on the nAmp range or less, in this case Ohmic drop is considered negligible. In depth reviews on electrode design, fabrication and characterization can be found elsewhere.[16-17] The most common mode of preparation of a UME involves the thermal sealing of a metal wire in a glass capillary, yielding a disc shaped electrode of typical diameter 0.6 μm to 100 μm (refer to Figure 1-8 for UME images).

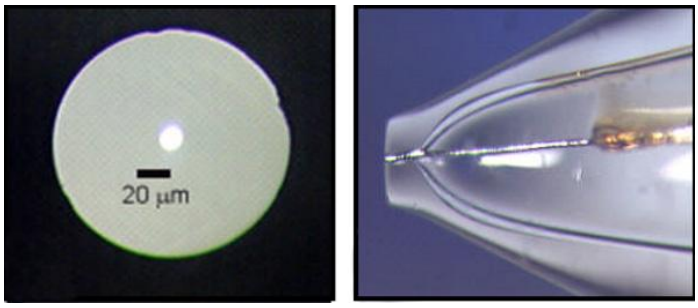

Figure 1-8: *Optical microscope images of a UME from an end on view and side view.*[16]

The term RG defines the ratio of the surrounding insulator dimension to that of the tip and is usually about 10. This ratio is chosen as it minimizes effects from back diffusion enabling the response to be more sensitive to surface processes[9]. As briefly highlighted when used in SECM, mass transport at UMEs is multi-

dimensional diffusion, than linear diffusion (as experienced by macroelectrodes). This also means that the diffusional flux at an UME is greater than that for larger electrodes for equivalent conditions (e.g. scan rate).[16] This feature can be attributed to the size and geometry of the electrode and the resulting diffusion pattern shown in Figure 1-9.

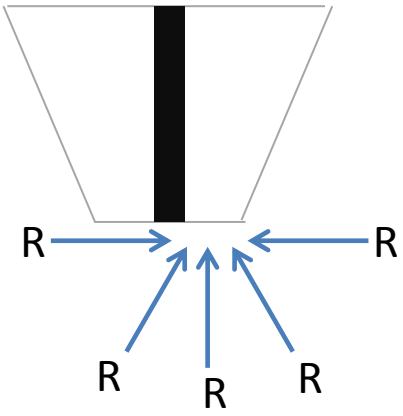

Figure 1-9: *Schematic of a hemispherical diffusion field established for the steady state diffusion-limited oxidation of a bulk solution species.*

1.2.1.2 Probe positioning

A key feature of SECM is that the electrode is connected to a piezoelectric stage, allowing motion control in the x, y, and z directions.[4] In many cases nanometer scale precision is possible depending on the type of piezoelectric positioner used, similar to those used in scanning tunnelling microscopy (STM).[18] For SECM, the greatest precision is required in positioning the z direction, i.e. in the electrode approach to the surface. The piezoelectric positioners are typically controlled by a high voltage amplifier receiving a signal from a control card converting the signal via a digital to analogue converter. Initial positioning (lower resolution) is often achieved via manual micrometer stages. A video microscope is

sometimes used, in order to facilitate tip approach, allowing the initial approach to the surface to be achieved via the manual control.[19-20]

1.2.1.3 Signal generating / acquiring devices.

In most cases, the signal detected in SECM is a current. This is converted to a voltage via a current to voltage converter and then amplified, with gain settings calibrated to a specific range of values. For the investigation of unbiased surfaces with SECM, a typical two electrode system (a working electrode and a reference electrode) is sufficient to bias the tip to initiate an electrochemical process. In cases where the surface also requires biasing externally, a bipotentiostat is used to control the system. All signals are then acquired via a data acquisition card and processed in specific host software, generating a visual depiction of interfacial processes.

1.2.2 Modes of operation

1.2.2.1 Feedback mode

The feedback mode is the main mode used in SECM and it includes detecting a species by electrolysis at a diffusion limited rate. Figure 1-10 shows the variation in electrochemical response with respect to the substrate. It must be noted that the term feedback mode should not be confused with positional feedback as in conventional scanned probe techniques as SECM, has no positional feedback. If the UME is approaching an insulating surface, the diffusion of redox species towards the active area of the microelectrode will be blocked by the surface. This means that the hemispherical diffusion field established at the UME is distorted by the insulating surface. The blockage of diffusion towards the UME leads to a depletion of species

available for the conversion and hence the current measured at the microelectrode drops.[21] This phenomenon is known as 'negative feedback'.

In the case of approaching a conducting substrate, the electroactive species now encounters a surface whereby electron transfer may occur. In this mode, the tip is held at a potential, initiating the diffusion-controlled electrolysis of a target species in solution (this is also performed during negative feedback). This, in turn, experiences positive diffusional feedback when positioned close to a conductor, due to the substrate sometimes following Nernstian behaviour (in some cases it is necessary to apply a bias to the electrode) , such that the direction of the tip electrode reaction is reversed on its surface, thereby increasing the overall current measured.[22] Essentially the equilibrium, disturbed by the SECM tip will tend towards being re-established by the Nernst potential of the surface to re-convert the species converted at the tip and will therefore increase the current at the tip since no depletion of convertible species happens[21]. The same processes are undergone for any sample being investigated and a more detailed description can be found in literature.[4-5,10,12-14,23-24]

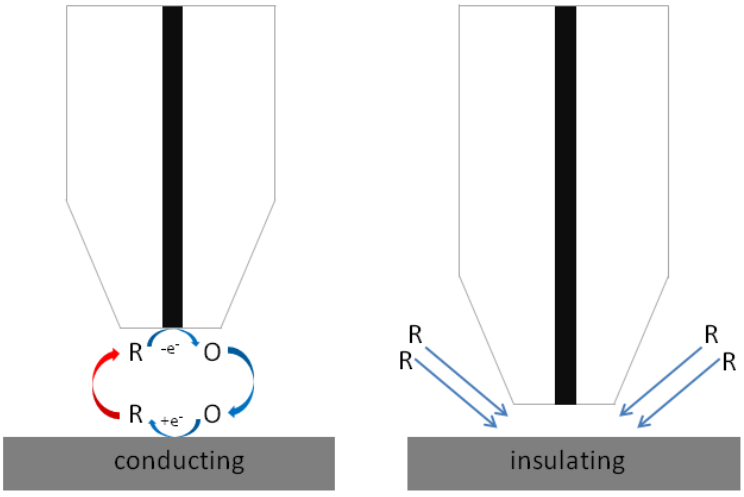

Figure 1-10: *A schematic of SECM operating in feedback mode when encountering a conducting and insulating substrate.*

1.2.2.2 Generator collector mode

There are many other SECM operative modes among which generation / collection modes[4-5,25-26] are most prominent. In substrate generation – tip collection (SG-TC) one detects species emerging from a surface as a tip current and in tip generation – substrate collection (TG-SC) a species is generated at the tip and detected as a current at the surface (shown in Figure 1-11).[4] For example, if electroactive species diffuse through a pore opening or from a sample surface, they can be converted by the SECM tip if it is held at a suitable potential,[4-5] determining the activity at that specific location, on the other hand species can be generated at the tip and collected at the surface[5]. These methods are designed to compensate for the different effects observed in each case. Specific details of technique variations can be found elsewhere. [4-5]

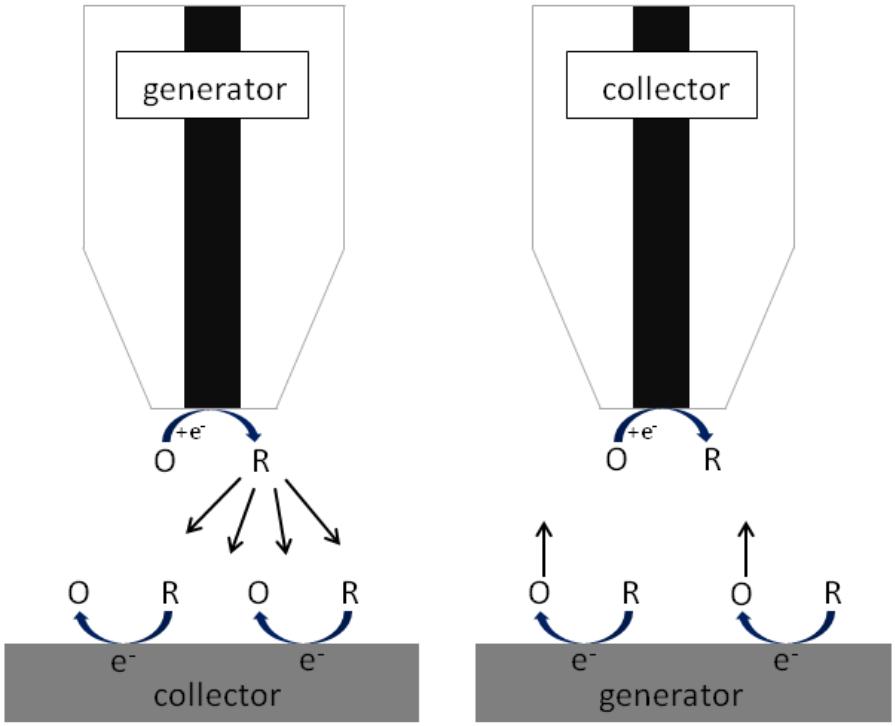

Figure 1-11: *SECM operating in generator collector mode*.

1.2.2.3 Permeability and ion transport at interfaces

SECM can be used to monitor or perturb interfacial processes by use of an amperometric probe. In the general case the UME immersed in a liquid phase and is in close proximity to a secondary phase, for example an immiscible liquid, gas or a biological membrane, with the process being studied initially at equilibrium.[20,27] A potential is applied to the probe oxidising the species in phase 1, driving the transfer of reduced species in phase 2 across the interface. An enhancement in tip current is observed and the reduced species reaches the tip via hindered diffusion through phase 1. This response is governed by diffusion in the two phases and the interfacial kinetics.[20] Even though this method has been used mostly with metal electrodes, liquid-liquid voltammetric probes can also be used as a study of ion transfer across interfaces. This method has proved useful in determining solute transfer across biological membranes and bathing solution, as a non invasive method.[27-29]

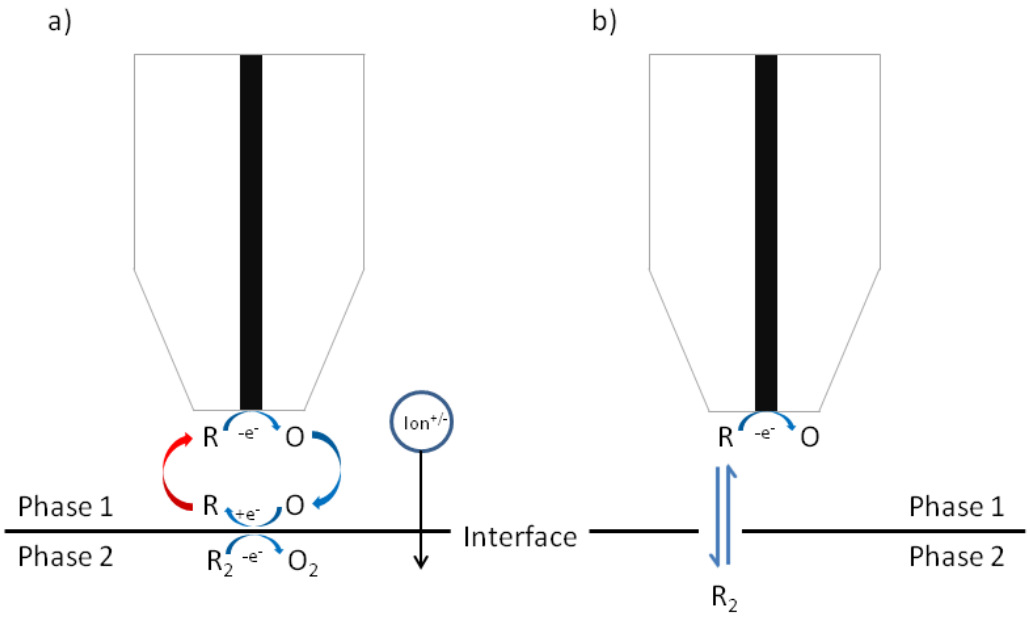

Figure 1-12: *Inducing an interfacial process using feedback mode a) monitoring induced transfer b).*

1.2.2.4 Pipet based liquid / liquid interface probes

The tips used here comprise of pulled glass or quartz pipets and the tip current is due to either facilitated[30] or simple ion transfer[31] across a liquid/liquid interface, in most cases an aqueous / organic (inside the pipet) interface.[5] These pipets are usually polished.[32] Due to the ease of preparation, compared to traditional SECM electrodes, pipets with radii less than 10 nm have been reported.[33] Similar to negative feedback mode with traditional SECM electrodes, when over a solid substrate ion transfer across the solution interface is hindered and leads to a decrease in tip current.[5] Enhancements in tip current indicate additional ion flux from the substrate and examples include ion transport measurements through porous silicon membranes[34] as well as the effects of silver ions in living cells.[30] When compared to the response of traditional platinum electrode a similar response was obtained with a liquid-liquid probe over a silicon wafer in constant current mode,[31] indicating that this method can be very useful for high resolution electrochemical imaging and kinetic experiments.[5] This same method can also be used to deliver species to a substrate surface and has been used for metal ion electrodeposition[35] and also to study the reactions of neutral species via facilitated ion transfer.[36]

1.2.3 The issue of substrate topography

In SECM, the probe needs to be positioned close to an interface with high precision and although this is achievable using piezoelectric positioners, it is often very difficult to determine the precise tip substrate separation. It is possible to use the amperometric response of the tip electrode when approaching to an inert surface but for many systems the addition of a redox mediator will affect the processes being

studied and hence is not a viable solution. This has led to the development of hybrid techniques in which various modes of operation attempt to solve this problem using unique positioning methods. These techniques will be discussed briefly in the following sections.

1.2.3.1 Scanning Electrochemical Microscopy – Atomic Force Microscopy (SECM-AFM)

One of the most well known hybrid techniques SECM – AFM combines both techniques by integrating a UME into an AFM tip. AFM acquires high resolution topographical images by monitoring interaction forces between the sharp tip and the surface attached to a force sensitive cantilever.[37] The merging of both techniques allows for the acquisition of topographically related, electrochemical activity at very high spatial resolution.[38] The most important component of this technique is the combined probe and significant progress has been undergone since the first reported instance, which consisted of the fabrication of a platinum wire into a force sensitive cantilever / electrochemical probe.[39] Batch fabrication methods are now available with different designs of probes being produced, either having ring electrodes embedded in a commercial AFM tip[40-41] or with the apex also acting as the working electrode.[42-44] Other methods of probe fabrication have also been reported, together with modelling of the tip response, but will not be discussed in this report.

Applications of SECM-AFM are wide due to the abundance of information that can be gained from this method. Typical test substrates have included patterned conducting-insulating samples and have been imaged in SECM feedback mode or SG-TC.[45] One field which made use of this method is materials science studying the

activity of electrode materials[44,46-47] and localised corrosion processes.[48-53] Membrane transport processes have also been investigated and are of great importance in separation methods, membrane supported reactions, gas permeation and in biological systems. Examples of systems studied include; fabricated polymer membranes, whereby the transport of redox mediator through each pore was investigated, correlating well with differences in pore diameter[54] and transport of glucose through a polycarbonate membrane, with the tip functionalised with an enzyme, glucose oxidase.[55] The enzyme converted glucose to hydrogen peroxide, which could be detected electrochemically and the local concentration of glucose corresponded with the predicted diffusion through each pore opening.[55] SECM-AFM has also been used for electrochemical patterning, giving the ability not only to generate smaller structures but also characterise them topographically.[56-57]

1.2.3.2 Scanning Electrochemical Microscopy – Scanning Tunnelling Microscopy (SECM-STM)

Electrochemical scanning tunnelling microscopy (EC-STM) allows for the investigation of electrochemical reactions at sub Å to the nm level.[58] The probe consists of a sharp STM tip coated with an insulating layer exposing only the end, reducing any unwanted electrochemical processes to the tunnelling current. EC-STM was subsequently combined with SECM using essentially the same setup. In this technique the tunnelling current was used for tip positioning and tracking topographical features. By implementing a consecutive lift mode, whereby the tip is retracted by a user defined distance, electrochemical measurements, common in SECM, were performed. Applications of this method include: corrosion studies in

stainless steel, where current spikes across the image were linked to pitting precursor sites,[59-60] electrochemical deposition of a palladium nanoparticle from the tip also studying its electrocatalytic activity,[61] the study of the electroactivity of a gold electrode modified with a self -assembled monolayer and mechanically scratched, observing an increased SECM feedback current at these specific sites[62] and also the integration of a pH electrode into the tip investigating the property dependence of electropolymerised polyaniline films.[63]

1.2.3.3 Dual mediator

Another approach for deconvoluting electrochemical activity and topography is to use two different mediators, one of which will be inactive to the surface chemistry being studied. By scanning over the substrate in a constant height mode, the inert mediator can allow for topographical information to be gained. A subsequent retrace at a potential at which the electrochemically active mediator to the system being studied, identifies a particular property connected to the activity of the sample. Some examples of this method have been seen in mapping the permeability of molecules in biological systems.[28-29]

1.2.3.4 Shear force SECM

This method achieves control of tip substrate separation by using a probe oscillated in the x-y plane, detecting the shear forces that occur when in close proximity to the surface of interest, that result in a damping of the oscillation amplitude.[64] This method for distance control was originally developed for near field

scanning optical microscopy (NSOM).[65] It was found that this effect had a significant distance dependence (particularly close to a surface) and was a convenient way of controlling the position of the UME for constant distance imaging. The damping in oscillation amplitude can be monitored in two ways: 1) by shining a laser on the very end of the electrode and detecting the signal using a photodiode[64,66] 2) by using a quartz crystal resonator attached to the probe and detecting the damping in vibration.[67-68]

Due to the mode of operation of this technique, the probes used need to be sub micron, needle like UMEs, in order to achieve a sufficient amplitude of oscillation and the topographical resolution is dependent on the tip diameter.[69] This places some limitations on the types of processes that can be studied. This setup can also be used with non pipet-based potentiometric probes[66], with applications in crystal dissolution studies[70], high resolution pH mapping[71] and also metal deposition.[72] The application of constant-distance shear-force SECM has allowed for the characterisation of single cells.[4] By mounting the setup onto an inverted microscope, the terminology Bio-SECM was introduced. An alternative imaging mode has also been developed and is termed 4D shear force constant distance SECM.[73] In this mode, the tip performs a series of approach curves at each point measuring the tip current at specific distance whilst approaching and also whilst retracting by a user defined amount. In this method diffusion profiles can be obtained and was demonstrated in generator-collector mode above a platinum band electrode.[73]

1.2.3.5 Alternating Current Scanning Electrochemical Microscopy (AC-SECM)

AC-SECM utilises an alternating potential (ca.10 mV) superimposed on a much larger tip bias that is generated from a function generator or internal oscillator of a lock-in amplifier (LIA). The modulated current signal is recorded, exhibiting a distance dependence between the tip and sample and hence can be used for positioning and for constant distance imaging.[74] This method does not require a redox mediator in solution, as it is the local impedance between tip and sample which is measured.[74] When a redox mediator is added, the Faradaic process can be used to determine the local electrochemical properties of the sample whilst the high frequency impedance signal is used for tip positioning and can be easily separated out. This method has been successfully used for a number of systems and an in depth review has recently been published.[74]

1.2.3.6 Tip position modulation (TPM) - SECM

TPM was an early advancement on the traditional feedback mode in SECM. In this configuration the amperometric tip is oscillated sinusoidally, perpendicular to the surface, with a very small amplitude.[75] The modulation in the tip position causes a modulation in the tip current at the same frequency, and through the use of lock-in techniques this signal is detected. The modulated signal further reduces any experimental complications which can arise due to potential drift and low signal to noise ratio when using much smaller UMEs. Both the amplitude and phase of the modulated current can be used to relate topographical features to electrochemical ones. When over an insulating substrate the modulated current is in phase with the oscillation of the tip but when over a conductive substrate the phase shifts by 180º.

The in-phase response over a conducting substrate can be easily modelled as a derivative of the steady-state behaviour but more complex models are required for the response over an insulating surface, as recently introduced by Edwards et al.[76] This method has shown to have improved sensitivity over tip-substrate separation, with minimal experimental modifications.[75]

1.2.3.7 Intermittent Contact SECM (IC-SECM)

Tip-substrate separation has commonly been controlled in AFM by oscillating the tip at its resonant frequency and then monitoring the damping in the oscillation amplitude resulting from surface contact.[77-78] This concept was recently applied to SECM but oscillating the tip at much lower frequencies (ca. 70 Hz).[79] In this mode, traditional SECM probes are utilised and, once the probe comes into contact with the substrate, a constant damping in the amplitude is maintained controlling the tip substrate separation. Once in contact, the topography, electrochemical response and also the modulated electrochemical response (resulting from the oscillating probe) are recorded. The technique utilises the fact that the tip and substrate will rarely be perfectly aligned and so only a small portion of the glass comes into contact. A lift mode was also introduced in which the tip is retracted on the reverse line and the current response measured whilst following the topography at a user-defined distance away. The method was proved on a gold band model substrate[79] and was also applied to a dental enamel system monitoring molecular transport through pores.[80] This demonstrated considerable enhancement in the spatial resolution and sensitivity compared to dc SECM.

1.2.4 Application of SECM in real world systems

1.2.4.1 Soft stylus probe

This type of probe was developed to facilitate imaging of very large samples compared to those usually studied in SECM and because of the nature of the probe tip crash is completely avoided.[81-82] The soft stylus probes consist of thin polymer films with a microchannel embedded inside, filled with a carbon ink. The carbon track is then laminated and the probe is cut and polished to produce a microelecrode.[82]

Under typical experimental conditions the probe is pressed against the sample so that the insulating part is always in contact and the thickness of the insulator defines the tip-sample separation. Due to the flexibility of these probes they can track topographical features without the need for complex electronic feedback circuits, maintaining a virtually constant tip-sample separation. Arrays of these probes have also been fabricated and used enabling the study of very large sample area in a much reduced experimental timescale.[81]

Another development of this system includes the insertion of a microfluidic channel, with an integrated reference / counter electrode. This acts as a fountain pen like probe delivering microliters of solution containing redox mediator acting as a two electrode microcell. This was developed to allow the characterisation of dry surfaces and also overcome problems of evaporation as encountered in conventional SECM.[83] The operation of the system acts like traditional feedback mode in SECM with an increased tip current over a conductor and decreased over an insulator.

A recent application of the method was for fingerprint analysis, whereby the fingerprints were developed using a silver stain[84] or metal deposition methods[85] and then imaged using the soft stylus technique. Tip currents were produced with the reaction of Iridium chloride ($IrCl_6^{3-/4-}$) mediator reacting with the silver producing high quality electrochemical images.[5] The advantage of this technique is that it usually takes 1 - 2 days to image such a large sample,[86] but using the microelectrode array this was performed in approximately 5 hours.[5]

1.2.4.2 SECM in Ionic Liquids

The migration to experimentation in ionic liquids expands the range of systems studied with applications such as batteries, fuel cells, etc.[87] Due to the high viscosity of these media, experimental challenges arise due to slow diffusion rates, experiencing reduced tip currents and increased time to reach steady-state currents.[5] Approach rates and scan speeds have to also be reduced in this media as it was found that hydrodynamic effects can have a serious influence on electrochemical measurements, making this system extremely difficult and unpractical to work with.[5,88] A few of these problems were overcome by migrating to nanometre-sized UMEs[31] but as the ionic liquid becomes more viscous, determined electron transfer kinetics decreased, as a result of slower mass transport, even with oxidised and reduced forms of the same electroactive species.[89]

1.3 Scanning ion conductance microscopy (SICM)

Originally developed by Hansma et al in 1989, SICM is a non-contact, scanned probe technique based on a nanopipet bathed in electrolytic solution.[90] The technique relies on an ion conductance current flowing between a quasi-reference-counter electrode (QRCE) inside a sharp pipet and another one in solution (Figures 1-13 to 1-15). The ion current measured is dependent on the probe to sample separation and provides a very good means of distance control. A number of advances in feedback mechanisms[91-95] have been made since the original system allowing for higher resolution and faster scan speeds showing the ability to study very delicate biological systems.

1.3.1 Probes

SICM nanopipets are prepared by a relatively simple process, which consists of the heating of a clamped capillary and a mechanical pull. The most common system is the use of a laser puller which can be programmed to yield the required diameter of the pipet, the length of the taper and also the cone angle. This ease of preparation and high success rate of probe manufacture make this technique particularly attractive.

1.3.2 Modes of operation

There are three main types of feedback mechanisms in SICM namely; non-modulated (dc), distance modulated (ac) and hopping modes. Each of these is discussed in the following sections.

1.3.2.1 Non-modulated (dc) mode

In the non-modulated mode, shown in Figure 1-13, a constant (dc) potential is applied between the electrode (QRCE) in the pipet and the electrode (QRCE) in solution. When far away from the surface a steady-state ion current is measured, but as the pipet approaches towards the surface, the ion current declines rapidly due to hindered ion migration (increased resistance). This property allows for constant distance imaging. The tip to sample separation is usually *ca*. an inner tip radius to avoid tip crash.[96] Applications of this method were to characterise cell membranes with very high resolution,[90,94,97] but when large topographical changes were encountered, relative to the tip diameter, the dc feedback was to slow. In addition, this method was susceptible to potential drift, pipet blockage and also changes in ionic strength.[96]

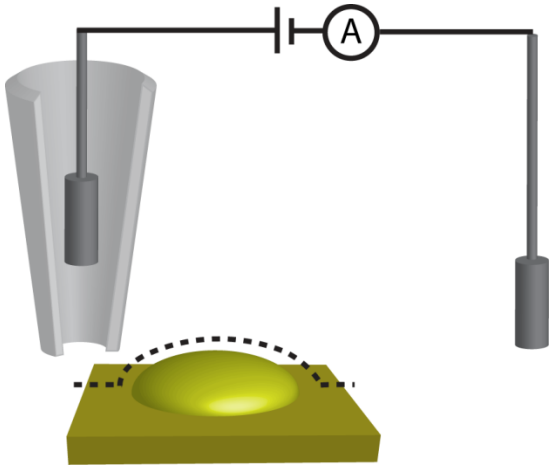

Figure 1-13: *A schematic showing dc mode SICM.*

1.3.2.2 Distance-modulated (ac) mode

Distance-modulated SICM, shown in Figure 1-14, operates similar to the dc mode, but with the probe oscillated in the vertical direction perpendicular to the surface. As the probe encounters the sample, the physical oscillation in the tip

position causes a modulation in the ion current, detected by a LIA. This is used as a feedback control signal. This feedback signal provides superior control over the probe position, compared to non-modulated SICM. The ac signal is relatively immune to potential drift or changes in ionic strength[95,98-99] and gives the ability to perform measurements on living cells on a much longer time scale.[98-99]

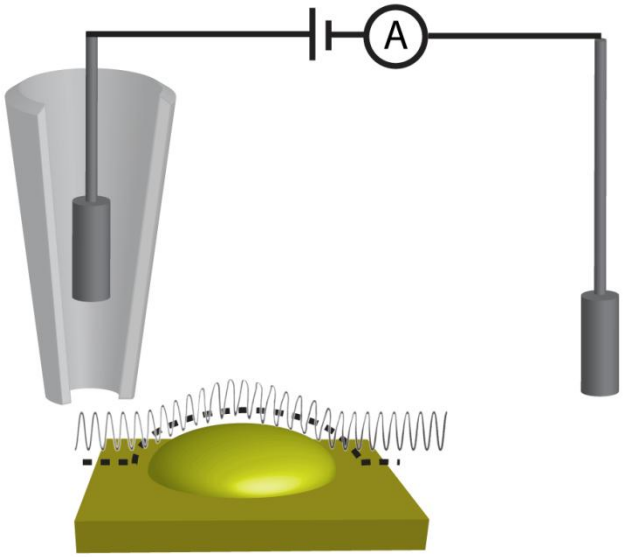

***Figure 1-14**: A schematic showing ac mode SICM.*

1.3.2.3 Hopping mode

Hopping mode SICM,[92] also known as backstep,[91,100] and standing approach mode,[93] shown in Figure 1-15, operate by performing a series of approach curves giving the ability to image topographically challenging samples, shown in Figure 1-10. In hopping mode, a prescan is performed in order to speed up the imaging. This consists of a low resolution image and if the topographical nature of a particular area exceeds a user defined threshold, then a high resolution scan is performed, otherwise the area is assumed to be featureless. This mode has been successfully used to image

complex 3D samples such as neurons at very high resolution identifying axons and dendrites, causing no damage to the live cell.[92]

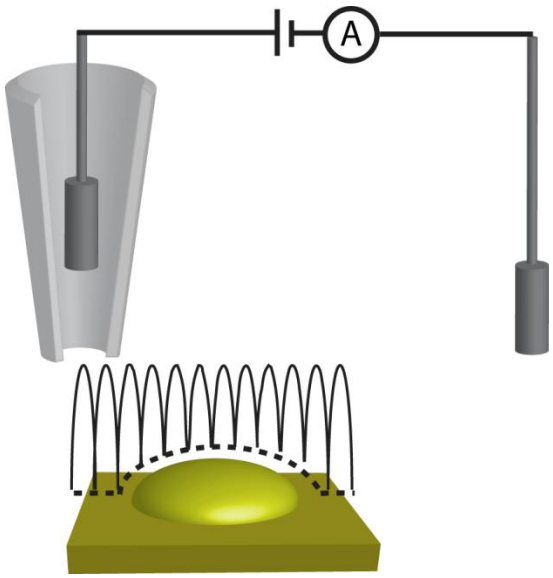

Figure 1-15: *A schematic showing hopping mode SICM.*

1.3.3 Applications of SICM

The major application for SICM has been the characterisation of live biological samples, with the ability to characterise the cell morphology, activity and also subcellular structures.[96]

The non-contact aspect of this technique allows for high resolution determination of cellular morphology, providing information on cell height, size and volume with very small error. The recent improvements in feedback methodology, namely hopping mode have allowed for single particle tracking within membranes[101] and very complex and delicate structures.[92-93] Differentiation in cell types is also

possible with SICM as demonstrated on cancer cells having three different variants, with different morphological attributes.[102]

The temporal stability of SICM has enabled the study of changes in cell morphology, due to migration.[95] Performing consecutive scans over the same area showed the direction of cell movement and also changes in volume.[100] The ability to monitor real time cellular activity has enabled the study of mobility and morphology of cells at different stages in the life cycle and also the effect of physiological processes.[96]

Morphological changes in cellular structure are usually accompanied by rearrangements in subcellular structure.[96] Studies with SICM have proved that subcellular dynamic studies are also possible, as demonstrated by examining small protrusions in cell membranes.[103]

SICM has also been used for physiological studies, correlating effects of surface morphology and also for identifying and studying the response of ion channels via scanning patch clamp techniques. A review has recently been published and detailed information can be found there.[96]

1.4 Chemical deposition using double barrel nanopipets

This method is a variant of distance modulated SICM, with the exception that the nanopipet consists of two separate channels, within the same capillary and is operated in air[104] or under organic solution.[105] A bias is applied between two QRCEs in each channel of the pipet, filled with electrolyte solution and the tip modulated perpendicularly to the surface. An ion current flows through a liquid meniscus at the end of the pipet and once surface contact is made a modulation in the ion current

arises, due a modulation in resistance.[104-105] Figure 1-16 a) shows a schematic of the described system

The modulation in the ion current is detected using an LIA and this parameter used as setpoint for constant distance feedback imaging. The system was first proved on a PDMS stamp showing the probe accurately tracking the surface features and was then used to deposit fluorescent biomolecules on a functionalised surface.[104] The advantage of this method is that the amount of material deposited can be controlled via the applied voltage between the two channels. With different voltage pulses and durations, a linear dependence on spot diameters was observed.[104] The method was then used for more complex patterns (shown in Figure1-16 b) and c)) and a two component graded deposition was used. This was achieved by using differently charged species and by changing the polarity of the bias between the two electrodes in the pipet, selective deposition was achieved on a functionalised surface.[104-105] The advantage of this method, compared to other patterning techniques, is that the pipet holds a large reservoir of chemical species and eliminates the need for tip conditioning before deposition.

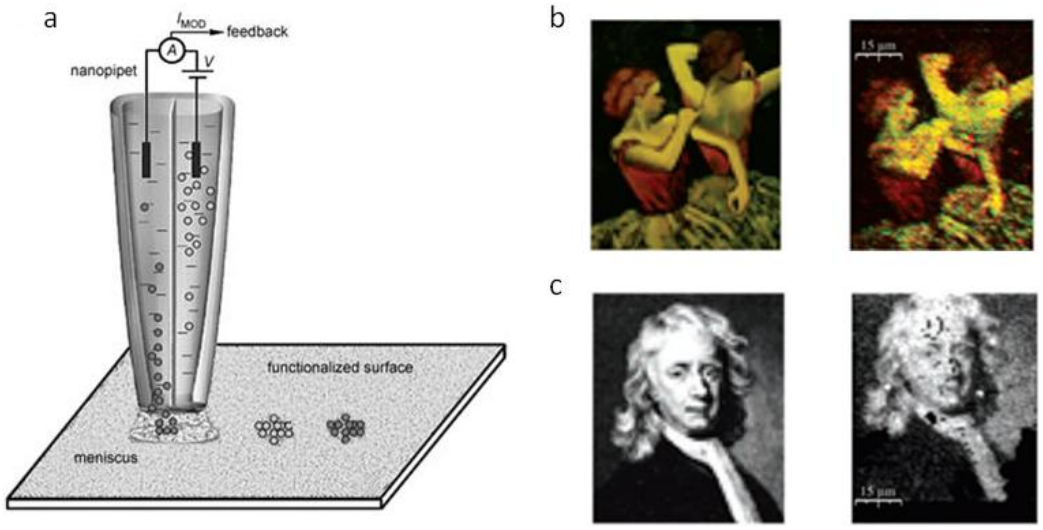

Figure 1-16: *A schematic of the double barrel nanopipet system a), b) and c) are the original images (right) together with their patterned counterparts (left) using a two component graded deposition.*[104]

1.5 Scanning Electrochemical Microscopy – Scanning Ion Conductance Microscopy (SECM – SICM)

SECM-SICM combines the features of both techniques to gain high resolution topographical imaging coupled with corresponding electrochemical data. A key feature is that tip positioning is achieved in a non contact mode and hence the probe cannot damage the system being studied. As with all scanned probe techniques, the tip is the most important aspect of the system and different fabrication methods have been explored. The first reports of tips utilised a pulled capillary of about 100 nm diameter coated with gold on one side and then insulated using an aluminium oxide. The end of the probe was then exposed using focussed ion beam (FIB).[106] Another approach was to form a gold ring electrode around the pulled pipet, which was then insulated with electrophoretic paint, again using FIB to expose the end.[107] This method has been shown on gold bands on glass as reported

by Comstock et al, using the SICM feedback in ac mode.[106] Takahashi et al proved their ring electrode system on an interdigitated platinum array electrode and then applied the same system to study enzyme activity of both glucose oxidase and horseradish peroxidise and also permeation of a cardiac myocyte cell membrane. The experiment was performed in a hopping mode feedback type, relating high resolution topography to the electrochemical response.[107]

1.6 Pipet Based Electrochemical techniques

1.6.1 Techniques developed for localised corrosion studies

Pipet based electrochemical techniques were initially developed for high resolution corrosion studies with probe dimensions between 1 and 1000 μm, but typically on the range of 100s of microns, in diameter with the end of the pipet coated in a thick layer of silicone rubber.[108-109] The pipets were approached towards a surface of interest and the silicon gasket at the end formed a seal with the substrate. A schematic of the setup is shown in Figure 1-17. Electrochemical measurements could then be performed with a resolution defined by the tip diameter. Studies were conducted on stainless steel samples to identifying corrosion mechanisms and pitting sites.[108-109]

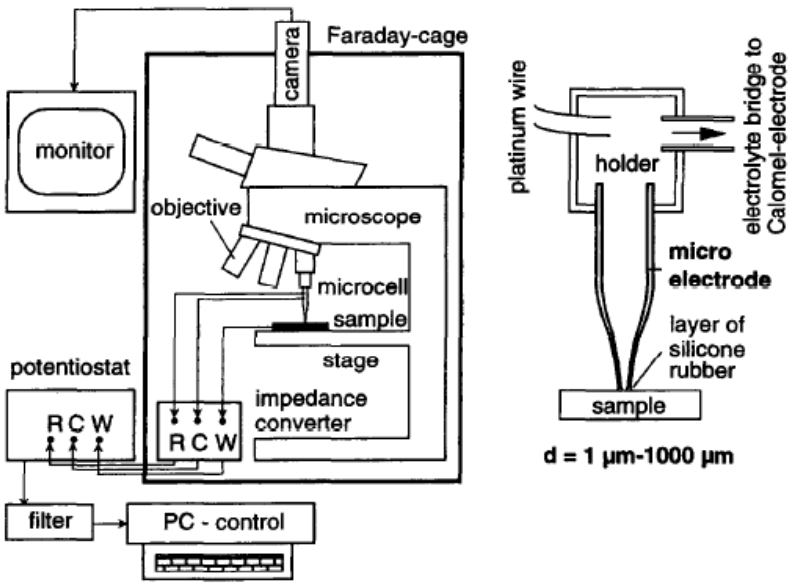

Figure 1-17*: A schematic of the experimental setup for the microcell reactor using a microscope for visualisation of the probe position. The expanded image to the right, shows the capillary connected up in a 3-electrode system.*[108-109]

The technique was further developed to include a feedback mechanism, to determine the tip substrate separation.[110] In this case the substrate was oscillated at the resonant frequency of the piezoelectric actuators and surface contact was detected due to a damping in the oscillation amplitude or a shift in the resonant frequency. This method was never progressed and no imaging applications were ever presented, most probably due to the complexity of the system.

Based on a similar setup, the scanning droplet cell was developed, shown in Figure 1-18. In this method small electrolyte droplets are positioned on the surface, formed by surface tension allowing for spatially resolved surface modification and analysis. In cases where the surface is extremely hydrophilic a silicon gasket at the end of the probe is pressed against the surface to control the area of investigation. The part of the substrate in contact with the droplet acts as the working electrode and the pipet contains the counter and reference electrodes. Techniques common in

electrochemical analysis can be performed, allowing for high resolution measurements to be made. The main applications of this method have been for corrosion studies, improving the resolution over all previously developed methods also eliminating any passivation which can occur due to the whole sample being immersed in solution.[111-113]

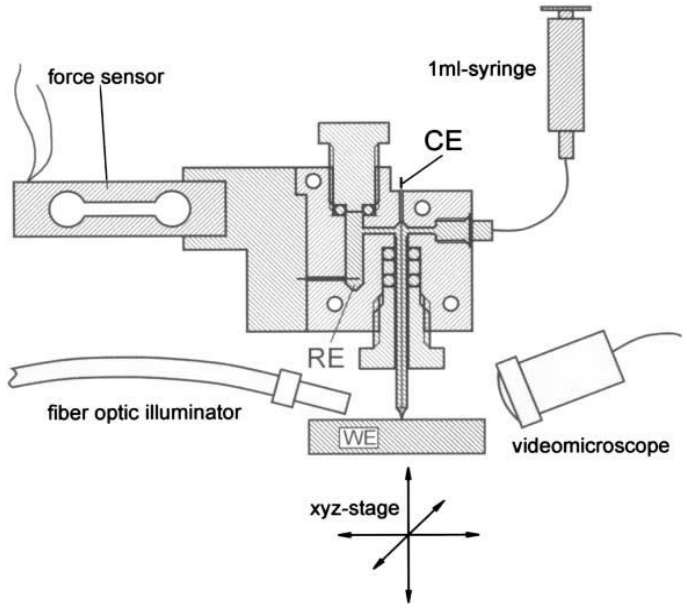

Figure 1-18: *A schematic of the scanning droplet cell.*[112]

A flow through microcell reactor was subsequently developed with the idea of removing any products of the reaction occurring, especially when large current densities were involved and also to produce a method to analyse these products. This concept is based on a theta, dual channel capillary, with the septum etched to allow electrolyte to flow through as shown in Figure 1-19 and was usually on the range of a few hundred microns in diameter. The end is coated with a silicone gasket, preventing any electrolyte leakage, also defining the working electrode area.[114] The sample is fitted to a xyz positioner and a video microscope is used to position the pipet on the surface. Electrolyte flow is controlled via an external pump, which then

goes to a flow through cuvette and can be analysed using a UV-Vis spectrometer as shown in Figure 1-19. The system was first proved on pure iron rods, by first monitoring the effect of flow rate on the current density, which was also simulated, and then separation of the iron (ii) and iron (iii) was achieved by adding a bidentate ligand as a chelating agent which prevented further oxidation of iron (ii). This allowed for both complexes to be detected simultaneously, by looking at different absorption wavelengths corresponding to the complexes.[114] The system has been used mostly for metallic dissolution studies with the ability to characterise the solute.[115-117]

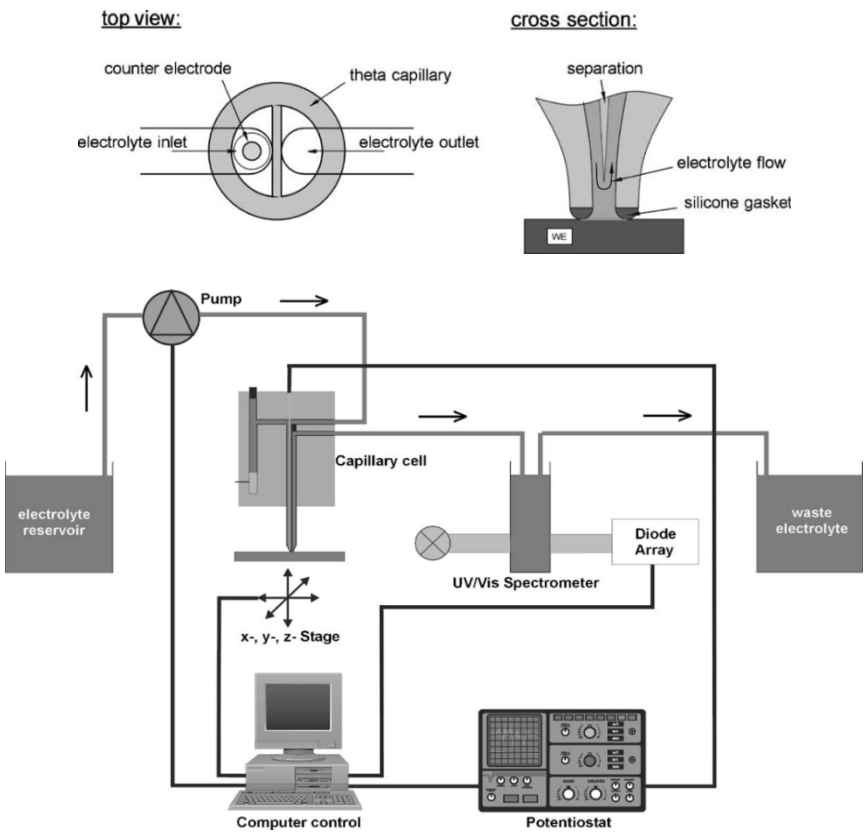

***Figure 1-19**: A schematic of the capillary flow cell system.*[114]

1.6.2 Scanning Micropipet Contact Method (SMCM)

In SMCM a mobile micropipette, of diameters between 300 nm – 1 μm, is used to conduct high resolution electrochemical measurements, shown in Figure 1-20. The technique operates in air and the pipet is filled with an electroactive species in electrolyte solution, with a reference electrode inserted inside the channel. The probe is translated carefully toward the surface with a bias applied between the reference electrode and the working electrode (conducting / semiconducting substrate), at a potential corresponding to the oxidation or reduction of the electroactive species inside the pipet. Once the liquid meniscus at the end of the probe makes contact with the surface, an electrochemical current is detected and the motion of the probe is halted, allowing for subsequent electrochemical measurements to be made. The technique operates in a hopping mode regime, but in this case simultaneous topography was not extracted as the signal is dependent on the electrochemical activity of the substrate. Measurements are typically carried out in a humid environment to reduce evaporation at the pipet meniscus. The technique was applied to determine the electrochemical activity of basal plane highly oriented pyrolytic graphite (HOPG) showing that it was not as inactive as previously thought and also to study the corrosion activity of an aluminium alloy.[118]

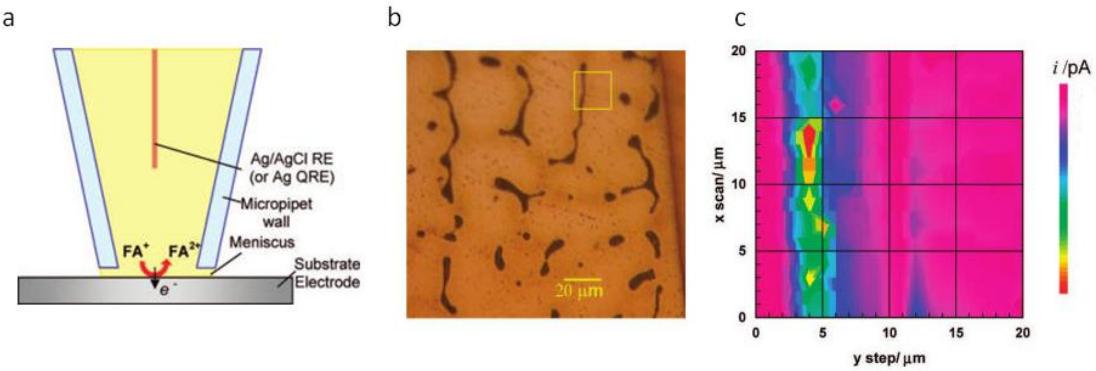

Figure 1-20: *A schematic of the SMCM setup a) and optical image of the aluminium alloy b) and the corresponding electrochemical image c).*[118]

1.6.3 Scanning Electrochemical Cell Microscopy (SECCM)

SECCM is an extension of SMCM, utilising the double barrel pipet system described in Section 1.4 but modified to make high resolution electrochemical measurements. In this case the double barrel pipet is filled with electrolyte and redox mediator of choice with a reference electrode inserted into each channel and a bias applied between them. The substrate is connected up as a working electrode (measured with respect to ground) and its potential is controlled by floating the reference electrode potentials with respect to ground. The incorporation of a positional feedback allowed for the investigation of hereterogeneous electrode materials maintaining a constant tip-sample separation. This also eliminated the need for the substrate to be entirely semi/conducting, as with SMCM. Being a pipet based electrochemical imaging technique the migration to small / nano electrodes proved to be rather simple when compared to other techniques, such as SECM, and this thesis describes the development and application of such a system. Chapter 2 describes the setup of the instrumentation whilst Chapters 3- 5 describe the applications of

SECCM starting from a model test substrate, as a proof of concept, moving onto more complex systems.

1.7 Research Aims

This introduction has highlighted the considerable possibilities that are opened up with various high resolution electrochemical techniques. Some of the pipet based methods, in particular, involve probes which are easy to fabricate with very high spatial resolution. Herein the developments and applications of SECCM and SECM-SICM are described with emphasis on carbon electrode materials and the rationale for studying these are outlined in each chapter.

Chapter 2 describes the building of the new instrument starting from combining all the necessary hardware components, together with writing the control software required to operate the technique. It also describes some of the complimentary analytical techniques used and some sample synthesis methods.

Chapter 3 is the original experimental work performed on the operation of the new electrochemical scanned probe technique together with a very brief insight to a theoretical model which has been developed within our group.

Chapter 4 describes the application of the technique to a complex and heterogeneous electrode material, CVD graphene. Due to the electrochemical confinement provided by such a novel scanned probe technique electrochemical activity is correlated to surface structure.

Chapter 5 concerns the fundamental electrochemical behaviour of single walled carbon nanotubes. There have been many hypotheses over the years to where the

nature of electron transfer occurs and with our method a clear picture is provided. Point electrochemical measurements are performed on a 3 dimensional carbon nanotube structure (forest), comparing the response at closed ends and sidewalls, and second, nanoscale electrochemical imaging is performed on a 2 dimensional network of carbon nanotubes identifying the behaviour of a sidewall rich sample. Finite element modelling is also used to try and quantify the observations providing a rationalisation for the proposed hypothesis.

Chapter 6 is a short chapter on the fabrication and characterisation of dual barrel SECM – SICM electrodes and is only a small part of a much larger piece of work described elsewhere.[119]

Chapter 7 provides a brief conclusion of the work.

1.8 References:

(1) Fisher, A. C. *Oxford University Press* **1996**

(2) Bard, A. J.; Faulkner, L. R. *Electrochemical methods fundamentals and applications*; Wiley: Weinheim, 2001.

(3) Mirkin, M. V.; Horrocks, B. R. *Anal. Chim. Acta* **2000**, *406*, 119.

(4) Amemiya, S.; Bard, A. J.; Fan, F. R. F.; Mirkin, M. V.; Unwin, P. R. In *Annual Review of Analytical Chemistry*; Annual Reviews: Palo Alto, 2008; Vol. 1, p 95.

(5) Mirkin, M. V.; Nogala, W.; Velmurugan, J.; Wang, Y. *Physical Chemistry Chemical Physics* **2011**, *13*, 21196.

(6) Barker, A. L.; Gonsalves, M.; Macpherson, J. V.; Slevin, C. J.; Unwin, P. R. *Anal. Chim. Acta* **1999**, *385*, 223.

(7) Bard, A. J.; Fan, F. R. F.; Pierce, D. T.; Unwin, P. R.; Wipf, D. O.; Zhou, F. M. *Science* **1991**, *254*, 68.

(8) Wittstock, G.; Burchardt, M.; Pust, S. E.; Shen, Y.; Zhao, C. *Angew. Chem.-Int. Edit.* **2007**, *46*, 1584.

(9) Edwards, M. A.; Martin, S.; Whitworth, A. L.; Macpherson, J. V.; Unwin, P. R. *Physiol. Meas.* **2006**, *27*, R63.

(10) Hsu, C.-Y.; Vasantha, V. S.; Ho, K.-C. *Electrochimica Acta* **2008**, *53*, 6244.

(11) Arca, M.; Mirkin, M. V.; Bard, A. J. *J. Phys. Chem.* **1995**, *99*, 5040.

(12) Zhao, C.; Wittstock, G. *Angew. Chem.-Int. Edit.* **2004**, *43*, 4170.

(13) Pierce, D. T.; Bard, A. J. *Anal. Chem.* **1993**, *65*, 3598.

(14) Kranz, C.; Wittstock, G.; Wohlschlager, H.; Schuhmann, W. *Electrochimica Acta* **1997**, *42*, 3105.

(15) Turyan, I.; Matsue, T.; Mandler, D. *Anal. Chem.* **2000**, *72*, 3431.

(16) Zoski, C. G. *Electroanalysis* **2002**, *14*, 1041.

(17) Forster, R. J. *Encyclopedia of electrochemistry volume 3: Instrumentation and electroanalytical chemistry*; Wiley, 2003; Vol. 3.

(18) Liu, H. Y.; Fan, F. R. F.; Lin, C. W.; Bard, A. J. *J. Am. Chem. Soc.* **1986**, *108*, 3838.

(19) Slevin, C. J.; Umbers, J. A.; Atherton, J. H.; Unwin, P. R. *Journal of the Chemical Society, Faraday Transactions* **1996**, *92*, 5177.

(20) Barker, A. L.; Macpherson, J. V.; Slevin, C. J.; Unwin, P. R. *The Journal of Physical Chemistry B* **1998**, *102*, 1586.

(21) Kwak, J.; Bard, A. J. *Anal. Chem.* **1989**, *61*, 1221.

(22) Unwin, P. R.; Bard, A. J. *The Journal of Physical Chemistry* **1991**, *95*, 7814.

(23) Horrocks, B. R.; Mirkin, M. V.; Bard, A. J. *J. Phys. Chem.* **1994**, *98*, 9106.

(24) Macpherson, J. V.; Unwin, P. R. *J. Phys. Chem.* **1994**, *98*, 1704.

(25) Martin, R. D.; Unwin, P. R. *Anal. Chem.* **1998**, *70*, 276.

(26) Zhou, F. M.; Unwin, P. R.; Bard, A. J. *J. Phys. Chem.* **1992**, *96*, 4917.

(27) Evans, N. J.; Gonsalves, M.; Gray, N. J.; Barker, A. L.; Macpherson, J. V.; Unwin, P. R. *Electrochem. Commun.* **2000**, *2*, 201.

(28) Gonsalves, M.; Macpherson, J. V.; O'Hare, D.; Winlove, C. P.; Unwin, P. R. *Biochim. Biophys. Acta-Gen. Subj.* **2000**, *1524*, 66.

(29) Macpherson, J. V.; Ohare, D.; Unwin, P. R.; Winlove, C. P. *Biophys. J.* **1997**, *73*, 2771.

(30) Zhan, D. P.; Li, X.; Zhan, W.; Fan, F. R. F.; Bard, A. J. *Anal. Chem.* **2007**, *79*, 5225.

(31) Laforge, F. O.; Velmurugan, J.; Wang, Y. X.; Mirkin, M. V. *Anal. Chem.* **2009**, *81*, 3143.

(32) Elsamadisi, P.; Wang, Y.; Velmurugan, J.; Mirkin, M. V. *Anal. Chem.* **2011**, *83*, 671.

(33) Elsamadisi, P.; Wang, Y. X.; Velmurugan, J.; Mirkin, M. V. *Anal. Chem.* **2011**, *83*, 671.

(34) Ishimatsu, R.; Kim, J.; Jing, P.; Striemer, C. C.; Fang, D. Z.; Fauchet, P. M.; McGrath, J. L.; Amemiya, S. *Anal. Chem.* **2010**, *82*, 7127.

(35) Yatziv, Y.; Turyan, I.; Mandler, D. *J. Am. Chem. Soc.* **2002**, *124*, 5618.

(36) Lin, C.-L.; Rodriguez-Lopez, J.; Bard, A. J. *Anal. Chem.* **2009**, *81*, 8868.

(37) Binnig, G.; Quate, C. F.; Gerber, C. *Phys. Rev. Lett.* **1986**, *56*, 930.

(38) Gardner, C. E.; Macpherson, J. V. *Anal. Chem.* **2002**, *74*, 576A.

(39) Macpherson, J. V.; Unwin, P. R. *Anal. Chem.* **1999**, *72*, 276.

(40) Shin, H.; Hesketh, P. J.; Mizaikoff, B.; Kranz, C. *Anal. Chem.* **2007**, *79*, 4769.

(41) Shin, H.; Hesketh, P. J.; Mizaikofff, B.; Kranz, C. *Sens. Actuator B-Chem.* **2008**, *134*, 488.

(42) Akiyama, T.; Gullo, M. R.; de Rooij, N. F.; Tonin, A.; Hidber, H. R.; Frederix, P.; Engel, A.; Staufer, U. *Japanese Journal of Applied Physics Part 1-Regular Papers Short Notes & Review Papers* **2004**, *43*, 3865.

(43) Gullo, M. R.; Frederix, P. L. T. M.; Akiyama, T.; Engel, A.; deRooij, N. F.; Staufer, U. *Anal. Chem.* **2006**, *78*, 5436.

(44) Frederix, P. L. T. M.; Bosshart, P. D.; Akiyama, T.; Chami, M.; Gullo, M. R.; Blackstock, J. J.; Dooleweerdt, K.; de Rooij, N. F.; Staufer, U.; Engel, A. *Nanotechnology* **2008**, *19*.

(45) Burt, D. P.; Wilson, N. R.; Weaver, J. M. R.; Dobson, P. S.; Macpherson, J. V. *Nano Lett.* **2005**, *5*, 639.

(46) Macpherson, J. V.; de Mussy, J. P. G.; Delplancke, J. L. *Journal of the Electrochemical Society* **2002**, *149*, B306.

(47) Pust, S. E.; Salomo, M.; Oesterschulze, E.; Wittstock, G. *Nanotechnology* **2010**, *21*.

(48) Davoodi, A.; Pan, J.; Leygraf, C.; Norgren, S. *Electrochem. Solid State Lett.* **2005**, *8*, B21.

(49) Davoodi, A.; Farzadi, A.; Pan, J.; Leygraf, C.; Zhu, Y. *Journal of the Electrochemical Society* **2008**, *155*, C474.

(50) Davoodi, A.; Pan, J.; Leygraf, C.; Norgren, S. *Journal of the Electrochemical Society* **2008**, *155*, C211.

(51) Davoodi, A.; Pan, J.; Leygraf, C.; Norgren, S. *Journal of the Electrochemical Society* **2008**, *155*, C138.

(52) Davoodi, A.; Pan, J.; Leygraf, C.; Norgren, S. *Electrochimica Acta* **2007**, *52*, 7697.

(53) Davoodi, A.; Pan, J.; Leygraf, C.; Norgren, S. *Applied Surface Science* **2006**, *252*, 5499.

(54) Gardner, C. E.; Unwin, P. R.; Macpherson, J. V. *Electrochem. Commun.* **2005**, *7*, 612.

(55) Kueng, A.; Kranz, C.; Lugstein, A.; Bertagnolli, E.; Mizaikoff, B. *Angew. Chem.-Int. Edit.* **2005**, *44*, 3419.

(56) Ghorbal, A.; Grisotto, F.; Charlier, J.; Palacin, S.; Goyer, C.; Demaille, C. *Chemphyschem* **2009**, *10*, 1053.

(57) Sekine, S.; Kaji, H.; Nishizawa, M. *Anal. Bioanal. Chem.* **2008**, *391*, 2711.

(58) Nagahara, L. A.; Thundat, T.; Lindsay, S. M. *Rev. Sci. Instrum.* **1989**, *60*, 3128.

(59) Zhu, Y.; Williams, D. E. *Journal of the Electrochemical Society* **1997**, *144*, L43.

(60) Williams, D. E.; Mohiuddin, T. F.; Zhu, Y. Y. *Journal of the Electrochemical Society* **1998**, *145*, 2664.
(61) Meier, J.; Friedrich, K. A.; Stimming, U. *Faraday Discussions* **2002**, *121*, 365.
(62) Treutler, T. H.; Wittstock, G. *Electrochimica Acta* **2003**, *48*, 2923.
(63) Ammann, E.; Beuret, C.; Indermuhle, P. F.; Kotz, R.; de Rooij, N. F.; Siegenthaler, H. *Electrochimica Acta* **2001**, *47*, 327.
(64) Ludwig, M.; Kranz, C.; Schuhmann, W.; Gaub, H. E. *Rev. Sci. Instrum.* **1995**, *66*, 2857.
(65) Betzig, E.; Finn, P. L.; Weiner, J. S. *Appl. Phys. Lett.* **1992**, *60*, 2484.
(66) Hengstenberg, A.; Kranz, C.; Schuhmann, W. *Chem.-Eur. J.* **2000**, *6*, 1547.
(67) Buchler, M.; Kelley, S. C.; Smyrl, W. H. *Electrochem. Solid State Lett.* **2000**, *3*, 35.
(68) James, P.; Casillas, N.; Smyrl, W. H. *Journal of the Electrochemical Society* **1996**, *143*, 3853.
(69) Katemann, B. B.; Schuhmann, W. *Electroanalysis* **2002**, *14*, 22.
(70) Etienne, M.; Schulte, A.; Mann, S.; Jordan, G.; Dietzel, I. D.; Schuhmann, W. *Anal. Chem.* **2004**, *76*, 3682.
(71) Etienne, M.; Dierkes, P.; Erichsen, T.; Schuhmann, W.; Fritsch, I. *Electroanalysis* **2007**, *19*, 318.
(72) Turyan, I.; Etienne, M.; Mandler, D.; Schuhmann, W. *Electroanalysis* **2005**, *17*, 538.
(73) Nebel, M.; Eckhard, K.; Erichsen, T.; Schulte, A.; Schuhmann, W. *Anal. Chem.* **2010**, *82*, 7842.
(74) Eckhard, K.; Schuhmann, W. *Analyst* **2008**, *133*, 1486.
(75) Wipf, D. O.; Bard, A. J. *Anal. Chem.* **1992**, *64*, 1362.
(76) Edwards, M. A.; Whitworth, A. L.; Unwin, P. R. *Anal. Chem.* **2011**, *83*, 1977.
(77) Hansma, P. K.; Cleveland, J. P.; Radmacher, M.; Walters, D. A.; Hillner, P. E.; Bezanilla, M.; Fritz, M.; Vie, D.; Hansma, H. G.; Prater, C. B.; Massie, J.; Fukunaga, L.; Gurley, J.; Elings, V. *Appl. Phys. Lett.* **1994**, *64*, 1738.
(78) Moller, C.; Allen, M.; Elings, V.; Engel, A.; Muller, D. J. *Biophys. J.* **1999**, *77*, 1150.
(79) McKelvey, K.; Edwards, M. A.; Unwin, P. R. *Anal. Chem.* **2010**, *82*, 6334.
(80) McKelvey, K.; Snowden, M. E.; Peruffo, M.; Unwin, P. R. *Anal. Chem.* **2011**, *83*, 6447.
(81) Cortes-Salazar, F.; Momotenko, D.; Lesch, A.; Wittstock, G.; Girault, H. H. *Anal. Chem.* **2010**, *82*, 10037.
(82) Cortes-Salazar, F.; Traeuble, M.; Li, F.; Busnel, J.-M.; Gassner, A.-L.; Hojeij, M.; Wittstock, G.; Girault, H. H. *Anal. Chem.* **2009**, *81*, 6889.
(83) Cortes-Salazar, F.; Lesch, A.; Momotenko, D.; Busnel, J.-M.; Wittstock, G.; Girault, H. H. *Analytical Methods* **2010**, *2*, 817.
(84) Zhang, M.; Girault, H. H. *Electrochem. Commun.* **2007**, *9*, 1778.
(85) Zhang, M.; Becue, A.; Prudent, M.; Champod, C.; Girault, H. H. *Chem. Commun.* **2007**, 3948.
(86) Cortes-Salazar, F.; Momotenko, D.; Girault, H. H.; Lesch, A.; Wittstock, G. *Anal. Chem.* **2011**, *83*, 1493.
(87) Hapiot, P.; Lagrost, C. *Chemical Reviews* **2008**, *108*, 2238.
(88) Fontaine, O.; Lagrost, C.; Ghilane, J.; Martin, P.; Trippe, G.; Fave, C.; Lacroix, J. C.; Hapiot, P.; Randriamahazaka, H. N. *J. Electroanal. Chem.* **2009**, *632*, 88.
(89) Ghilane, J.; Lagrost, C.; Hapiot, P. *Anal. Chem.* **2007**, *79*, 7383.
(90) Hansma, P.; Drake, B.; Marti, O.; Gould, S.; Prater, C. *Science* **1989**, *243*, 641.

(91) Mann, S. A.; Hoffmann, G.; Hengstenberg, A.; Schuhmann, W.; Dietzel, I. D. *J. Neurosci. Methods* **2002**, *116*, 113.

(92) Novak, P.; Li, C.; Shevchuk, A. I.; Stepanyan, R.; Caldwell, M.; Hughes, S.; Smart, T. G.; Gorelik, J.; Ostanin, V. P.; Lab, M. J.; Moss, G. W. J.; Frolenkov, G. I.; Klenerman, D.; Korchev, Y. E. *Nature Methods* **2009**, *6*, 935.

(93) Takahashi, Y.; Murakami, Y.; Nagamine, K.; Shiku, H.; Aoyagi, S.; Yasukawa, T.; Kanzaki, M.; Matsue, T. *Physical Chemistry Chemical Physics* **2010**, *12*, 10012.

(94) Korchev, Y. E.; Bashford, C. L.; Milovanovic, M.; Vodyanoy, I.; Lab, M. J. *Biophys. J.* **1997**, *73*, 653.

(95) Shevchuk, A. I.; Gorelik, J.; Harding, S. E.; Lab, M. J.; Klenerman, D.; Korchev, Y. E. *Biophys. J.* **2001**, *81*, 1759.

(96) Chen, C.-C.; Zhou, Y.; Baker, L. A. *Annual Review of Analytical Chemistry* **2012**, *5*, null.

(97) Korchev, Y. E.; Milovanovic, M.; Bashford, C. L.; Bennett, D. C.; Sviderskaya, E. V.; Vodyanoy, I.; Lab, M. J. *Journal of Microscopy-Oxford* **1997**, *188*, 17.

(98) Gorelik, J.; Zhang, Y. J.; Shevchuk, A. I.; Frolenkov, G. I.; Sanchez, D.; Lab, M. J.; Vodyanoy, I.; Edwards, C. R. W.; Klenerman, D.; Korchev, Y. E. *Molecular and Cellular Endocrinology* **2004**, *217*, 101.

(99) Zhang, Y. J.; Gorelik, J.; Sanchez, D.; Shevchuk, A.; Lab, M.; Vodyanoy, I.; Klenerman, D.; Edwards, C.; Korchev, Y. *Kidney International* **2005**, *68*, 1071.

(100) Happel, P.; Hoffmann, G.; Mann, S. A.; Dietzel, I. D. *Journal of Microscopy-Oxford* **2003**, *212*, 144.

(101) Adler, J.; Shevchuk, A. I.; Novak, P.; Korchev, Y. E.; Parmryd, I. *Nature Methods* **2010**, *7*, 170.

(102) Liu, X.; Yang, X.; Zhang, B.; Zhang, X.; Lu, H.; Zhang, J.; Zhang, Y. *Brain Research* **2011**, *1386*, 35.

(103) Gorelik, J.; Shevchuk, A. I.; Frolenkov, G. I.; Diakonov, I. A.; Lab, M. J.; Kros, C. J.; Richardson, G. P.; Vodyanoy, I.; Edwards, C. R. W.; Klenerman, D.; Korchev, Y. E. *Proceedings of the National Academy of Sciences of the United States of America* **2003**, *100*, 5819.

(104) Rodolfa, K. T.; Bruckbauer, A.; Zhou, D. J.; Korchev, Y. E.; Klenerman, D. *Angew. Chem.-Int. Edit.* **2005**, *44*, 6854.

(105) Rodolfa, K. T.; Bruckbauer, A.; Zhou, D. J.; Schevchuk, A. I.; Korchev, Y. E.; Klenerman, D. *Nano Lett.* **2006**, *6*, 252.

(106) Comstock, D. J.; Elam, J. W.; Pellin, M. J.; Hersam, M. C. *Anal. Chem.* **2010**, *82*, 1270.

(107) Takahashi, Y.; Shevchuk, A. I.; Novak, P.; Murakami, Y.; Shiku, H.; Korchev, Y. E.; Matsue, T. *J. Am. Chem. Soc.* **2010**, *132*, 10118.

(108) Bohni, H.; Suter, T.; Schreyer, A. *Electrochimica Acta* **1995**, *40*, 1361.

(109) Suter, T.; Bohni, H. *Electrochimica Acta* **1997**, *42*, 3275.

(110) Eng, L.; Wirth, E.; Suter, T.; Bohni, H. *Electrochimica Acta* **1998**, *43*, 3029.

(111) Hassel, A. W.; Lohrengel, M. M. *Electrochimica Acta* **1997**, *42*, 3327.

(112) Lohrengel, M. M.; Moehring, A.; Pilaski, M. *Electrochimica Acta* **2001**, *47*, 137.

(113) Lohrengel, M. M.; Moehring, A.; Pilaski, M. *Fresenius Journal of Analytical Chemistry* **2000**, *367*, 334.

(114) Lohrengel, M. M.; Rosenkranz, C.; Klüppel, I.; Moehring, A.; Bettermann, H.; Bossche, B. V. d.; Deconinck, J. *Electrochimica Acta* **2004**, *49*, 2863.

(115) Klemm, S. O.; Pust, S. E.; Hassel, A. W.; Huepkes, J.; Mayrhofer, K. J. J. *Journal of Solid State Electrochemistry* **2012**, *16*, 283.

(116) Klemm, S. O.; Schauer, J.-C.; Schuhmacher, B.; Hassel, A. W. *Electrochimica Acta* **2011**, *56*, 9627.

(117) Klemm, S. O.; Schauer, J.-C.; Schuhmacher, B.; Hassel, A. W. *Electrochimica Acta* **2011**, *56*, 4315.

(118) Williams, C. G.; Edwards, M. A.; Colley, A. L.; Macpherson, J. V.; Unwin, P. R. *Anal. Chem.* **2009**, *81*, 2486.

(119) Takahashi, Y.; Shevchuk, A. I.; Novak, P.; Zhang, Y.; Ebejer, N.; Macpherson, J. V.; Unwin, P. R.; Pollard, A. J.; Roy, D.; Clifford, C. A.; Shiku, H.; Matsue, T.; Klenerman, D.; Korchev, Y. E. *Angewandte Chemie International Edition* **2011**, *50*, 9638.

CHAPTER 2
Instrument Design, Construction and Experimental techniques

This chapter deals with the setting up of a new electrochemical scanned probe technique, SECCM, from the hardware to the writing of control software. Materials synthesis and preparation are also described together with various analytical techniques which were used as complementary tools to accurately characterise the samples being investigated.

2.1 SECCM

SECCM utilizes a double barrel (theta) pipet, filled with electrolyte solution and two quasi-reference counter electrodes (QRCEs), inserted into each channel as a probe. A thin meniscus droplet at the end of the pipet constitutes a mobile, nanoscopic electrochemical cell. By modulating the probe in the z direction, it can be brought into contact with a surface, maintaining a constant tip to sample separation, for high resolution electrochemical (ion transfer and electron transfer) imaging. Figure 2-1 shows the majority of the components used in SECCM, each of which will be described in detail in the following sections. Two instruments were built, the first of which is described in detail in this thesis and was the original system developed (used in Chapters 3 and 4). The second system was used in Chapters 4

and 5 and had a number of modifications (discussed briefly in this chapter) with the most significant, being the migration to onboard FPGA processing.

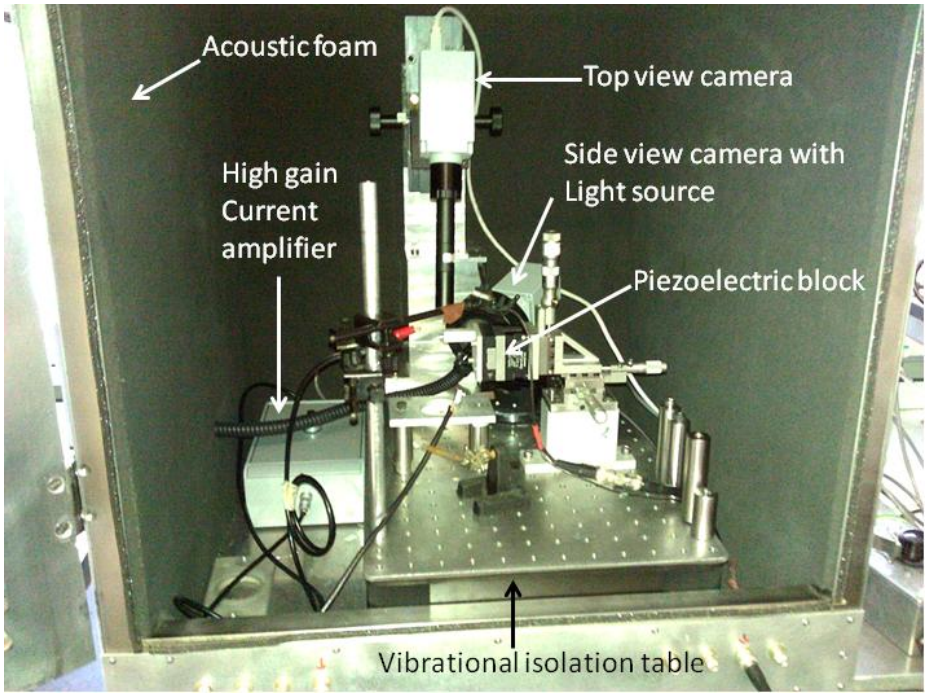

Figure 2-1: *An optical image of the instrument, showing the components used in SECCM.*

2.2 Hardware

2.2.1 Data Acquisition

Data acquisition (DAQ) refers to the process of acquiring signals, typically converting analog signals, to digital ones. This is usually achieved through the use of an analog to digital converter (ADC), converting the measured voltages into digital signals which can be read by a personal computer (PC). In cases where control of analog systems is required, a digital to analog converter is used (DAC), allowing the

manipulation of physical systems via software control. Typically both systems are embedded into one piece of hardware. DAQ cards interface with specific host software with the ability to choose specific channels to generate / acquire analog or digital signals. Each acquisition or output can be tuned in terms of frequency of collection / generation and also magnitude in the case of signal generation. One limitation of using DAQ cards is that the response time will depend on the PC and the operating system, arising from the fact that signal processing occurs on the central processing unit (CPU), and will depend on the number of operations being performed at that time. One way to overcome this problem, was to migrate to field programmable gate array (FPGA) based DAQ cards. This piece of hardware consists of a number of logic gates which can be wired up via the software loaded onto it. They can perform the same operations as traditional DAQ systems but at much higher execution rates as signal processing can be performed on board, buffering data to host software on the PC. This feature allows for much faster feedback loops and gives access to a number of inputs and outputs together with ADCs and DACs. However, this system involves more complex programming, with relatively long compile times, as the internal logic gates need to be reconfigured, but provides a more robust method for control systems where the response time needs to be very short and also allows the streaming of much more amounts of data with very little effort. The main system described herein used an NI FPGA (7830R) with the base code compiled on the card, programmed to operate as a DAQ card, i.e. all processing was done on the CPU. This was done so that only input and output commands were accessed through the FPGA allowing for the modification, or writing of new software to be much simpler.

2.2.2 Electronic Components

The system described herein required very sensitive, analog electronics that were developed by Dr. Alex Colburn. The system described in Chapter 3 is the first variation of the technique. In this setup a potential is applied to one QRCE 1 and the current at QRCE 2 is measured with respect to ground. The electrochemical current, at the surface, working electrode, is also measured with respect to ground (shown in Figure 2-2).

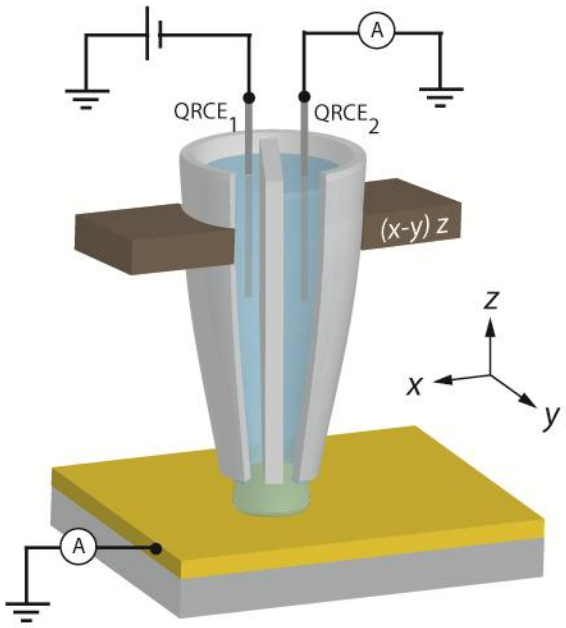

Figure 2-2: *A schematic of the original SECCM setup*.

The equipment used in Chapters 3 to 5, consisted of two separate modules: 1) A bipotentiostat type system, whereby a potential was applied between two QRCEs with a current measured between them, whilst the entire potential was floated with respect to ground, 2) the second component consisted of a high gain current

amplifier measuring signals with respect to ground and is the same equipment used on the setup described in Chapter 3. A schematic of the setup is shown in Figure 2-3.

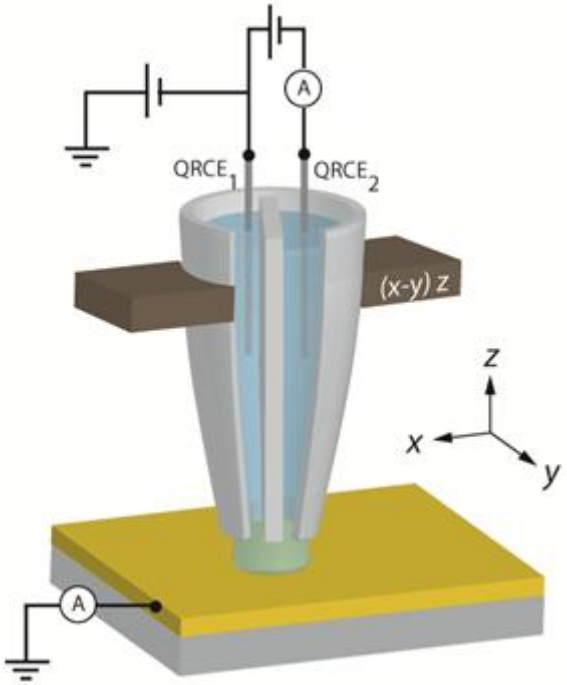

Figure 2-3: *A schematic of the revised SECCM setup*.

The first module allowed us to keep a constant potential between the two reference electrodes, with the ability to vary the potential with respect to ground. This enabled potential control of the conducting surface being studied, essential in making electrochemical measurements. The gain ranges went from 10 nA / V to 100 µA / V and had a bandwidth of around 10 kHz. This module also controlled the gains and supplied power to the second module. The electrochemical signals were then collected via a high gain, current amplifier allowing for measurements from the nanoAmp range down to the picoAmp range (1 nA / V to 1 pA / V) and had a bandwidth of 1 kHz.

2.2.3 Probe oscillation electronics

For the technique described it was necessary to oscillate the probe in a sinusoidal manner in the z direction. This required two pieces of external hardware: a wave generator and a signal adder. The wave generator supplied the sinusoidal signal used for the oscillation of the probe with the ability to tune frequency and amplitude and was either an external piece of hardware or built into a lock-in amplifier. The signal adder summed two signals a direct current (d.c.) and an alternating current (a.c.) signal, with controlled the motion of the probe. Simply this provided an a.c. signal with an underlying d.c. offset.

2.2.4 Lock-in Amplifier

In order to detect the a.c. signal arising from the modulation of the pipet probe a lock-in amplifier was used. Two types were used in the experiments described; a software version and an external piece of hardware (Stanford Research SR830). The software version was an attempt to have a cheaper and easily transferable system across different platforms but was limited to a frequency of approximately 80 Hz is described in detail.[1] This version was used for the experiments described in Chapters 3 and 4, whilst the rest of the experiments were done using the second developed system which used a hardware based lock-in. The operation of the hardware version will be briefly described herein.

A lock-in amplifier is used to detect a.c. signals as small as a few nanovolts. Using phase sensitive detection a single component can be extracted at a specific

reference frequency and phase. All other signals at different frequencies can be filtered out making it a very sensitive piece of equipment.

2.2.4.1 Phase Sensitive detection

In an experiment, a system is modulated at a fixed reference frequency and the experimental response is detected at this specific frequency. The signal is of the type $V_{sig}\sin(\omega_r t + \theta_{sig})$ where V_{sig}, is the amplitude of the signal, ω_r is the signal frequency and θ_{sig} is the phase. An example reference frequency and experimental response is shown in Figure 2-4.

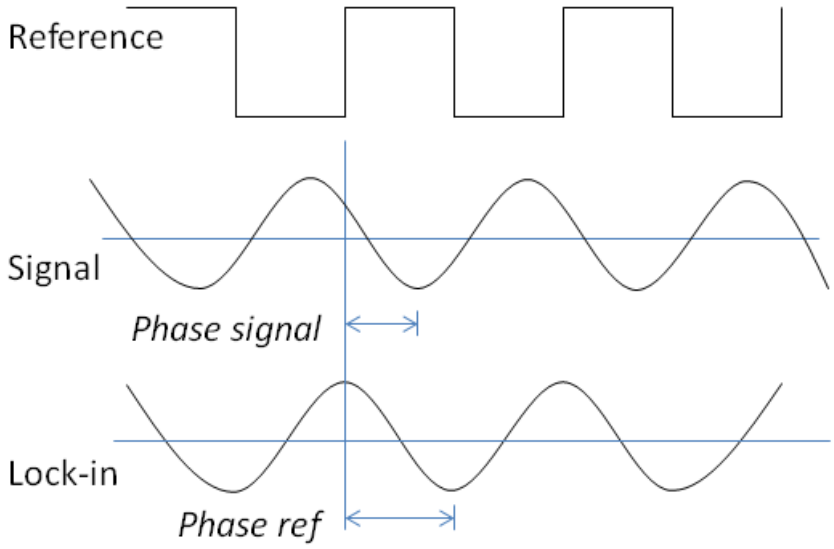

Figure 2-4: *A schematic of a reference signal applied to a lock-in amplifier, the lock-in signal after performing the phase locked loop and the experimental signal with a slight phase shift from the reference.*

A lock-in amplifier generates its own internal reference using a phase-locked-loop locked to the external reference frequency with the reference frequency given as

$V_L \sin(\omega_L t + \theta_{ref})$. The lock-in multiplies the amplified signal with the reference signal using the phase sensitive detector and the output is the product of two sine waves.

$$V_{psd} = V_{sig} V_L \sin(\omega_r t + \theta_{sig})(\sin \omega_L t + \theta_{ref}) \quad 2.1$$

$$= \frac{1}{2} V_{sig} V_L \cos([\omega_r - \omega_L]t + \theta_{sig} - \theta_{ref}) - \frac{1}{2} V_{sig} V_L \cos([\omega_r + \omega_L]t + \theta_{sig} + \theta_{ref})$$

The product is two a.c. signals; one is the difference of the two frequencies and the other the sum. This signal is then passed through a low pass filter and the ac signals are removed and in the case that $\omega_r = \omega_L$ the result will be a d.c. signal proportional to the signal amplitude.

$$V_{psd} = \frac{1}{2} V_{sig} V_L \cos(\theta_{sig} - \theta_{ref}) \quad 2.2$$

2.3 Actuation and positioning

2.3.1 Piezoelectric positioners

Piezoelectric actuators were necessary for fine control of the tip / sample positioning in *x*, *y* and *z* directions. A piezoelectric material is one which expands with an applied voltage by a very small amount or can generate a voltage with applied mechanical stress.[2-3] The original system used was based on a 3-dimensional cube actuator which controlled the motion of the probe in all three directions with a range of 100 μm (PI Nanocube P-611.35). The second system was developed where higher resolution peizoelectrics were used and consisted of mounting a standalone piezo for vertical motion 38 μm resolution (PI Lisa P-753.3CD), where the tip was

mounted, and an *x*-*y* scanner, 250 μm resolution (PI Hera P-621.2CD) where the sample was mounted. The latter system allowed for higher tip oscillation frequencies, up to a 400 Hz (dependent on the load), to be used avoiding any crosstalk between actuators, due to the physical oscillation.

Due to hysteresis commonly found in piezoelectric systems, the actual displacement was recorded by monitoring the values from a sensor built in to the piezoelectric block. These sensors can come in two forms: a strain gauge sensor, where a change in resistance is converted to distance from prior calibration from the manufacturer or a capacitative sensor, where the capacitance of two plates is converted into a distance. A piezoelectric actuator can be operated in two modes open loop or closed loop. In closed loop an internal feedback is used to maintain the required distance monitoring the position using the inbuilt sensors, or in open loop where the position is controlled directly by the voltage applied to the system. In this case the *x* and *y* piezoelectrics were always operated in closed loop and it was found that due to the mechanical oscillation the vertical (*z*) piezo operated more reliably in open loop with the feedback controlled directly from the control software on the pc. In open loop it is still possible to use the sensors as a measure of displacement and values were taken from there.

The piezoelectric actuators are controlled by a high voltage amplifier (PI E-664 for the Nanocube, E-665 for the Lisa, and E-625 for each axis in the Hera stage) receives either digital or analog inputs. An analog voltage from 0 V to 10 V was applied, where the latter corresponded to the maximum extension of the piezoelectric positioner, as it was easier to program than using the digital interface and was modular to any other type of piezoelectric actuator.

2.3.2 Micromanipulators

Micromanipulators consist of linear stages which are adjustable by hand. A set of three positioners were orthogonally mounted for coarse control of the pipet probe with either the *x*,*y*,*z* cube piezoelectric block or the standalone *z* piezoelectric actuator mounted directly onto them (Newport M-461). Accuracy is down to about 0.5 μm, similar to that of a Vernier scale, these can be seen in Figure 2-1 attached to the piezoelectric block.

2.4 Probes

2.4.1 SECCM probes

The probes used within all the projects consisted of theta capillaries pulled using a laser puller (Sutter Instrument P 2000). Pipets are pulled via laser heating of the capillary combined with a mechanical pull to the required dimensions. Depending on the diameter required either borosilicate glass (Harvard Apparatus, UK TGC 150-10) was used or quartz (Sutter Instrument QT 120-90-7.5). The capillary was mounted onto the holder and the pull could be tailored from the control panel, shown in Figure 2-5. The adjustable parameters on the laser puller allowed the user to tailor both the size and shape of the probe.

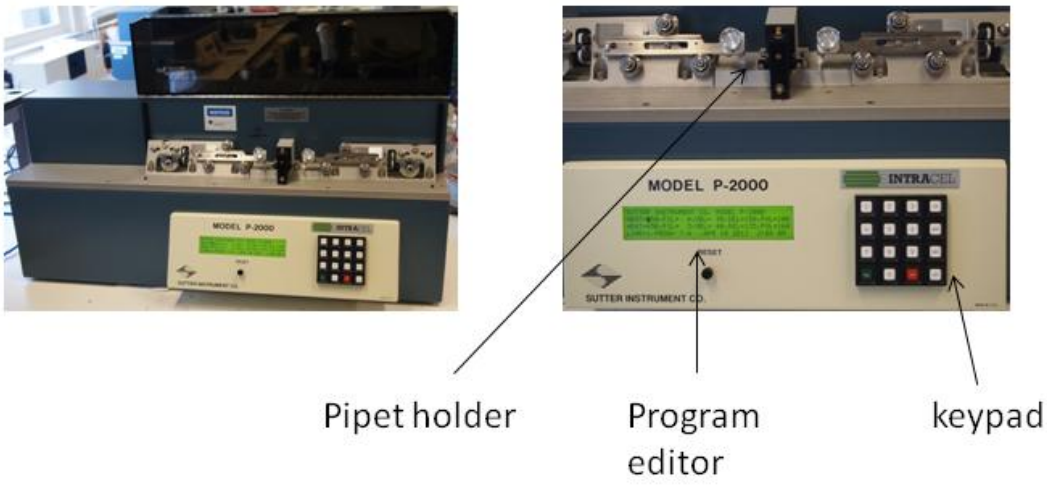

Figure 2-5: *An optical image of the laser puller with a zoom in, of the control panel*.

The five parameters are: heat, filament, velocity, delay and pull. The heat parameter controlled the heating temperature of the laser whilst the filament controlled the spot size of the laser onto capillary with smaller numbers indicating a smaller spot size. The velocity parameter controlled the speed of the mechanical pull, the delay controlled the delay time of the pull after the heating step and the pull controlled the force of the pull. Choosing each parameter carefully, the size and taper of the pulled capillary could be controlled and it was later found that by using a multi line program greater control and reproducibility of the pipets could be achieved. Typical multi line programs are shown below and were used to fabricate pipets with approximately 1 μm, 400 nm, 300 nm and 100 nm in diameter. Figure 2-6 a) shows an optical image of a 400 nm borosilicate probe, in which the effect of the multi line program can be seen optically as three distinctive regions. Figures 2-6 b), c) and d) show FE-SEM images of the 400 nm, 300 nm and 100 nm probes.

1 µm probes (borosilicate)

Line 1: Heat: 600 Fil: 4 Vel: 30 Del: 150 Pul: 20

Line 2: Heat: 500 Fil: 4 Vel: 30 Del: 150 Pul: 60

Line 3: Heat: 500 Fil: 3 Vel: 30 Del: 135 Pul: 60

400 nm probes (borosilicate)

Line 1: Heat: 600 Fil: 4 Vel: 30 Del: 150 Pul: 20

Line 2: Heat: 500 Fil: 4 Vel: 30 Del: 150 Pul: 60

Line 3: Heat: 500 Fil: 3 Vel: 30 Del: 135 Pul: 70

300 nm probes (quartz)

Line 1: Heat: 750 Fil: 4 Vel: 30 Del: 150 Pul: 80

Line 2: Heat: 650 Fil: 3 Vel: 40 Del: 150 Pul: 120

100 nm probes (quartz)

Line 1: Heat: 750 Fil: 4 Vel: 30 Del: 150 Pul: 80

Line 2: Heat: 650 Fil: 3 Vel: 40 Del: 135 Pul: 150

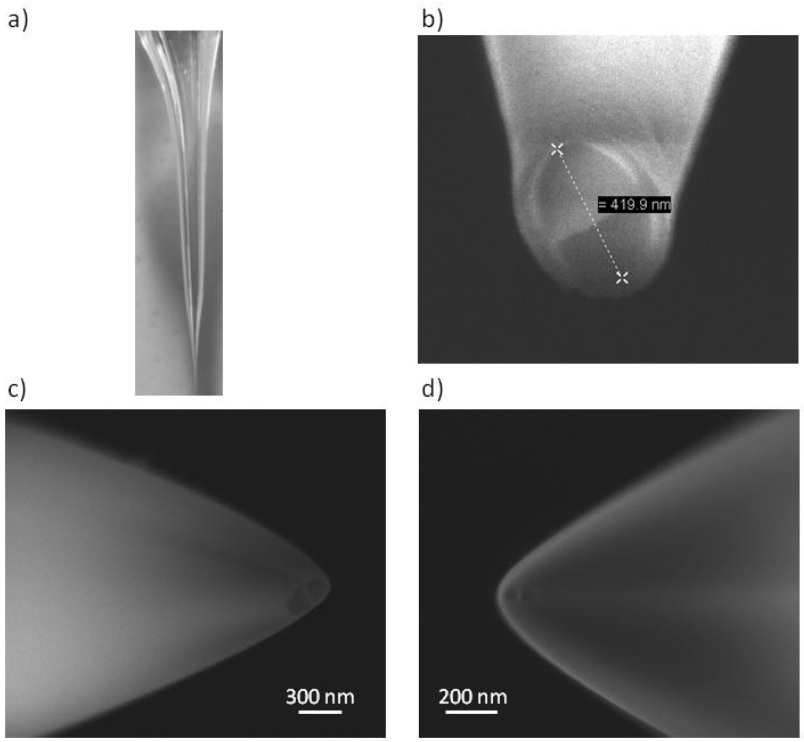

Figure 2-6: *Optical image a) of a pulled 400 nm,borosilicate theta pipet, b) the corresponding SEM image, c) an SEM image of a 300 nm quartz theta pipet and d) an SEM image of a 100 nm quartz theta pipet.*

As can be seen, for a borosilicate pipet, a progressive type program is used with the first line using a high heat as the glass is thickest at this stage and a relatively small pull. The second and third lines use less heat as the glass gradually becomes thinner but the pull parameter increases and in the final line the filament decreases and also the delay time. Increasing the pull parameter usually decreases the probe diameter but in some cases it is necessary to reduce the delay time in order to keep the symmetrical shape of the probe. Unfortunately, this can also increase the taper at the end of the probe. For the quartz pipets, two line programs were typically used, due to the high heat parameters used to melt the quartz, making it more difficult to design the overall size and shape. The first line heated and thinned the quartz whilst the second line controlled the size and shape at the end of the pipet. It

should also be noted that not all laser pullers are the same so direct transfer of pull programs did not achieve identical probes, but served as a good starting point.

2.4.2 SECM – SICM probes

SECM-SICM was introduced in Chapter 1. The type of probes used in this thesis, were the theta pipet type with one barrel filled with pyrolytic carbon. Probe preparation procedures were similar as those discussed in the previous section, with the exception that only quartz pipets could be used due to the pyrolytic step. An in-depth fabrication procedure will be discussed in Chapter 6 together with characterisation and some applications.

2.5 Optical visualisation

Initial probe positioning was achieved with the micromanipulators in conjunction with a camera system and light source. Two cameras were mounted in the setup described shown in Figure 2-1. The top camera (PixeLink PL-B776U, 6 megapixel) allowed for positioning of the probe over the sample whilst the side view camera (PixeLink, PL-B782U) allowed for careful positioning of the probe above the surface. The cameras were with various lenses depending on the magnification required.

2.6 Humidity Cell

A humidity cell was essential in the setup used as it minimised any evaporation occurring at the meniscus formed at the end of the pipet probe. The setup shown in Figure 2-7 consisted of an elevated sample holder within a Teflon cell, having an aqueous moat around it. This was sealed in a glass cover with the top open allowing for probe mounting.

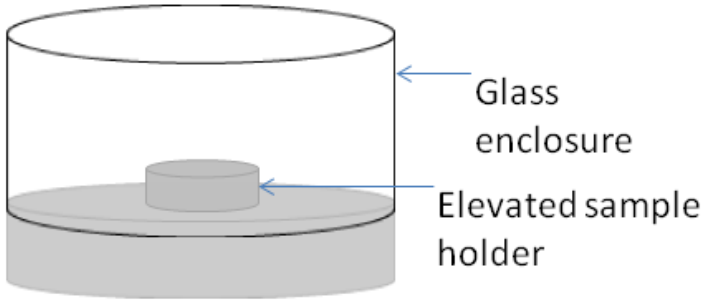

Figure 2-7: *A schematic of the humid cell used during experimentation. The sample is elevated so that a moat can be used to ensure a humid environment.*

2.7 Faraday Cage

It was essential that most of the system was mounted inside a grounded faraday cage due to the very low currents being measured, in some instances tens of fA. The faraday cage was also fitted with class O acoustic foam to reduce any acoustic vibrations, which was found to be essential when using nanometre sized probes, with the whole system mounted on top of a vibration isolation table and s shown in Figure 2-1.

2.8 Software

All software was written in National Instruments LabView 9.0, which is a graphical programming language and each program in known as a virtual instrument (VI). This software package was designed for scientists and engineers to easily design control systems for a multitude of instruments. Each VI consists of a front panel, which is the graphical user interface (GUI) whereby users can enter different parameters which control the experiment being performed. The code is written in the back panel in a graphical type format, whereby different low level modules are connected by wires interfacing with various inputs and outputs, including graphs, buttons dials etc. which are mirrored on the front panel. The system described in this thesis was a significant development of an earlier system designed for SICM.[4]

2.8.1 Basic SubVIs

SubVIs are usually basic programs which constitute the underlying operations of a more complex VI. Such operations include analog outputs, voltages, data acquisition etc. Most of the subVIs used in this thesis were pre-programmed with operations such as move piezo, outputting an analog voltage to the peizo amplifier, voltage outputs for potential control in electrochemical experiments, probe approach programs which combined data acquisition, piezo movement and also potential control. All these minor programs were then combined to make a higher level imaging program and a dual channel cyclic voltammetry (CV) program and are discussed in the following sections.

2.8.2 Scan Program

The scan program developed was used for experiments in Chapters 3 and 4, whilst the other Chapters used a newly developed version developed by Mr. Kim McKelvey, but will not be discussed in this thesis. The latter version made better use of the FPGA (NI 7852R) card allowing for faster scan speeds and much higher data acquisition rates. The initial scan program developed, operated on a move – stop – measure regime, with the data acquisition set at 25 Hz and in some occasions a 20 ms equilibration time was added before measurements were taken. The program controlled the vertical motion of the *z* piezo, moving at predefined steps, then stopping, acquiring data, processing and determining whether the stop parameter was above a predefined threshold, in this case the ac component within the ion current, between the channels in the theta pipet. Once surface contact was established a setpoint for feedback imaging was chosen by the user and the scan started. The probe was moved at predefined substeps in which only the vertical position was updated and these substeps were at a much closer spacing than those used for acquiring electrochemical data. This setup sped up the system slightly, also ensuring that the chances for tip crash were minimised. Due to the operation of the program scan times tended to be quite long ca. 1 hour for a 50 x 50 micron scan at 1 micron resolution, but experimental success rates tended to be quite high. The code was written to be as modular as possible and so other scanning techniques could also be performed including SECM and various modes of operation with very little programming effort.

The layout of the program consisted of two parts the front panel which contained the GUI and the back panel which contained the underlying code. The back panel was written to have a number of consecutive frames which controlled

each step in the imaging procedure. In total there were 7 frames, the first two set the piezo positions, so first centring the *x* and *y* piezos to allow positioning of the tip over the sample and then moving to the start positions, which were calculated from scan size and centre point. The third frame, called the approach program in which the parameters were all inputted into the GUI and the fourth frame built up ,the matrix in which the data would be saved. Frame 5 was the core of the scanning procedure where the feedback parameter was measured and piezo positions adjusted according to the feedback and this also contained subVIs in order to simplify the view of the program, an example is shown in Figure 2-8, which controlled the data acquisition and also calculated the feedback parameter. Frame 6 gathered the entire data set which was saved in a prebuilt matrix and written to a text file, whilst the last frame readjusted all the piezos to zero, occurring at the end of a scan.

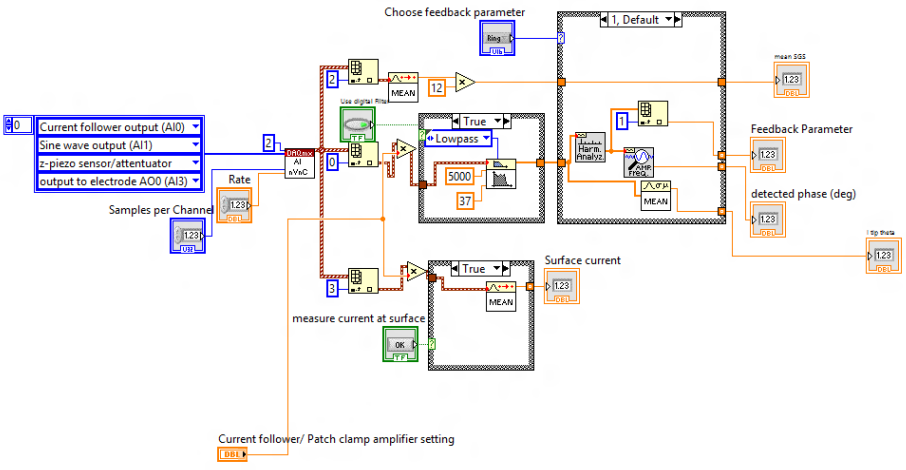

Figure 2-8: *A screenshot of the subVI called 'measure and analyse' and was part of frame 5. As can be seen input channels are split and processed relaying the data to the main GUI.*

The front panel or GUI was written to be as user friendly and intuitive as possible. Figure 2-9 shows a screenshot of the GUI. As can be seen it consisted of a number of different panels those that controlled the operation of the probe and those that plotted the processed data.

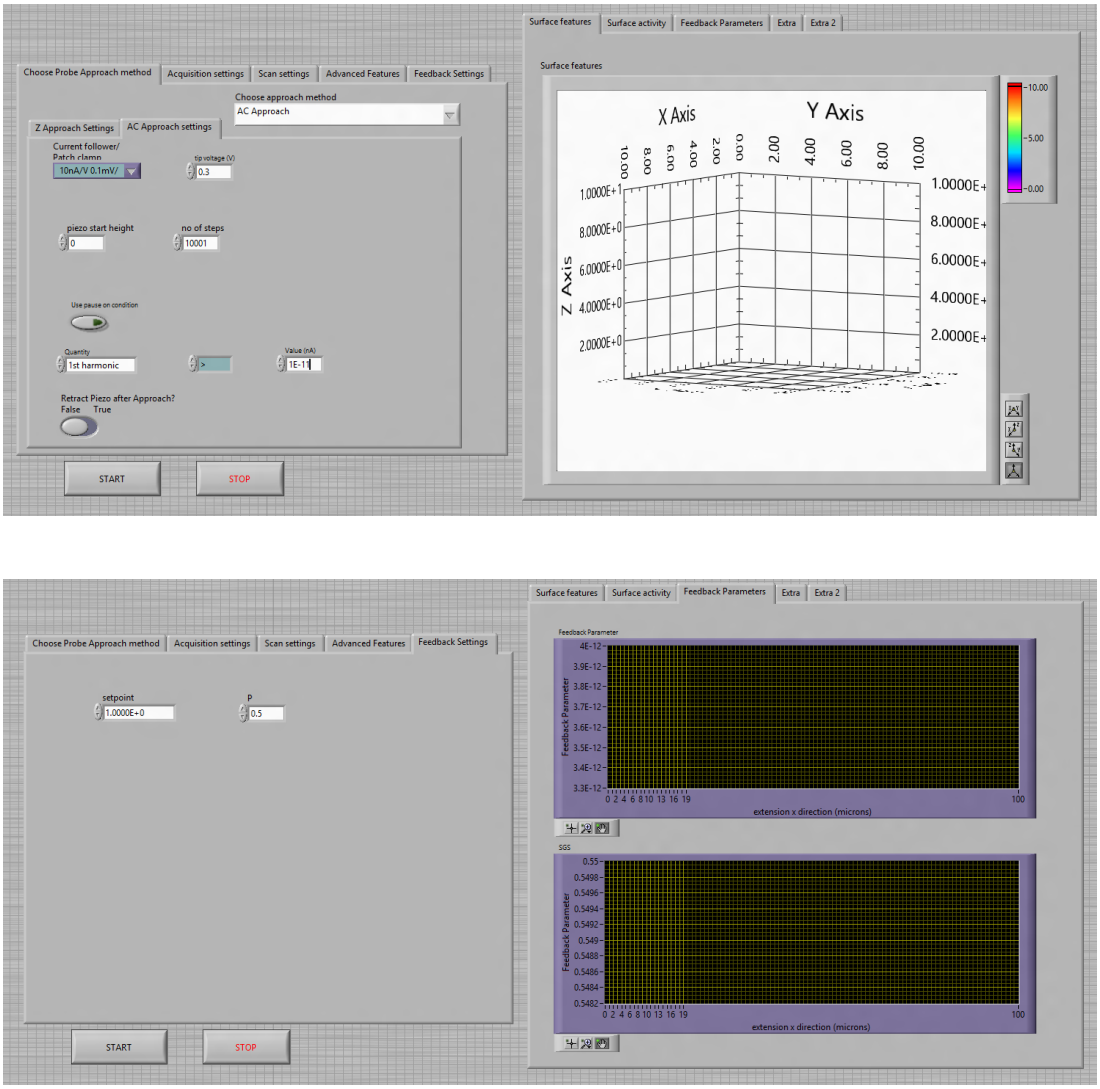

Figure 2-9: *Screenshots of different panels of the GUI. The top screenshot shows the approach settings and the graph in where 3-D topographical features could be seen. The bottom screenshot shows the feedback panel where the user could adjust the gains with the feedback parameter plotted in an x-y chart on the right.*

2.8.3 Dual Channel CV program

The dual channel CV program was a modified version of that described in the elsewhere.[1] Basically, the modification allowed for two input channels to be measured simultaneously, this included both the electrochemical current, at the surface working electrode, and the ion current between the channels in the pipet, essential for the experimental work done when comparing to a theoretical model.

2.9 Microscopy and spectroscopy

Characterisation methods included AFM, field emission scanning electron microscopy (FE-SEM), optical microscopy and Raman spectroscopy. Single walled carbon nanotube (SWNT) samples and graphene samples were both characterised with AFM and Raman spectroscopy, in conjunction with optical microscopy, in the case of graphene. FE-SEM and optical microscopy were used in the characterisation of electrochemical probes determining internal diameters and taper angles.

2.9.1 Atomic Force Microscopy (AFM)

The AFM used was a Veeco Multimode with a Nanoscope V controller, in a tapping mode configuration. This allowed for a high resolution, non-destructive characterisation of the SWNT and graphene samples. In the case of SWNT only the height data gave an accurate representation of the tube diameter; the lateral resolution was compromised by tip convolution effects.

2.9.2 Optical Microscopy

Optical microscopy was performed using an Olympus BH2 microscope with lenses giving overall an magnification from 50 x to 1000 x. SECCM probes with diameters of 1 μm or greater were routinely characterised when approximate dimensions were required, accurate characterisation of probe dimensions was performed using FE-SEM. Graphene samples were also characterised using optical microscopy as they are visible on a Si substrate, with a 300 nm layer of SiO_2 on top[5-6] (refer to Chapter 4).

2.9.3 FE-SEM

FE-SEM (Zeiss Supra 55 with variable pressure system) was used to accurately characterise the internal diameters of the theta electrochemical probes, together with wall thicknesses and also taper angles. Due to the nature of the probe material (both borosilicate and quartz) charging at the tip of the probe was common, so the probes had to be cut, giving an overall length of less than 1 cm, and coated in silver epoxy, leaving the end untouched. It should also be noted that two halves of the same capillary gave almost identical probes, an example of this is shown in Chapter 6 when preparing SECM-SICM electrodes. Accelerating voltages between 2 KeV and 5 KeV were used with a very short working distance, of 1 mm or less. Probes were also aligned at a slight angle to the detector in order to minimise charging and gain higher resolution. The smallest dimension measured was less than 20 nm and took several hours (Chapter 6).

2.9.4 Micro Raman Spectroscopy

Raman spectroscopy was essential in the characterisation of the carbon materials used. In the case of SWNTs the technique was used to determine the quality of the nanotubes under investigation and for the graphene substrate Raman spectroscopy gave information about the number of layers being studied and also the stacking order. The technique was also used to determine the quality of the carbon pyrolytically deposited in the SECM – SICM probes.

Micro-Raman (Renishaw in Via Micrscope coupled to a Leica microscope) was used to record spectra with a HeNe 633 nm Laser with 10 % attenuation, 2 mW power, 100 x objective lens for the graphene substrate and 514 nm Ar Laser 50 x objective lens for the SWNT substrates.

2.10 Materials synthesis and preparation

The carbon working electrodes fabricated in this thesis were synthesised using chemical vapour deposition (CVD) via a catalytic process for both SWNT[7] and graphene. The same setup was used with different catalytic materials used and will be discussed briefly in the following sections. Once synthesised, electrical contacts were made using a thin layer metallic deposition process.

2.10.1 Graphene synthesis and preparation

Graphene growth was carried out by evaporating a 300 nm nickel film (Minilab, Moorfields, UK) onto a Si / SiO_2 substrate. The sample was first annealed

by being placed in a chemical vapour deposition (CVD) furnace (Lindberg Blue Thermo, UK) and heated at 1000 ºC for 20 minutes, under a flow of 600 sccm Ar and 500 sccm H_2, improving the crystal quality and reducing surface roughness. A consequent flow of 1500 sccm and 14 sccm CH_4 was introduced into the chamber, inducing graphene growth, keeping a constant temperature of 1000 ºC for 10 minutes. The sample was then cooled to room temperature using a 2000 sccm Ar flow, with the entire process being performed under atmospheric pressure.[8] The graphene had to be transferred onto a new Si / SiO_2 support in order to remove any unwanted electrochemical contributions from the underlying nickel layer. This was performed by spin coating poly(methylmethacrylate) (PMMA) over the graphene / nickel/ Si / SiO_2 sample. The nickel layer was dissolved using an aqueous 1M $FeCl_3$ solution, releasing the PMMA / graphene film allowing it to be transferred onto a fresh Si / SiO_2 substrate. Once transferred the PMMA was dissolved in acetone.

2.10.2 SWNT synthesis and preparation

SWNT forests were grown on silicon wafers (n-type, 525 μm thick, IDB Technologies Ltd, UK) which had been sputtered (Plassys (MP 900S)) with a 10 nm layer of aluminium (Al) and cleaved into ~ 1 cm × 1.5 cm pieces. The individual substrates were ashed in an oxygen plasma for 2 minutes (K1050X plasma system, Emitech, UK; O2 pressure 6×10^{-1} mbar) and sputtered (Quorum Technologies SC7640 sputter coater, fitted with a Co target, 99.95%, Testbourne Ltd. UK) with Co. Once prepared, the substrates were heated to growth temperature (825 ºC) in a CVD oven consisting of a 1 inch diameter quartz tube (Enterprise Q ltd.) passing through a tube furnace (Lindberg/Blue M, Thermo-Fisher Scientific,

US). Heating was performed under hydrogen flow (99.995%, BOC). After the growth temperature was reached, argon (99.9995%, BOC) was bubbled through ethanol (99.99%, Fisher Scientific) at 0 °C before being introduced into the CVD system as the source of carbon. In both cases, the flow rates of the process gasses were controlled using mass flow controllers (MKS Instruments UK Ltd, UK). Growth was sustained for 40 minutes before the Ar-EtOH flow was stopped and the oven was allowed to cool under hydrogen flow.

2-D networks of SWNTs were grown by catalytic vapour deposition on a silicon / silicon oxide substrate (IDB technologies limited., n-type Si 525 μm thick with a 300 nm of thermally grown SiO2), and cleaved into ~ 1 cm × 1.5 cm pieces. The catalyst, horse spleen ferritin, was deposited on the individual substrates, by drop casting for 1 hour and were then ashed in an oxygen plasma for 2 minutes (K1050X plasma system, Emitech, UK; O2 pressure 6×10^{-1} mbar). Once prepared, the substrates were heated to growth temperature (700 ºC) in a CVD oven consisting of a 1 inch diameter quartz tube (Enterprise Q ltd.) passing through a tube furnace (Lindberg/Blue M, Thermo-Fisher Scientific, US). Heating was performed under hydrogen flow (99.995%, BOC). After the growth temperature was reached, argon (99.9995%, BOC) was bubbled through ethanol (99.99%, Fisher Scientific) at 0 °C before being introduced into the CVD system as the source of carbon. In both cases, the flow rates of the process gasses were controlled using mass flow controllers (MKS Instruments UK Ltd, UK). Growth was sustained for 10 minutes before the Ar-EtOH flow was stopped and the oven was allowed to cool under hydrogen flow.

2.10.3 Electrical contacts

Electrical contacts were made to all samples by partially covering the substrate with a shadow mask and a thin film of 3 nm Cr and 90 nm Au was thermally evaporated (Minilab Moorfields, UK). This procedure eliminated the need for any photolithographic steps which could leave residues on the samples as sometimes seen on carbon nanotubes.[9-10]

2.11 Chemicals and materials

Materials	Description
SWNT / Graphene growth substrates	
Si / SiO_2 wafers	4", 525 μm thick, <100>, resistivity 1-10 Ω cm, n-type, single side polished, 300 nm thermally grown oxide, IDB Technologies Ltd., UK
Solvents	
Ethanol	99.99% Fischer Scientific Ltd., UK
Gases	
Argon	99.9995%, BOC Gases, UK
Hydrogen	99.95%, BOC Gases, UK
Oxygen	99.5%, BOC Gases, UK
Catalyst for SWNT growth	
Horse spleen Ferritin	50 - 150 mg mL^{-1} in 150 mM aqueous NaCl, Sigma-Aldrich Co., UK
Thermal evaporation	

Gold wire	99.99% and 99.95%, Goodfellow, Cambridge, UK
Chromium bar	Cr coated tungsten rod, 99.9%
Reference electrodes	
Silver Wire	99.99% Ø 0.25 mm, Goodfellow, Cambridge, UK
Capillaries	
Borosilicate theta glass capillaries	1.5 mm outer diameter x 0.23mm inner diameter with 0.17 mm septum, TGC 150-10, Harvard Apparatus ltd. USA
Quartz theta capillaries	1.2 mm outer diameter 0.9 mm inned diameter, QT 120-90-7.5, Sutter instrument, USA
Chemicals	
Ruthenium (III) hexamine trichloride $Ru(NH3)_6^{3+}Cl_3^-$	99%, Stem Chemicals Ltd., UK
Ferrocenylmethyltrimethylammonium hexafluorophosphate, $FcTMA^+PF6^-$	Metathesis of $FcTMA^+I^-$ with $Ag^+PF_6^-$
Ferrocenylmethyltrimethylammounium $FcTMA^+I^-$	99%, Stem Chemicals Ltd., UK
Silver hexaflourophosphate, $Ag^+PF_6^-$	99%, Stem Chemicals Ltd., UK
Sodium chloride, NaCl	99%, Sigma Aldrich Co, UK
Potassium chloride, KCl	99%, Sigma Aldrich Co, UK

2.12 References

(1) Edwards, M. A., PhD thesis, University of Warwick, 2008.

(2) de Gironcoli, S.; Baroni, S.; Resta, R. *Phys. Rev. Lett.* **1989**, *62*, 2853.

(3) Cady, W. G. *Piezoelectricity*; McGraw-Hill: New York, 1946.

(4) Edwards, M. A.; Williams, C. G.; Whitworth, A. L.; Unwin, P. R. *Anal. Chem.* **2009**, *81*, 4482.

(5) Blake, P.; Hill, E. W.; Neto, A. H. C.; Novoselov, K. S.; Jiang, D.; Yang, R.; Booth, T. J.; Geim, A. K. *Appl. Phys. Lett.* **2007**, *91*.

(6) Ni, Z. H.; Wang, H. M.; Kasim, J.; Fan, H. M.; Yu, T.; Wu, Y. H.; Feng, Y. P.; Shen, Z. X. *Nano Lett.* **2007**, *7*, 2758.

(7) Edgeworth, J. P., University of Warwick, 2009.

(8) Reina, A.; Jia, X.; Ho, J.; Nezich, D.; Son, H.; Bulovic, V.; Dresselhaus, M. S.; Kong, J. *Nano Lett.* **2009**, *9*, 30.

(9) Heller, I.; Kong, J.; Heering, H. A.; Williams, K. A.; Lemay, S. G.; Dekker, C. *Nano Lett.* **2005**, *5*, 137.

(10) Dudin, P. V.; Snowden, M. E.; Macpherson, J. V.; Unwin, P. R. *Acs Nano* **2011**, *5*, 10017.

CHAPTER 3

Localised High Resolution Electrochemistry and Multifunctional Imaging: Scanning Electrochemical Cell Microscopy

In this chapter a methodology for highly localized electrochemical measurements and imaging is described using a simple, mobile theta pipet cell. Each channel (diameter <500 nm) of a tapered theta pipet is filled with electrolyte solution and a Ag/AgCl electrode, between which a bias is applied, resulting in a conductance current across a thin meniscus of solution at the end of the pipet, which is typically deployed in air or a controlled gaseous environment. When the position of the pipet normal to a surface of interest is oscillated, an oscillating component in the conductance current is generated when the meniscus at the end of the probe comes into contact with the surface and undergoes periodic (reversible) deformation, so as to modulate the solution resistance. This oscillating current component can be used to maintain gentle contact of the solution from the pipet cell with the surface and as a set point for high resolution topographical imaging with the pipet. Simultaneously, the mean conductance current that flows between the pipet channels can be measured and is sensitive to the local nature of the interface, informing one, for example, on wettability and ion flow into or out of the surface investigated. Furthermore,

conductor or semiconductor surfaces can be connected as a working electrode, with one of the electrodes in the pipet serving as a QRCE. This pipet cell then constitutes part of a dynamic electrochemical cell, with which direct voltammetric-amperometric imaging can be carried out simultaneously with conductance and topographical imaging. This provides multifunctional electrochemical maps of surfaces and interfaces at high spatial resolution. The prospects for the use of this new methodology widely are highlighted through exemplar studies and a brief discussion of future applications.

3.1 Introduction

Among scanned probe microscopies (SPMs), electrochemical microscopies, such as scanning electrochemical microscopy (SECM),[1-5] have attracted considerable attention as a means of mapping the function, as well as topography of a wide range of surfaces and interfaces. Amperometric SECM generally employs a working electrode tip, as part of an electrochemical cell, in which an electrolyte solution bathes the entire sample of interest[1]. Variants of amperometric SECM including SECM- atomic force microscopy (AFM)[6-11] and SECM- scanning ion conductance microscopy (SICM)[12-13] operate with similar electrochemical principles but provide a feedback mechanism so that surface activity and topography can be mapped simultaneously. These techniques are discussed in detail in Chapter 1.

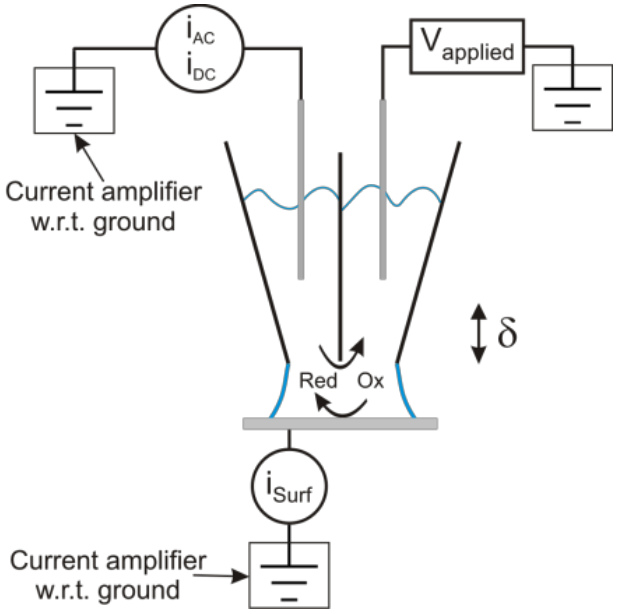

Figure 3-1: *Schematic (not to scale) of the theta pipet system which serves as a localized conductivity cell (measurement of i_{DC} and i_{AC}) and for conducting/semiconducting surfaces as a local dynamic electrochemical cell (i_{surf}).*

Herein, a new technique is described, scanning electrochemical cell microscopy (SECCM), which utilizes a theta pipet electrochemical cell (figure 3-1) for the simultaneous measurement of the topography and local functional properties of interfaces. The basic idea is to apply a potential between two Ag/AgCl (or similar) electrodes, one in each channel of a tapered glass theta pipet filled with (aqueous) electrolyte solution. The perpendicular position of the probe (normal to the surface of interest, typically in air or another environment) undergoes a small amplitude oscillation, and the conductance current response is measured and utilized for high resolution functional and topographical imaging. When the electrolyte solution, at the end of the pipet, just comes into contact with a surface, the periodic (reversible) deformation of the meniscus formed between the pipet and surface modulates the solution resistance and, thus, the DC current, giving rise to an alternating current,

i_{AC}, which is not experienced when the pipet is away from the surface. Thus, i_{AC} can be measured and used as a set point to ensure contact of the electrochemical cell with the surface. Simultaneously, one can measure the mean, or direct, conductance current, i_{DC}. As well as depending on the meniscus geometry and size, i_{DC} is sensitive to the surface properties. For example, an ion flow, from the solution in the pipet, into the surface will cause a decrease of the local electrolyte concentration at the end of the tip, thus increasing the resistance (decreasing i_{DC}). By measuring both i_{AC} and i_{DC}, it is, thus, possible to carry out functional imaging of interfaces with this simple high resolution conductivity cell. For (partially) conductive surfaces, it is possible to further use the pipet as a local dynamic electrochemical (voltammetric-amperometric) cell, where the sample is a working electrode and one of the pipet electrodes is a quasi-reference electrode. Again, i_{AC} can be used for positioning; i_{DC} informs one on local conductance and, hence, the properties of the interface, but one can also measure the current through the sample directly due to surface redox processes, double layer charging, for example. This aspect of the technique builds significantly on the scanning microcapillary contact method (SMCM),[14] but the additional i_{DC} and i_{AC} measurements in SECCM allows for superior control of the tip position, provides for much faster imaging, and yields considerably richer data on surface properties, as demonstrated in this chapter.

A modulated probe of the type employed herein has been used previously to trace the topography of surfaces (via i_{AC}) and to carry out local deposition of proteins,[15-16] but it has not been recognized that i_{DC} will also be very sensitive to the local environment of the probe, allowing functional imaging which is the central premise of this chapter. Furthermore, there are no previous reports of surface electrochemical imaging using the methodology described. Among many advantages

of SECCM are the fact that: (i) only the part of the surface of interest that is imaged or probed comes into contact with solution, for a very brief time, which is particularly useful for systems where surface passivation, fouling, corrosion, etc. are otherwise problematic; (ii) a defined portion of the surface is targeted and isolated for investigation, free from the influence of neighboring areas, which can sometimes complicate SECM measurements; and (iii) the interfacial reaction or property is probed directly, with minimal convolution from tip and topographical effects.

3.2 Experimental

3.2.1 SECCM setup

Refer to Chapter 2 for a detailed description of the technique.

3.2.2 Sample preparation

As a model substrate, a structure comprising of 25 μm wide gold bands, separated by 20 μm, with a thickness of approximately 200 nm, were prepared on a glass microscope slide using photolithography. Glass microscope slides were also used for some approach curve measurements. Bovine dental enamel lesions were prepared by standard methods,[17] so that a demineralized sub-surface zone was created below an intact mineralized surface that was imaged.

3.2.3 Solutions and chemicals.

Aqueous solutions were prepared using Milli-Q reagent water with a resistivity ca. 18.2 MΩ cm at 25 °C. Solutions used to fill the theta pipet were either 20 mM KCl (Fischer Scientific) or 1 mM calcium dihydrogenphosphate monohydrate (Sigma

Aldrich), adjusted to pH 7. For electrochemical measurements a redox mediator, trimethyl(ferrocenylmethyl) ammonium ion, $FcTMA^+$ (2 mM) was added to the 20 mM KCl solution. For some studies, the enamel surface was treated with $ZnCl_2$ (5 mM, Sigma Aldrich).

3.3 Results and discussion

3.3.1. Tip approach measurements.

The pipet tip was translated through air toward a glass surface (in 10 nm steps), while the positioner was oscillated in the z-direction with an amplitude $\delta = 50$ nm and frequency of 70 Hz. Figure 2a shows the i_{DC} and i_{AC} conductance current responses as a function of piezoelectric positioner extension (z-approach curves), until surface contact was achieved and the motion of the probe ceased automatically by the control program. It can be seen that, when the probe is away from the surface, i_{DC} ca. 50 pA flows, but i_{AC} is negligible, ca. 5 pA, with the finite value most likely due to leakage current or the relatively short time constant setting of the lock-in amplifier. Importantly, these currents stay essentially constant with z-piezoelectric extension, indicating that the humidity chamber minimizes any evaporation effects, until the pipet cell senses the surface, via contact of electrolyte confined to the end of the pipet, and then both components increase significantly (note the $\log_{10}$ scale on the current axes). The increase in i_{DC} is attributed, mainly, to an increase in the thickness of the liquid layer at the pipet end, due to wetting of the surface, whereas i_{AC} increases due to the periodic oscillation of the solution, in contact with the surface, due to the oscillating probe. The pipet cell could readily be detached from the surface by reversing the z-motion and both i_{AC} and i_{DC} returned to their original

values, indicating that the tip was not damaged when interacting with the surface. The data in figure 3-2 and subsequent images are representative of many tens of experiments carried out over a period of many months.

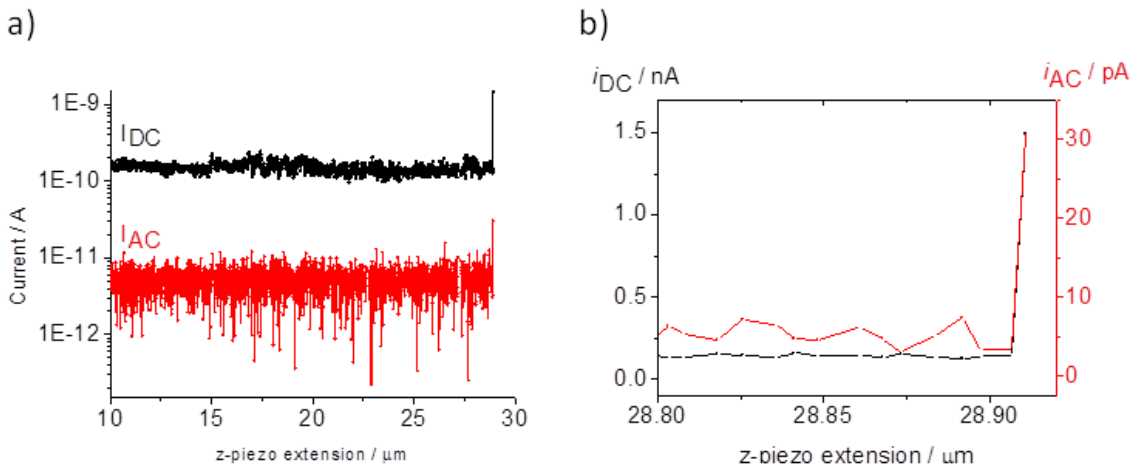

Figure 3-2: a) *Typical pipet approach data showing i_{DC} (black) and i_{AC} (red) as a theta pipet was translated towards a glass surface, until surface contact was made. A bias of 500 mV was applied with 20 mM KCl in the pipet. Note the log current scale. b) A zoom of the final few points of i_{DC} and i_{AC} until contact of the electrolyte from the pipet cell with the surface.*

3.3.2 Imaging with SECCM.

For imaging, a user defined set-point for i_{AC}, of about an order of magnitude greater than the background value with the probe away from the surface, was employed to maintain electrolyte from the probe just in contact with the surface. A grounded substrate comprising of gold bands on glass is first considered. The theta pipet contained 20 mM KCl and a 500 mV bias was applied between the pipet channels (for consistency with the surface amperometric imaging reported in the following section; see below). Using i_{AC} as a set-point, the electrolyte meniscus at the end of the probe maintains contact as it is scanned over the surface and

topographical features are, thus, mapped out from the changes in the z-piezoelectric positioner. It is clear that the sample is at a slope of ca 2º; but even with this tilt, gold bands of 200 nm in height are evident (figure 3-3 a)). This is even more noticeable on the plane-fit image (Figure 3b) which highlights convincingly the capability of this method to trace surface topography. Note that the lateral resolution of the technique is high; the 25 μm wide bands and 20 μm pitch are faithfully reproduced. This is consistent with deposition experiments which highlight the high spatial resolution of this type of probe.[15-16]

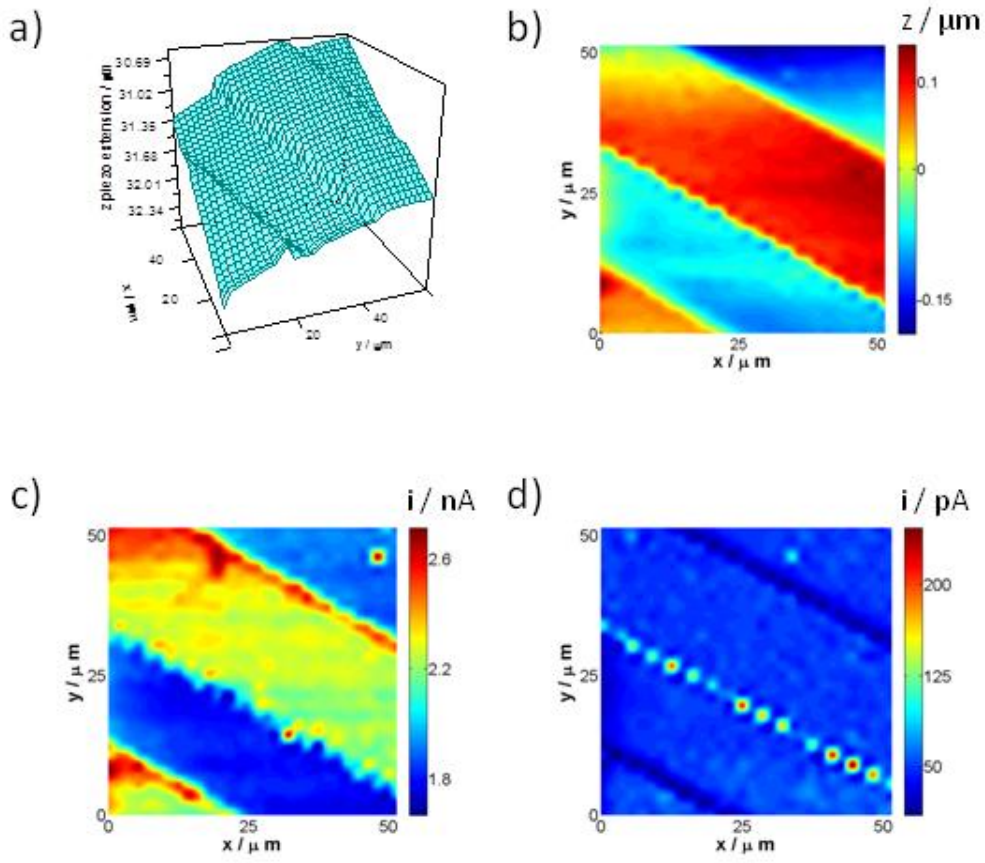

Figure 3-3: *SECCM images of gold bands on glass. (a) 3D topography of the sample. (b) Plane fitted topographical data from (a). (c) i_{DC} image in which the gold bands show higher current than the glass surface. (d) Corresponding value of i_{AC} (set-point) during imaging.*

The i_{DC} image (Figure 3c), clearly highlights that this quantity responds to the different materials that make up the substrate. Over the glass region, i_{DC} is ca. 1.8 nA, but in the vicinity of the gold bands this value increases by about 400 pA to 2.2 nA. This small, but readily detected and consistent change is attributed to electrowetting of the gold surface. The heterogeneity in i_{DC} over the gold band is most likely due to small variations in the gold surface, as no attempt was made to clean the substrate before use. When the gold structure was unbiased (not grounded), there was no detectable difference in the value of i_{DC} between the gold and glass areas.

The i_{AC} (error) image, shown in Figure 3d, indicates that surface contact is maintained throughout imaging; the variation in the locked-in amplitude is reasonably consistent over most of the region imaged. However, this (error) image also shows that at the leading boundary between the glass and gold (each line scan is across x from left to right at y positions separated by 1 μm, starting at $x = 0$; $y = 0$), the current attains values above the average set-point while at the trailing edge (with respect to x-scan direction) between the gold and glass lower values are seen. This is expected given the change in i_{DC} in the two regions, which was noted above. An important consequence of the variation in i_{DC} (and i_{AC}) across the substrate is that the tip will not necessarily strictly map the surface topography, as implied in earlier work,[15-16] but nonetheless provides a reasonable representation of it (as highlighted in figure 3-3 a),b)).

3.3.3 Surface amperometric imaging.

Direct amperometric imaging of electrode surfaces is demonstrated, by measuring the current through a conductive substrate surface, i_{surf} , during the imaging process (simultaneously with i_{DC} and i_{AC}; these are not considered further as they were essentially as already described). Figure 4a shows the i_{surf} response when the microband array substrate was held at ground and the quasi-reference electrode was at -500 mV. For these measurements, the pipet again contained 20 mM KCl, but there was no delay in reading the current immediately after the probe was moved to each fresh spot on the surface.

When the pipet is in the region of the glass, no current flows through the surface, as expected, but over the gold band a net current of 2 pA flows (average of 1000 data points measured at 25 kHz, 40 ms duration) when the electrolyte comes to a fresh portion of the gold surface. This current can be attributed to local double layer charging and other surface electrochemical processes. Figure 3-4 b) employs the same approach as in figure 3-4 a), but a redox mediator ($FcTMA^+$) was introduced into the electrolyte solution in the pipet. The applied potential (-500 mV to the quasi reference electrode, with the substrate at ground) was such that $FcTMA^+$ would undergo a one-electron, diffusion limited oxidation at the gold electrode surface. It can clearly be seen that the current is enhanced by about an order of magnitude, as a consequence. Except at the leading edge, where the current attains the highest values (corresponding to transient diffusion controlled oxidation of $FcTMA^+$), the value measured over most of the band attained a steady value of ca. 25 pA, consistent with values determined by point-by-point (steady-state) voltammetric measurements and in line with theory for a similar sized (overall) single channel pipet. [7]

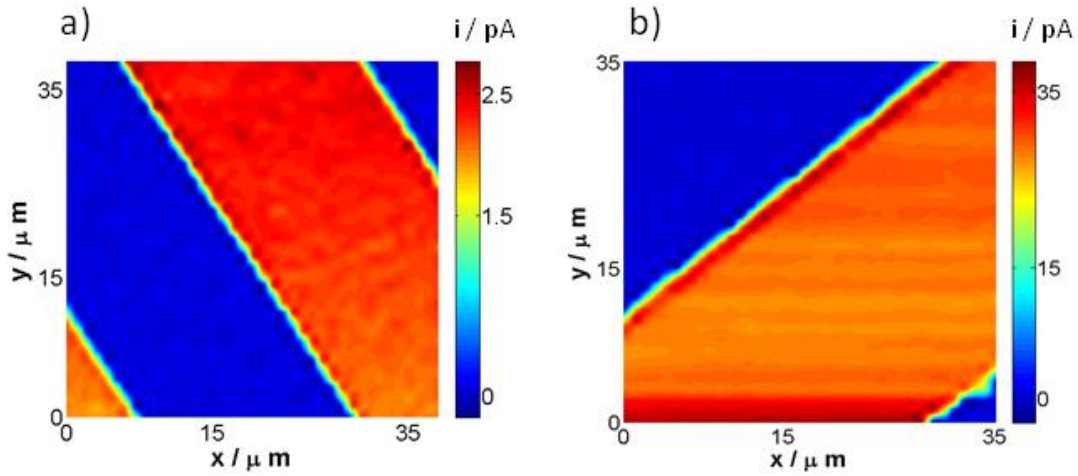

Figure 3-4: *(a) Surface current maps of the gold band structure. (a) 20 mM KCl; (b) 2 mM FcTMA$^+$, 20 mM KCl. The substrate was at biased at +500 mV with respect to the Ag/AgCl quasi-reference electrode.*

3.3.4 Mapping of ion fluxes into biominerals.

A biomineral surface was considered for imaging, specifically the surface of dental enamel, with a lesion sub-surface which promotes remineralization via the uptake of calcium phosphate.[12] Images were acquired using 1 mM calcium dihydrogenphosphate monohydrate (pH 7) in the pipet, to provide the source of calcium phosphate. The topographical (feedback-control) data, figure 3-5 a), show that SECCM copes well in tracking a very rough surface. The most important data, however, are in the i_{DC} map, where current values vary significantly across the surface (compared with the much smaller variation of i_{DC} seen over the glass regions in Figure 3c for example). The low i_{DC} values were attributed to regions where there is ion flow from the pipet into the sample, decreasing the electrolyte concentration in the meniscus. This effect was confirmed by treating the sample with $ZnCl_2$ (5 mM)

for 5 minutes, to exchange the surface Ca^{2+} for Zn^{2+} [18-19] which passivates the enamel surface towards the uptake of calcium phosphate, but is not expected to affect local wetting significantly. When the surface was re-imaged, i_{DC} values were much higher and more constant, ca. 2.7 ± 0.2 nA, attributed to much less (if any) transfer of electrolyte into the treated sample. Furthermore, as an additional control, a glass (inert) substrate was imaged with the same solution in the pipet: the values of i_{DC} were consistent to ±5% of the mean value, confirming our observations that the variation in i_{DC} on the enamel surface was due to variation in local ion uptake.

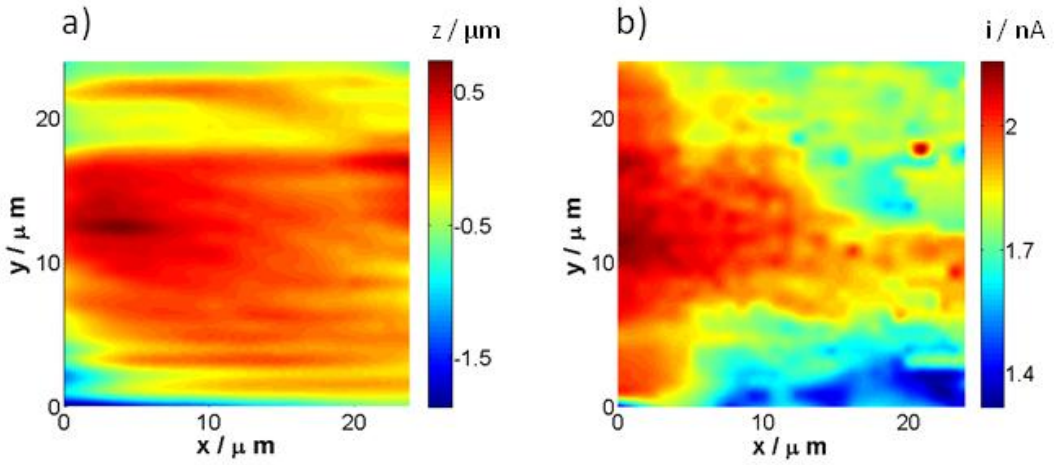

Figure 3-5: *Topographical image (a) of the enamel surface (plane fitted) and (b) corresponding i_{DC} image of the same region acquired simultaneously*.

3.4 Advances in SECCM

The methodology described above was further developed to allow independent potential control of the substrate without affecting the bias between the two quasi reference electrodes. An electrical diagram of the setup is shown in figure 3-6 a). This was made possible by electronics designed by Dr. Alex Colburn and described in chapter 2. Controlling the bias between the two QRCEs also meant that the ion migration could be tuned allowing us to access much higher mass transport

rates. This new system was modeled using a Finite Element Method (FEM) model developed by Dr. Michael E. Snowden allowing the determination of heterogeneous electron transfer kinetics, tip sample separations derived from the ac and dc currents, etc. Full details of the model can be found elsewhere[20] and only a brief description will be given in the following section, as the simulation itself goes beyond the scope of this thesis, but is useful in identifying some of the key features of SECCM.

3.4.1 FEM model

All simulations were performed using Comsol Multiphysics 4.1 (Comsol AB, Sweden) with Matlab 2009 (Mathworks Inc., Cambridge) interface. Figure 3-5a shows an electrical diagram of the simulated system identifying the variable parameters used in the simulation, these being the applied potential (E_t) and (E_b) the taper angle of the pipet (Θ) (measured using FE-SEM), the radius of the pipet (r_p), the septum width (t_w), the meniscus width (m_w) and height (m_h).

Figure 3-6 b) shows the simulated domain taken around a central plane of symmetry and was done to enhance computational efficiency. The domains are split into two sections ‘upper’ and ‘lower’ and in order to split the mesh used for simulation, as it was found that the lower part of the pipet dominated most of the response.

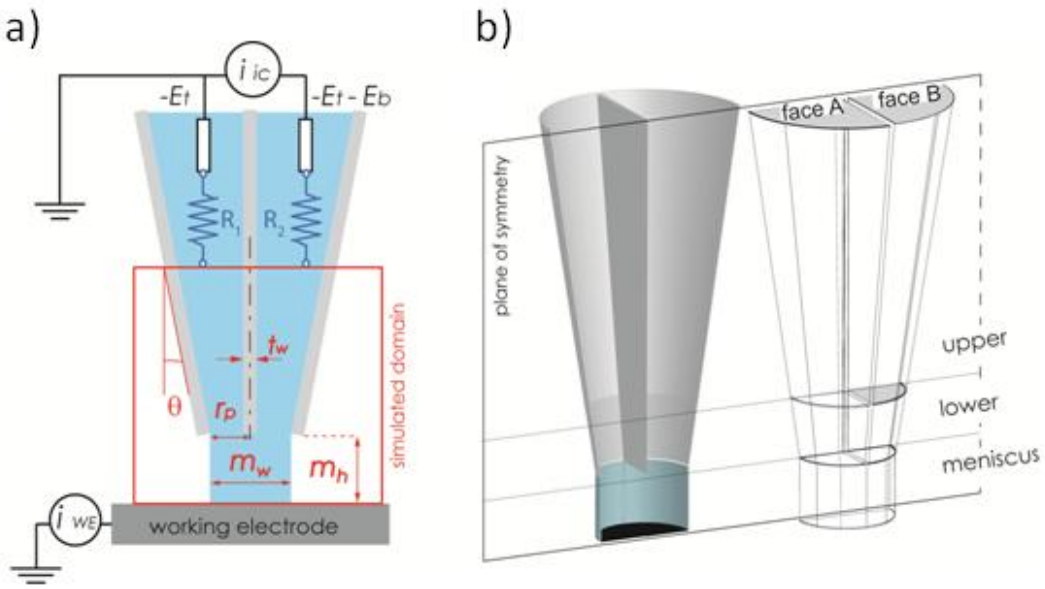

Figure 3-6: *Schematics of (a) the SECCM setup showing key geometric dimensions and electronic circuits and (b) the simulation domain. Not to scale.*

The ion current response between the two QRCEs was simulated using the time dependent Nernst-Planck equation (eq 3-1) with electroneutrality (eq 3-2) and was solved for all species inside the pipet

$$\frac{\delta c_j}{\delta t} + \nabla(-D_j \nabla c_j - z_j u_j F c_j \nabla V) + \mathbf{u}\nabla c_j = 0 \qquad 3\text{-}1$$

$$\sum_j z_j c_j = 0 \qquad 3\text{-}2$$

where c_j is the concentration, D_j is the diffusion coefficient, z_j is the charge, u_j is the ionic mobility of species, t is the time, F is the Faraday constant, V is the electric field provided by E_b in figure 3-6 a) and **u** is the velocity vector of the solution inside the pipet. Due to the high rates of migration found within the ensemble, it was reasonable to ignore any convective terms.

The simulation was then extended to include an electrochemical reaction at the working electrode denoted as w_e in figure 3-6 a), in this case was for the one electron oxidation of trimethyl(ferrocenylmethyl) ammonium hexafluorophosphate (2 mM) in KCl (50 mM). All simulations were compared to experimental data performed by approaching the pipet towards a highly oriented pyrolytic graphite (HOPG) (SPI supplies, West Chester, PA – SPI1) working electrode substrate, without modulation. Current-Voltage curves were then performed at the surface monitoring the effect of the bias on both the ion current and electrochemical currents, shown in figure 3-7. Modulated approach curves were also simulated and were essential in determining the tip sample separation. As the probe moved closer towards the surface a decrease in the ion current was observed together with an increase in ac amplitude, but the effect on the ion current was found to be significant only when the separation was in the range of half a pipet radius or less.

Figure 3-7 a) and b) show that there is a good agreement between the experimental response of the ion current (i_b) and theoretical one show an increase with applied potential between the two QRCEs, exhibiting an ohmic response. Figures 3-6 c) and d) show the simultaneous surface electrochemical response showing an increase in the limiting current with increasing bias potential E_b, between the two QRCEs in the pipet. This occurs due to an increase migration of charged species (redox mediator) towards the electrode surface, going from a diffusion limited regime, in the case of no bias applied, to a combined diffusion and electromigration system. The simulated electrochemical response fits very well with experimental showing that the migration, hence mass transport of species can be controlled with the applied bias potential. Figures 3-7 e) and f) show the response of

the ion current i_b with a variation consistent with the counter reaction (i_c) occurring at the second QRCE. Compared to the overall current magnitude this effect is found to negligible but can also be accounted for again fitting well with the theoretical response.

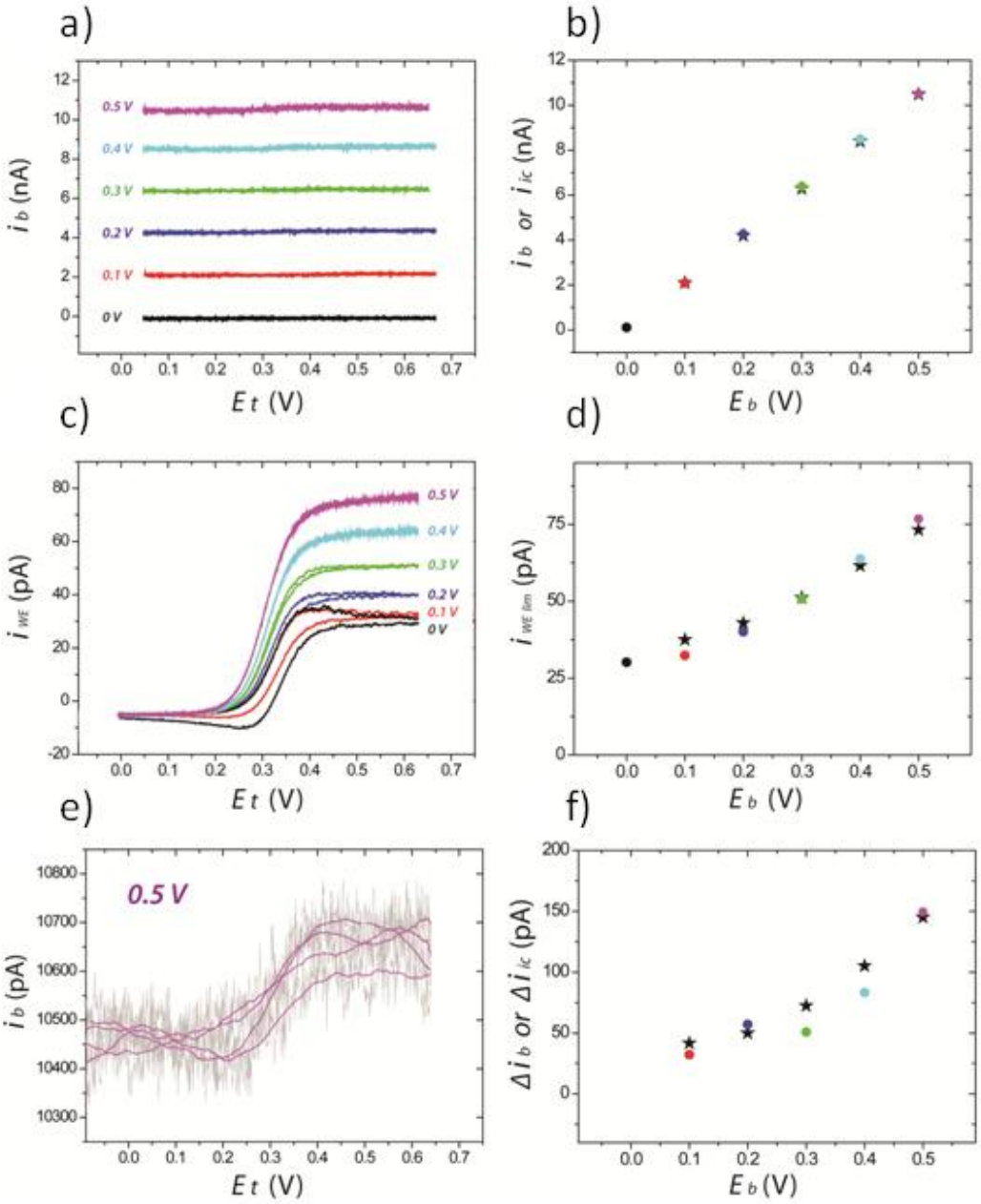

Figure 3-7: *Simultaneously recorded ion conductance currents (a,b) and the working electrode response (c,d) during CV measurements (v = 100 mVs^{-1}) for the $FcTMA^{+/2+}$ couple on HOPG. The currents between the two QRCEs in each barrel (experimentally and i_b and simulated i_{ic} (a,b)) and the working electrode response (i_{WE} and $i_{WE,lim}$) were recorded as a function of E_t for different values of E_b between 0 and 0.5 V (marked on (a) and (c)). The probe was defined by r_p = 0.6 μm and Θ = 8.5, m_h = 0.15 μm filled with 2 mM $FcTMA^+$ and 50 mM KCl. Plot (e) is a magnified view of the ion current between barrels, i_b, at bias 0.5 V (from plot (a)), where a change in i_b is observed during voltammetry. The change in i_c during voltammetric sweeps is plotted as a function of the bias potential for experimental and simulated data sets (f). Experimental (colored circles) and simulated data (stars) are plotted for (b), (d), and (f).*[20]

3.5 Conclusions

SECCM allows high resolution electrochemical measurements (conductance, amperometry), together with topographical imaging, via a simple, moveable theta pipet containing electrolyte solution and an Ag/AgCl electrode in each channel. Initial studies have highlighted how functional imaging of surfaces and interfaces can be implemented and that one can also measure dynamic processes at surfaces such as ion uptake-release and electrochemistry.

There are significant prospects for SECCM methodology. First, it should be possible to pull much smaller pipets, than the 500 nm channels used herein, to permit even higher resolution imaging. Second, the method constitutes a powerful means of probing dynamics of interfaces where there is a change in the local ion concentration, for example, ion adsorption/desorption/exchange, dissolution and growth, among other possibilities. Third, our studies have highlighted how the localized amperometric mapping of heterogeneously active electrode surfaces is readily realized with SECCM. The ability to characterize local electrode activity is

of tremendous importance in electrocatalysis, electroanalysis and in understanding what triggers corrosion.[21-27] SECCM greatly extends the capabilities of pipet and scanning droplet based techniques currently used in corrosion studies.[28-29] More generally, SECCM not only provides a means for local voltammetric-amperometric analysis, but complementary information is obtained via the simultaneous conductance and topographical responses. These responses are further developed in Chapters 4 and 5.

The configuration herein is further interesting as it opens up the possibility of a gas exchange at the meniscus; thus gas/liquid/solid (electrode) reactions could be investigated. It may be possible to replace the gas phase with a variety of fluid phases, including other electrolyte solutions.

The development of a mass transport model for SECCM is also shown, permitting quantitative analysis of the response,[20] with the ability to quantify ion fluxes and electrode surface reaction rates.

3.6 References:

(1) Bard, A. J.; Fan, F. R. F.; Kwak, J.; Lev, O. *Anal. Chem.* **1989**, *61*, 132.

(2) Amemiya, S.; Bard, A. J.; Fan, F. R. F.; Mirkin, M. V.; Unwin, P. R. In *Annual Review of Analytical Chemistry*; Annual Reviews: Palo Alto, 2008; Vol. 1, p 95.

(3) Bard, A. J.; Mirkin, M. V. *Scanning Electrochemical Microscopy*; Marcel Dekker: New York, 2001.

(4) Edwards, M. A.; Martin, S.; Whitworth, A. L.; Macpherson, J. V.; Unwin, P. R. *Physiol. Meas.* **2006**, *27*, R63.

(5) Wittstock, G.; Burchardt, M.; Pust, S. E.; Shen, Y.; Zhao, C. *Angew. Chem.-Int. Edit.* **2007**, *46*, 1584.

(6) Macpherson, J. V.; Unwin, P. R. *Anal. Chem.* **2000**, *72*, 276.

(7) Macpherson, J. V.; Unwin, P. R. *Anal. Chem.* **2001**, *73*, 550.

(8) Dobson, P. S.; Weaver, J. M. R.; Holder, M. N.; Unwin, P. R.; Macpherson, J. V. *Anal. Chem.* **2005**, *77*, 424.

(9) Kranz, C.; Friedbacher, G.; Mizaikoff, B. *Anal. Chem.* **2001**, *73*, 2491.

(10) Anne, A.; Demaille, C.; Goyer, C. *Acs Nano* **2009**, *3*, 819.

(11) Anne, A.; Cambril, E.; Chovin, A.; Demaille, C.; Goyer, C. *Acs Nano* **2009**, *3*, 2927.

(12) Comstock, D. J.; Elam, J. W.; Pellin, M. J.; Hersam, M. C. *Anal. Chem.* **2010**, *82*, 1270.

(13) Takahashi, Y.; Shevchuk, A. I.; Novak, P.; Murakami, Y.; Shiku, H.; Korchev, Y. E.; Matsue, T. *J. Am. Chem. Soc.* **2010**, *132*, 10118.

(14) Williams, C. G.; Edwards, M. A.; Colley, A. L.; Macpherson, J. V.; Unwin, P. R. *Anal. Chem.* **2009**, *81*, 2486.

(15) Rodolfa, K. T.; Bruckbauer, A.; Zhou, D. J.; Korchev, Y. E.; Klenerman, D. *Angew. Chem.-Int. Edit.* **2005**, *44*, 6854.

(16) Rodolfa, K. T.; Bruckbauer, A.; Zhou, D. J.; Schevchuk, A. I.; Korchev, Y. E.; Klenerman, D. *Nano Lett.* **2006**, *6*, 252.

(17) Jones, C. E., PhD thesis, University of Warwick, 2000.

(18) Matsunaga, T.; Ishizaki, H.; Tanabe, S.; Hayashi, Y. *Archives of Oral Biology* **2009**, *54*, 420.

(19) Martin, R. D.; Beeston, M. A.; Unwin, P. R.; Laing, M. E. *Journal of the Chemical Society-Faraday Transactions* **1994**, *90*, 3109.

(20) Snowden, M. E.; Gueell, A. G.; Lai, S. C. S.; McKelvey, K.; Ebejer, N.; O'Connell, M. A.; Colburn, A. W.; Unwin, P. R. *Anal. Chem.* **2012**, *84*, 2483.

(21) Colley, A. L.; Williams, C. G.; D'Haenens Johansson, U.; Newton, M. E.; Unwin, P. R.; Wilson, N. R.; Macpherson, J. V. *Anal. Chem.* **2006**, *78*, 2539.

(22) Fernandez, J. L.; Raghuveer, V.; Manthiram, A.; Bard, A. J. *J. Am. Chem. Soc.* **2005**, *127*, 13100.

(23) Fernandez, J. L.; Walsh, D. A.; Bard, A. J. *J. Am. Chem. Soc.* **2005**, *127*, 357.

(24) Sanchez-Sanchez, C. M.; Bard, A. J. *Anal. Chem.* **2009**, *81*, 8094.

(25) Serebrennikova, I.; Lee, S.; White, H. S. *Faraday Discussions* **2002**, 199.

(26) Boxley, C. J.; White, H. S. *Journal of the Electrochemical Society* **2004**, *151*, B265.

(27) Basame, S. B.; White, H. S. *Anal. Chem.* **1999**, *71*, 3166.

(28) Staemmler, L.; Suter, T.; Bohni, H. *Journal of the Electrochemical Society* **2004**, *151*, G734.

(29) Lohrengel, M. M.; Rosenkranz, C.; Klüppel, I.; Moehring, A.; Bettermann, H.; Bossche, B. V. d.; Deconinck, J. *Electrochimica Acta* **2004**, *49*, 2863.

CHAPTER 4

Structural Correlations in Heterogeneous Electron Transfer at Monolayer and Multilayer Graphene Electrodes

As a new form of carbon, graphene is attracting intense interest as an electrode material with widespread applications. In the present study, the heterogeneous electron transfer (ET) activity of graphene is investigated using scanning electrochemical cell microscopy (SECCM), which allows electrochemical currents to be mapped at high spatial resolution across a surface for correlation with the corresponding structure and properties of the graphene surface. It is established, in this work, that the rate of heterogeneous ET at graphene increases systematically with the number of graphene layers, and that the stacking in multilayers also has a subtle influence on ET kinetics.

4.1 Introduction:

Graphene-based materials are having a huge impact in electrochemistry and electrochemical technologies, with promising applications in areas such as supercapacitors,[1] batteries,[2] electrocatalytic supports,[3] sensors for electroanalysis,[4]

and transparent electrodes.[5] These important technologies typically use graphene produced by chemical vapour deposition (CVD)[6] and other scalable methods, yet important fundamental questions concerning heterogeneous electron transfer (ET) at such materials, intrinsic to many of these applications, remain to be addressed. Electrical measurements have revealed that the electron mobility[7] and the electronic band structure[8] are sensitive to the number of graphene layers and their stacking order, with implications for electrochemistry. In this chapter, the effect of the number of graphene layers and their arrangement on the heterogeneous ET kinetics is investigated.

Graphene grown by CVD on nickel substrates[9] was optimal for the present study because it presents a heterogeneous continuous layer of microsized multilayered flakes, which can be addressed with high resolution scanning electrochemical cell microscopy (SECCM).[10-13] Thus, on one sample it is possible to make thousands of individual electrochemical (EC) measurements at different locations and relate these to the corresponding graphene structure. This provides data sets on a scale that would be unfeasible with conventional photolithographic techniques of the type employed in recent EC studies of exfoliated graphene.[14-16] In order to study the unambiguous electrochemical response of graphene without any interference from a conductive substrate, CVD graphene layers were transferred to a silicon substrate with a 300 nm thermal grown oxide layer. This substrate allowed optical visualization and identification of the morphological film features characteristic of graphene,[17-18] for direct correlation with the local electrochemistry. Importantly, the approach described herein makes possible the study of graphene surfaces with minimal intrusion and avoids the need for any postprocessing

lithographic step, which may result in unavoidable damage and possible interference of residues.[19]

4.2 EC measurements with SECCM

Ferrocene derivatives have proven particularly suitable for the study of the ET activity of sp^2 carbon allotropes, such as carbon nanotubes,[15,19-20] and so the one-electron oxidation of $FcTMA^{+/2+}$ was considered, as an exemplar outer-sphere redox couple. The dual channel theta pipet[21] (1.1 μm diameter) of the SECCM instrument was filled with an aqueous electrolyte solution containing 2 mM $FcTMA^+$ (as the hexafluorophosphate salt) and 30 mM KCl supporting electrolyte together with silver-silver chloride quasi counter reference electrodes (QCREs) to serve as both a conductance cell and voltammetric cell, with the graphene as the working electrode (Figure 4-1 a)). A linear sweep voltammogram (LSV) obtained with the SECCM setup (Figure 4-1 b)) demonstrates the electrochemical activity of graphene, with a sigmoidal wave for the oxidation of $FcTMA^+$ which rises with increasing potential to a clear transported-limited current ca. 68 pA.

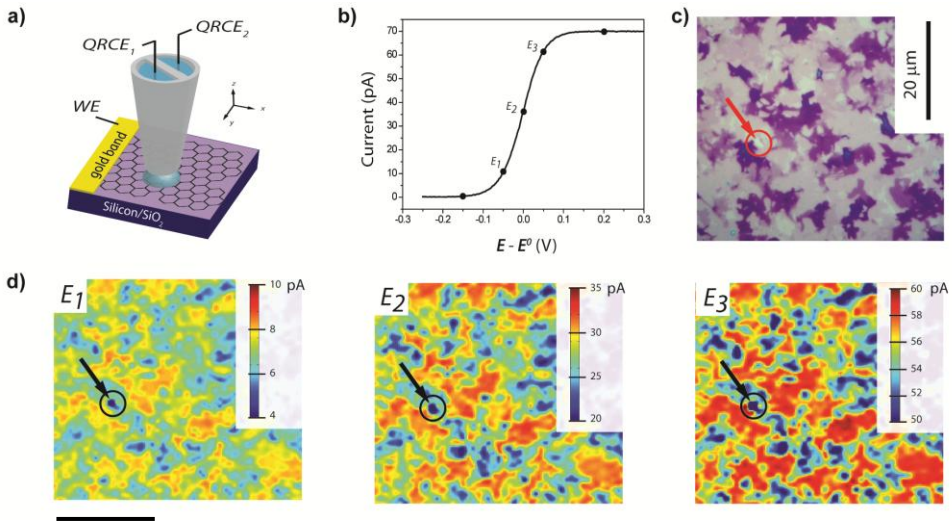

Figure 4-1: *SECCM. (a) Schematic representation of the EC imaging setup. The graphene lies on a Si/SiO_2 substrate and is connected as the working electrode via an evaporated Cr/Au band. An SECCM probe is employed as a local and mobile EC cell for electrochemical imaging. (b) LSV for the oxidation of 2 mM $FcTMA^+$ (30 mM KCl) acquired with an SECCM setup on a graphene surface, at 100 mVs^{-1}, with a 1.1 µm diameter pipet. (c) Optical microscope image of the CVD graphene area mapped by SECCM, showing the heterogeneity of the surface and the presence of multiplelayer graphene flakes. (d) Set of three EC maps of the area shown in (c) acquired by SECCM at three different substrate electrode potentials ($E-E^{o\prime}$) indicated in LSV in (b) with labels E_1, E_2 and E_3. All images are at the same scale as (c). The arrow-circle in part (c) and (d) indicates a small area where the SiO_2 was exposed and measured currents in this area are below the lower limit on the scale bar. This area was used to calibrate the number of graphene layers (vide infra). Scale bars are 20 µm.*

The waveshape is indicative of essentially reversible electron transfer (difference in the potentials at 3/4 and 1/4 of the limiting current, $E_{3/4} - E_{1/4} = 57$ mV). The wave highlights five different potentials at which the local electrochemical activity of CVD graphene was mapped by SECCM within the same area using the point by point system described in Chapter 3, with independent control of the

substrate potential and that between the two QRCEs, yielding EC current maps (presented in Figures 4-3 – 4-7 d)). These data show clearly that, at all potentials, the redox reaction occurs across the entire surface, but with significant heterogeneity in the current values. Simultaneously with the surface EC current, SECCM also acquires three complementary maps: *z* piezo displacement (related to the substrate topography, Figures 4-3 - 4-7 a)), the ion conductance current between the QCREs in the barrels (Figures 4-3 - 4-7 c)), and the AC component of the migration current (used as the set-point to control tip-to sample separation, Figures 4-3 – 4-7 b)).[10-13] Those maps (Figures 4-3 – 4-7 b)) confirm the stability of the electrolyte drop size (electrolyte contact area of the order of the pipet size,[12,21] here a 550 nm radius) and tip-to-sample separation (180 nm; determined from a finite element model which is also described in Chapter 3 and outlined further below for this particular application). Thus, the changes in surface EC current can be assigned unequivocally to differences in EC activity of the material and not to any changes in wettability. This is further evident by comparing the five EC maps (in Figures 4-3 – 4-7) which show that the most active and inactive areas are in the same location in each map. Pixel by pixel correlation between EC current maps and the corresponding optical image are also presented by taking the green component from the RGB image (Figures 4-2, 4-3 – 4-7 e)) (Digital Camera, Spot, Diagnostic Instruments, USA, attached to an Optical Microscope Olympus BH2, Olympus, Japan, with a 50x/0.7NA optical lens, Neo SPlan, Olympus, Japan). The green component (expressed on a scale of 0-255) of the optical images was used to identify the graphene thickness, since this component shows the highest contrast of graphene layers with respect to the underlying 300 nm silicon oxide layer / Si substrate.[17] In order to assign a range of contrast to graphene layer number, the green component

intensity values for bare SiO_2/Si, monolayer, bilayer and trilayer graphene were required.

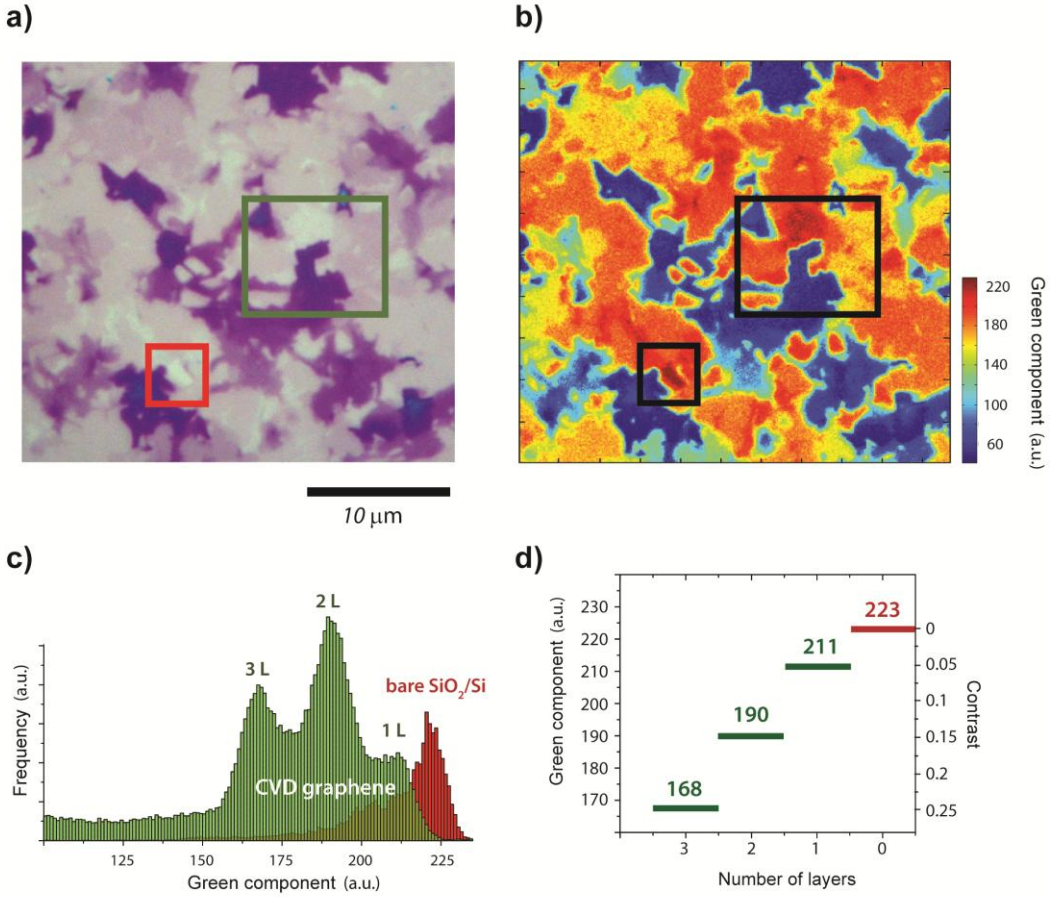

Figure 4-2: *Optical image (a) and its corresponding image using the green component of the RGB scheme (b) of the CVD graphene area studied. The red square marks an area where bare SiO_2/Si is exposed and the green square marks an area with 4 different thickness graphene flakes. (c) Histogram of the green component of each area marked with red and green squares. (d) Calibration plot of green component, light contrast and number of graphene layers.*

In the optical image presented in Figure 4-2 a) and 4-2 b) (as green component only) a red square indicates an area where bare SiO_2/Si is exposed due to a hole in the CVD graphene layer, whilst the green square limits an area where four

clearly different flakes are present: monolayer, bilayer, trilayer, and multilayer (identified by Raman spectroscopy). The green component intensity values were extracted from the histogram of each selected area (Figure 4-2 c)), and a calibration plot of contrast per number of layers (Figure 4-2 d)) obtained, with values matching previously published work of the same type of CVD graphene.[9] The calibration plot shows a linear trend of contrast *vs*. number of layers for the first three layers of graphene.[9,17,18]

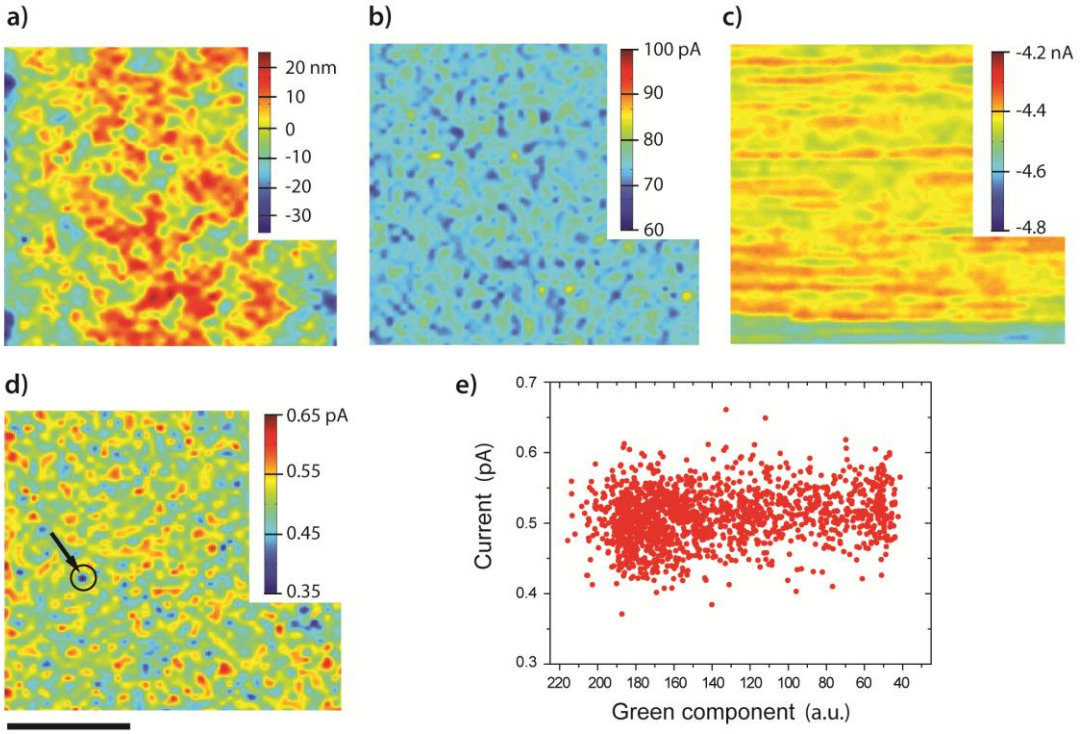

Figure 4-3: *Set of maps obtained during SECCM scanning at a potential E = -0.150 V. (a) z-piezo displacement from which topography can be observed, (b) AC component of the ion current barrels (c) conductance current between barrels, (d) electrochemical current at the working electrode, (e) pixel-by-pixel correlation between EC current map and the corresponding optical image of the scanned area, averaged and converted to green component. Scale bar is 20 µm. The points*

corresponding to Si/SiO_2 were discarded. The arrow-circle in (d) marks a small area where the silicon oxide was exposed due to a hole in the CVD graphene layer.

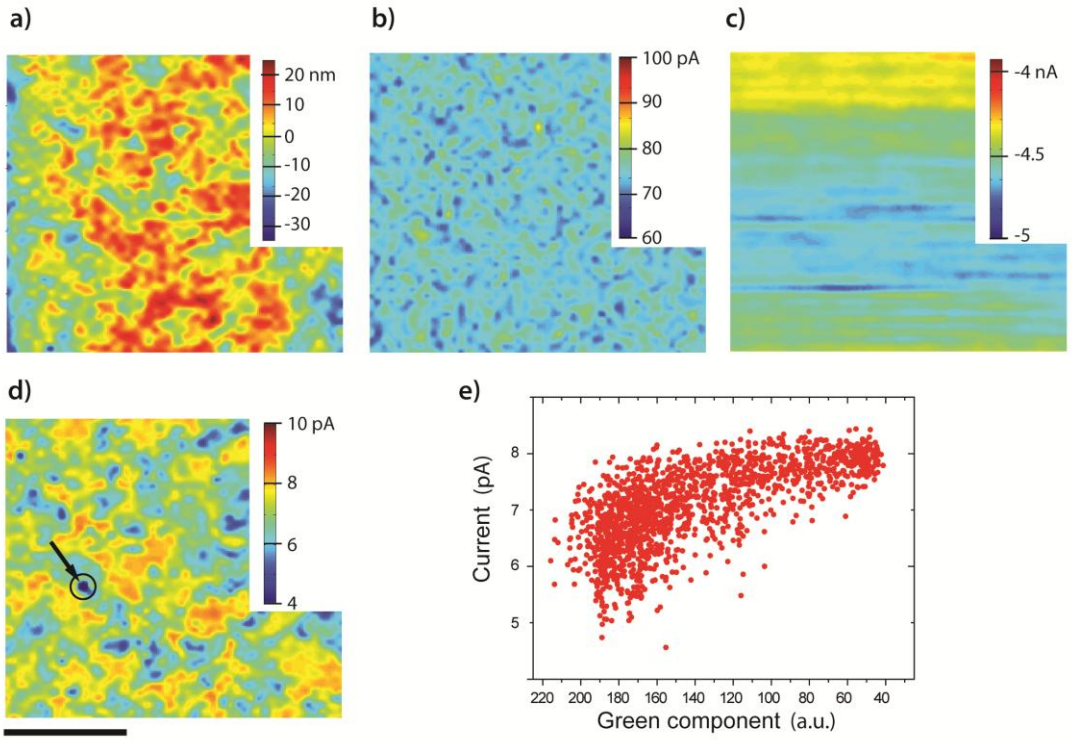

Figure 4-4: *Set of maps obtained during SECCM scanning at a potential E = -0.043 V. (a) z-piezo displacement from which topography can be observed, (b) AC component of the ion current barrels (c) conductance current between barrels, (d) electrochemical current at the working electrode, (e) pixel-by-pixel correlation between EC current map and the corresponding optical image of the scanned area, averaged and converted to green component. Scale bar is 20 µm. The points corresponding to Si/SiO_2 were discarded. The arrow-circle in (d) marks a small area where the silicon oxide was exposed due to a hole in the CVD graphene layer.*

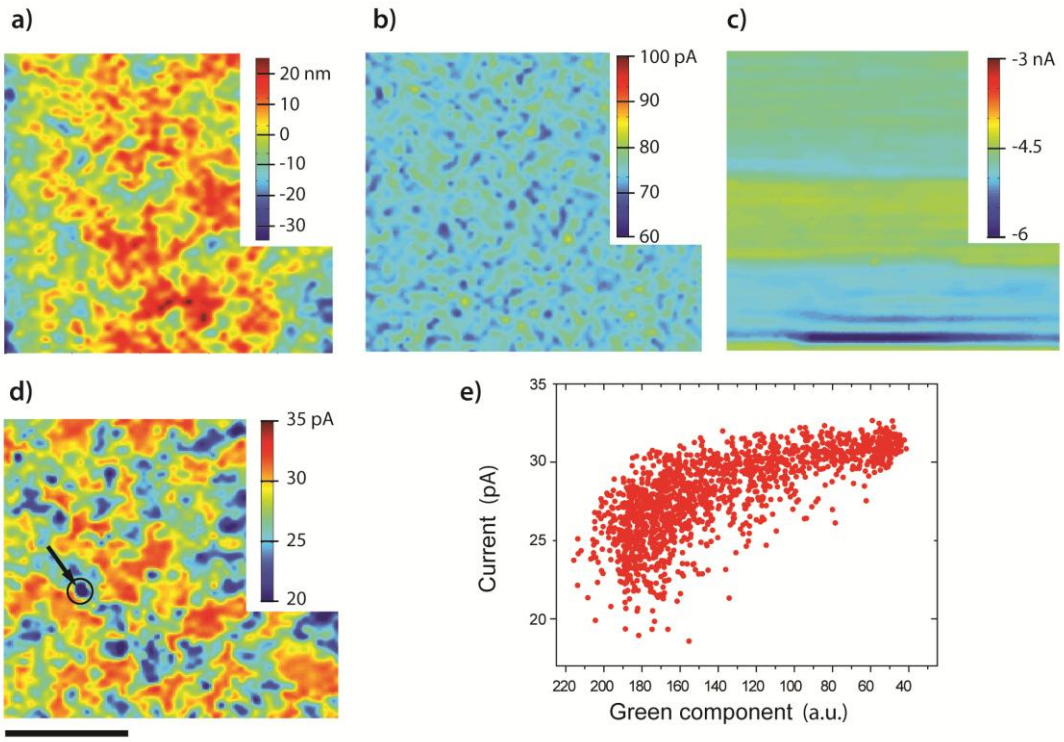

Figure 4-5: *Set of maps obtained during SECCM scanning at a potential E = 0.016 V. (a) z-piezo displacement from which topography can be observed, (b) AC component of the ion current barrels (c) conductance current between barrels, (d) electrochemical current at the working electrode, (e) pixel-by-pixel correlation between EC current map and the corresponding optical image of the scanned area, averaged and converted to green component. Scale bar is 20 µm. The points corresponding to Si/SiO_2 were discarded. The arrow-circle in (d) marks a small area where the silicon oxide was exposed due to a hole in the CVD graphene layer.*

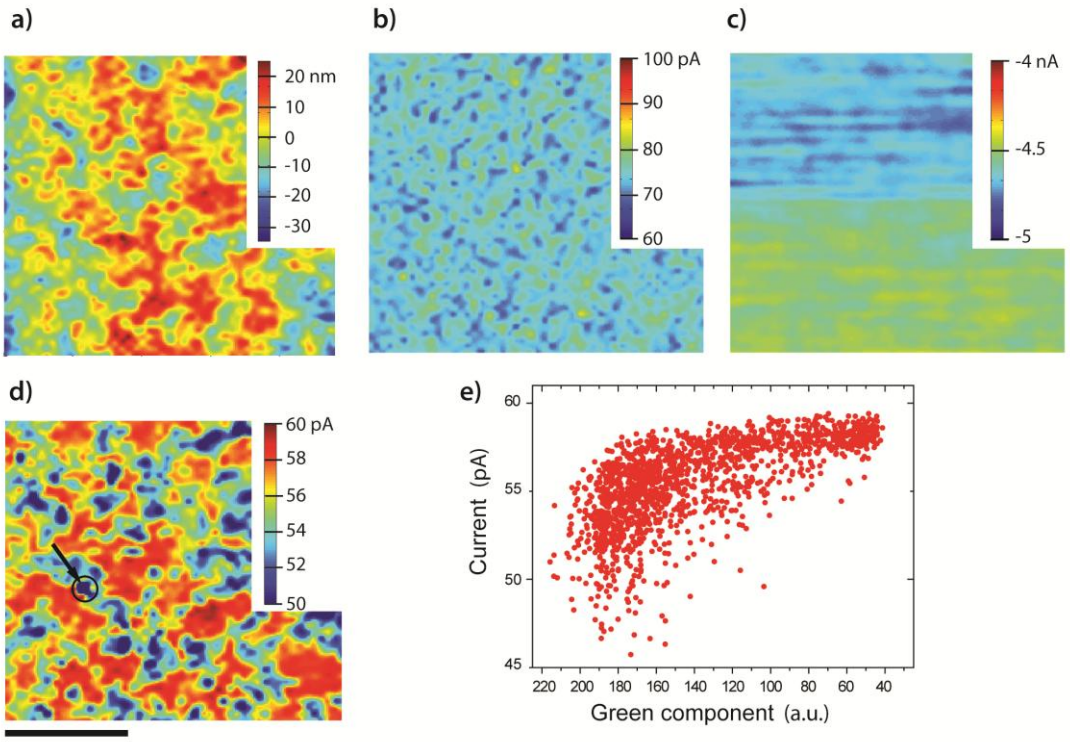

Figure 4-6: *Set of maps obtained during SECCM scanning at a potential E = 0.065 V. (a) z-piezo displacement from which topography can be observed, (b) AC component of the ion current barrels (c) conductance current between barrels, (d) electrochemical current at the working electrode, (e) pixel-by-pixel correlation between EC current map and the corresponding optical image of the scanned area, averaged and converted to green component. Scale bar is 20 µm. The points corresponding to Si/SiO_2 were discarded. The arrow-circle in (d) marks a small area where the silicon oxide was exposed due to a hole in the CVD graphene layer.*

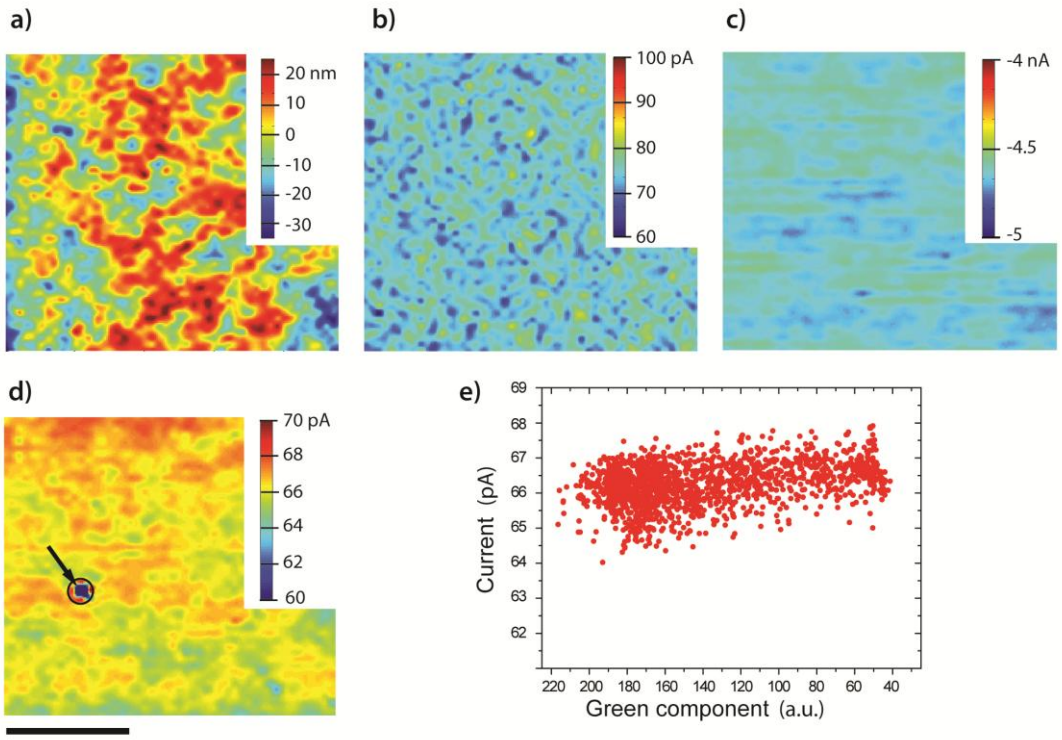

Figure 4-7: *Set of maps obtained during SECCM scanning at a potential E = 0.2 V. (a) z-piezo displacement from which topography can be observed, (b) AC component of the ion current barrels (c) conductance current between barrels, (d) electrochemical current at the working electrode, (e) pixel-by-pixel correlation between EC current map and the corresponding optical image of the scanned area, averaged and converted to green component. Scale bar is 20 µm. The points corresponding to Si/SiO_2 were discarded. The arrow-circle in (d) marks a small area where the silicon oxide was exposed due to a hole in the CVD graphene layer.*

4.3 Finite element model

A finite element model[12] was developed, by Dr. Michael Snowden, to analyze the EC maps (discussed briefly in Chapter 3), extract and assign standard heterogeneous ET rate constants at each micrometer-scale pixel of the images. The tip of the theta pipet was approximated to a circular based cone with a cylindrical meniscus as shown in Figure 4-8. The probe geometry was obtained using FE-SEM

(Figure 4-9) where the pipet radius, r_p = 550 nm, the central segment t_w = 50 nm, and the semi-angle of the capillary Θ = 8º.

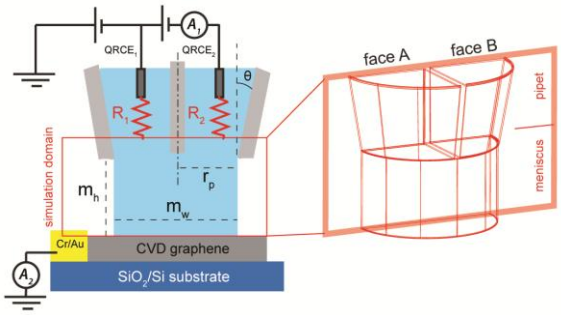

Figure 4-8: *Schematic of the SECCM probe and sample (not to scale) showing the key geometric dimensions as described previously in Chapter 3.*

Characteristic i_{dc} and i_{ac} values were used to determine the effective bias (E_f) between faces A and B needed for the ET kinetic simulations (Figure 4-8) and the tip substrate separation. For these experiments a typical setpoint of i_{ac} = 80 pA was used with i_{dc} = 4.6 nA, resulting in a predicted tip substrate separation of 180 nm shown in Figure 4-10.

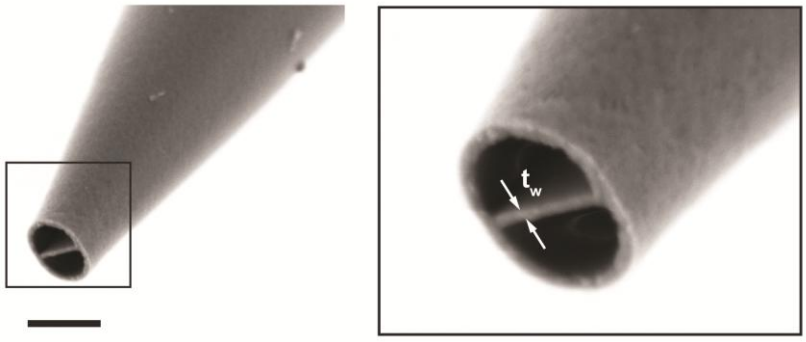

Figure 4-9: *FE-SEM images of the SECCM probes used to obtain maps of graphene. Scale bar is 1 µm and t_w = 50 nm.*

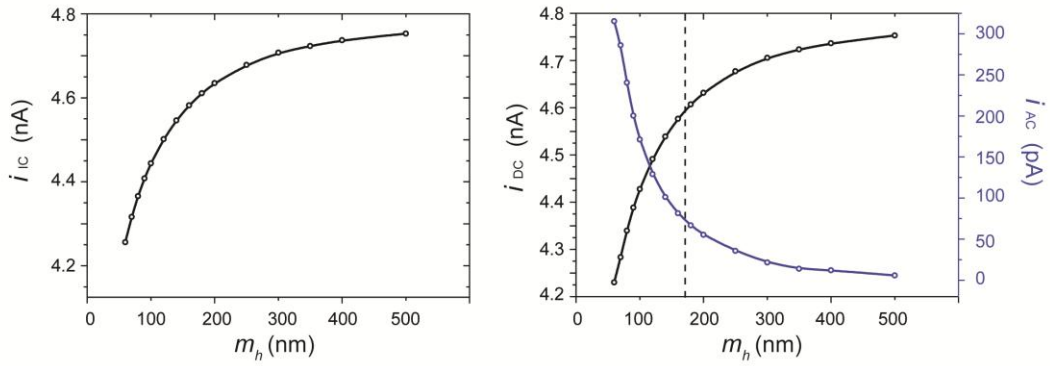

Figure 4-10: *FEM model determined approach curves for the SECCM probe, with an oscillation amplitude (peak to peak) of 100nm.*

The current due to the one-electron oxidation of $FcTMA^+$ to $FcTMA^{2+}$ (equation 1) is considered at the substrate electrode with Butler-Volmer kinetics (see Chapter 1).

$$FcTMA^+ \underset{k_f}{\overset{k_b}{\rightleftharpoons}} FcTMA^{2+} + e^- \qquad (1)$$

The rate constants of the oxidation (k_b) and reduction (k_f) of $FcTMA^{+/2+}$ are calculated using:

$$k_b = k_0 \exp\left[\frac{(1-\alpha)FE_{op}}{RT}\right] \qquad (2)$$

$$k_f = k_0\left[\frac{-\alpha FE_{op}}{RT}\right] \qquad (3)$$

where k^0 is the standard rate constant, α is the transfer coefficient chosen as α = 0.5, given the large self-exchange ET rate constant for ferrocene and its derivatives.[22] *R*

is the gas constant and T is the temperature (K), and E_{op} is the driving potential with respect to the reversible (formal potential). The flux at the substrate working electrode was defined as:

$$\mathbf{n}.\mathbf{N}_m = k_f c_p - k_b c_m \quad (4)$$

Where **n** is the unit normal vector, and $\mathbf{N}_m$ is the flux of mediator. The generation of the flux product ($\mathbf{N}_p$) at the working electrode was defined by equation (4),

$$-\mathbf{n}.\mathbf{N}_p = \mathbf{n}.\mathbf{N}_m \quad (5)$$

and the working electrode response i_{we} was calculated using equation (6).

$$i_{we} = 2nF\mathbf{n}.\mathbf{N}_m \quad (6)$$

Maps E_1, E_2 and E_3 in Figure 4-1(d), correspond to E_{op} = -0.065 V, -0.016 V, and 0.043 V, respectively. The kinetic parameter k^0 was swept between 1 x 10^{-5} to 10 cms^{-1} (Figure 4-11), to produce working curves of surface current *vs* log k^0 at each potential. These were used to convert the SECCM surface current response maps to corresponding k^0 values.

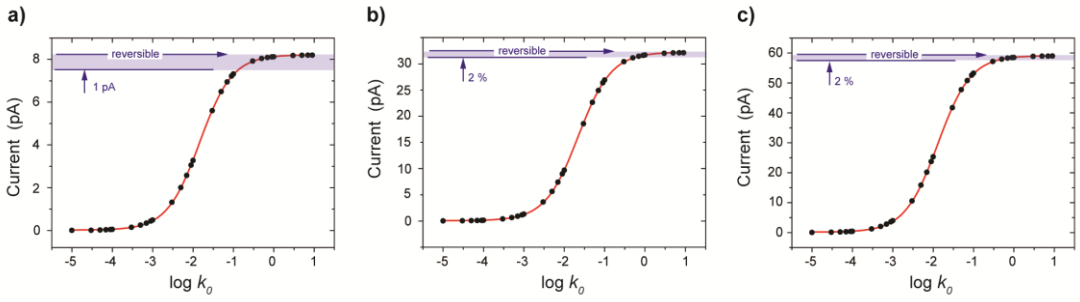

Figure 4-11: *Boltzmann fits for the simulated k^0 values obtained by FEM modelling of the SECCM probe at (a) E_{op} = -0.065 V; (b) E_{op} = -0.016 V and (c) E_{op}*

= 0.043 V. The shadowed area indicates the range of currents where the reaction is essentially reversible (within experimental error), indicated by the shaded zones in Figure 4-12.

4.4 Complementary surface analysis

Comparison between the observed heterogeneity in EC activity of CVD graphene and the corresponding topography, revealed by optical microscopy or atomic force microscopy (AFM), shows a clear correlation between electrochemical activity and the number of graphene layers. Qualitatively, there is close correspondence between dark regions (multilayers) in Figure 4-1c and high EC currents (Figures 4-1, 4-3 to 4-7 d)).

Confirmed by micro-Raman spectroscopy, the full range of light contrast was segmented into eight different bins assigned to a defined number of graphene layers. Figure 4-12 a) shows the local EC current at potential E2 versus the number of graphene layers. Similar correlations at potentials E1 and E3 are provided in Figure 4-14. From this plot, it is clear that single layer graphene exhibits the lowest EC activity and that the activity increases systematically with the number of layers, to a situation where the flakes are so active that the ET process becomes essentially reversible[13] within experimental error (see Figure 4-12).

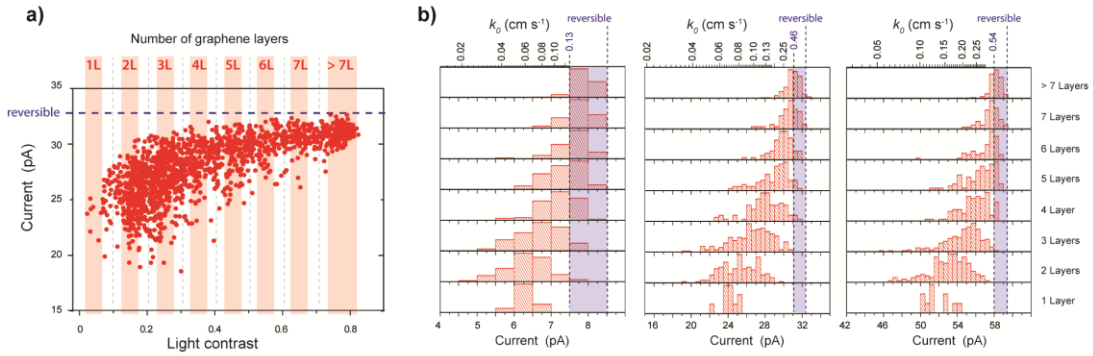

Figure 4-12: *(a) Pixel-by-pixel correlation between the EC current map at potential E2 and the number of graphene layers. (b) Histograms of the EC current and standard rate constant, k^0, for each defined number of CVD graphene layers, for potentials E1, E2, and E3 (from left to right). The dashed line in (a) and the blue area in (b) denote the conditions where the ET process becomes entirely reversible.*

EC current distributions were analyzed to obtain the corresponding ET standard rate constants (k^0) for potentials E1, E2, and E3, using the working curves shown in Figure 4-11. Figure 4-12 b) reveals that the ET kinetics evolves with the number of layers toward faster ET and a broader range of k^0 (and current magnitudes) from monolayer to multilayer graphene. This is found consistently at all three potentials. Although there will be some cross contribution of different flakes at some single point measurements (where the tip is at the boundary between flakes), the different stacking order within the graphene multilayers could also play a role in the broadness of ET kinetics, seen for bilayer, trilayer, and thicker flakes, especially for epitaxy of CVD multilayer graphene, where non-Bernal or AB stacking order is very common.[23]

Raman spectroscopy was employed (HeNe 633nm laser microRaman, Renishaw inVia, UK, using a 100x optical lens. Leica NA 0.8, and a 10% attenuation

was used to achieve a *ca*. 500 nm diameter spot dimensions, with < 2mW power) to determine both the stacking order and the corresponding number of layers on different graphene flakes for correlation with EC (Figure 4-13). Figure 4-13 a shows a zoom of the optical image and the associated SECCM map. Four different graphene flakes labeled A1, A2, A3, and A4, can be differentiated and categorized as monolayer, bilayer, trilayer, and multilayer graphene, respectively (vide infra). The Raman spectra of those areas (Figure 4-13 c)) present the three characteristic graphene D, G, and 2D peaks.[24] For the A1 and A2 areas, the 2D bands are slightly more intense than the G peak, and the FWHM values of the 2D peaks are around 35−40 cm^{-1}, hallmarks of single layer CVD graphene.[9,25] However, the upshift of about 10 cm^{-1} for the 2D peak[26,27] (Figure 4-13 d)), in addition to light contrast values of 0.15 (*vide supra*), indicate that the A2 region actually corresponds to a non-AB stacking bilayer. The lack of AB stacking (Figure 4-13 d)) reduces electronic coupling between the graphene layers, so that bilayer graphene in this configuration has electronic properties similar to those of monolayer graphene.[28-30] This evidently directly impacts the EC activity: current values for the A2 spot are very similar to those of the A1 region (Figure 4-12 and 4-13), which corresponds to a single layer. It is accepted that the electronic structure and density of states play a key role in heterogeneous ET rates,[31,32] and these results show that different graphene layers (monolayer and bilayer), with closely similar band structures, behave analogously in terms of electrochemistry. This result also allows us to rule out a strong influence of charge carrier mobility to the EC activity measured. An increase of mobility is expected for a non-AB stacking bilayer, compared to monolayer graphene, since the substrate effect is, to some extent, screened by the additional graphene layer beneath the top layer in the case of bilayer graphene,[33] but

this does not enhance ET kinetics compared to the intrinsic activity of monolayer graphene.

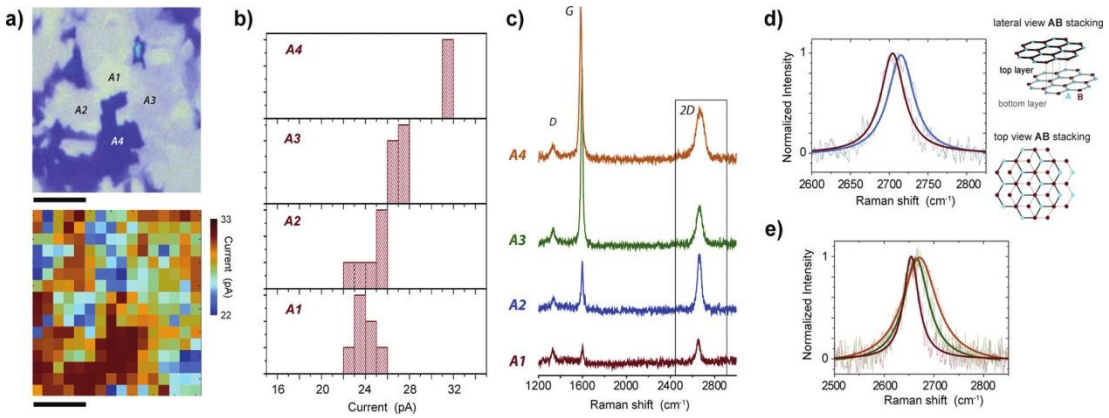

Figure 4-13: *(a) Optical image of CVD graphene with four different flakes labeled A1, A2, A3, and A4, and corresponding SECCM data. Scale bar is 5 μm. (b) Histograms of the EC current in each designated flake at potential E2. (c) Raman spectra acquired with an excitation wavelength of 633 nm and spot size of 500 nm at each graphene flake. The three characteristic Raman peaks for graphene are labeled as D, G, and 2D. (d) Raman 2D peak for regions A1 (red line) and A2 (blue line) plotted together highlighting the ~10 cm^{-1} Raman upshift characteristic for a non-AB stacking bilayer (blue line). Schematic of Bernal (AB-stacking) for a bilayer of graphene. The basic structure of graphene is defined with two atoms in the unit cell, denoted A (red dot) and B (blue dot). For an AB stacking bilayer, the A atom of the top layer lies directly over the B atom of the bottom layer. (e)The Raman 2D peak for areas A1 (red line), A3 (green line), and A4 (orange line).*

The areas A3 and A4 are assigned to trilayer and multilayer (>trilayer), respectively, based on the much broader 2D peak (Figure 4-13 e)) and the intensity and peak position of the G peak (Figure 4-13 c)). For these domains, an increase of EC activity, at all the measured potentials, is observed with the number of layers (Figure 4-12 and 4-13), consistent with the evolution of the density of electronic

states through single layer, AB-bilayer, and trilayer graphene.[7] These more detailed analyses confirm the trend (*vide supra*) between EC current and light contrast in the optical image (interpreted as the number of graphene layers).

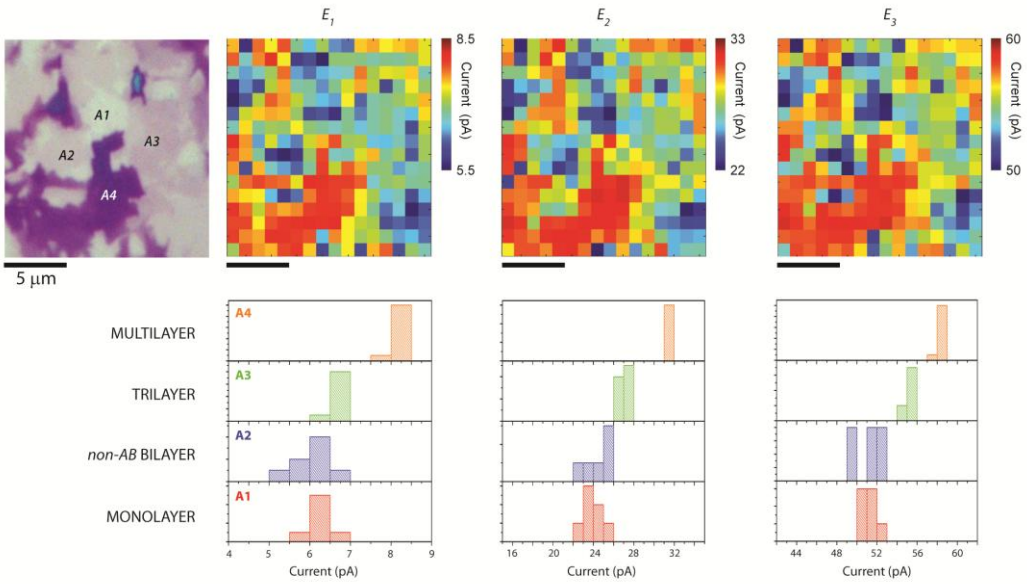

Figure 4-14: *Zoom of the optical microscope image and the associated SECCM maps at all potentials (E1, E2, E3) of the area examined with Raman spectroscopy. Four different areas are labelled as A1, A2, A3, and A4, and their histograms of EC current are shown.*

Complementary experiments were carried out to eliminate other possible causes for the observed changes in EC activity with the number of graphene layers. An exhaustive analysis of surface roughness was performed over the sample with AFM to discard the possibility that the observed increase of EC activity was due to a change in the roughness of the surface with the number of layers. The presence of wrinkles is unavoidable for synthetic graphene, which are responsible for local changes in the electronic structure,[34] but they were essentially uniform (as evidenced

by AFM in Figure 4-15) over the entire surface area and independent of the number of layers and flakes.

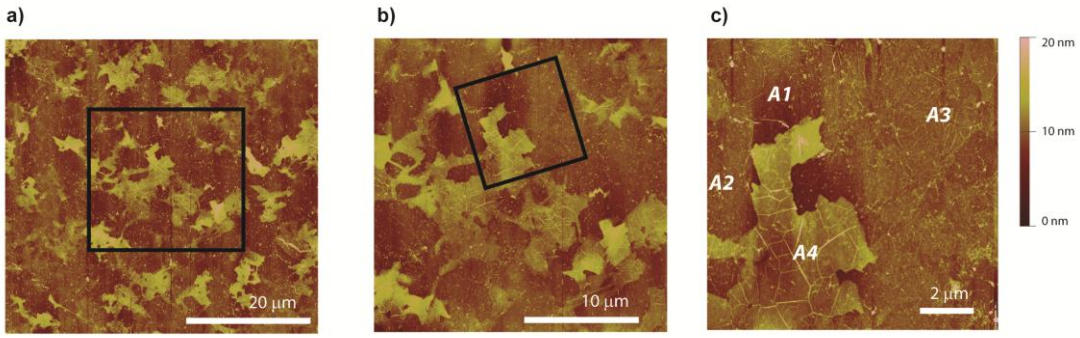

Figure 4-15: *AFM images of the CVD graphene studied by SECCM. The black squares denote the zoomed in area.*

The Raman D peak at 1350 cm^{-1} is usually used to determine the density of defects on graphene,[24,25] either as the peak intensity itself or with the ratio of D and G peaks (ID/IG). In all spectra obtained, the D peak intensity was essentially constant for all flakes studied and independent of the number of layers. Indeed, if the ID/IG ratios are compared, the multilayered flakes have the lowest density of defects, yet have higher activity. It is further well-known[35,36] that edges accumulate a higher density of defects, but it is clear that no increase of EC activity either along the edges of the flakes or at the (step-edge) boundary between flakes is seen, at the spatial resolution of the investigation.

4.5 Conclusions

In conclusion, it has been demonstrated how the ET activity of a complex graphene material can be elucidated, analyzed, and correlated with intrinsic structural properties using high resolution SECCM in tandem with Raman microscopy, optical microscopy, and AFM. The unprecedented insights on the structural controls of ET are of fundamental value and provide a rational basis for the design and use of graphene in electrochemical technologies. The SECCM methodology described is general, and it is expected it to find increasing use for structure−function imaging of surface and interfacial processes.

4.6 References

(1) Zhu, Y.; Murali, S.; Stoller, M. D.; Ganesh, K. J.; Cai, W.; Ferreira, P. J.; Pirkle, A.; Wallace, R. M.; Cychosz, K. A.; Thommes, M.; Su, D.; Stach, E. A.; Ruoff, R. S. *Science* **2011**, *332*, 1537.

(2) Xiao, J.; Mei, D.; Li, X.; Xu, W.; Wang, D.; Graff, G. L.; Bennett, W. D.; Nie, Z.; Saraf, L. V.; Aksay, I. A.; Liu, J.; Zhang, J.-G. *Nano Letters* **2011**, *11*, 5071.

(3) Liang, Y.; Li, Y.; Wang, H.; Zhou, J.; Wang, J.; Regier, T.; Dai, H. *Nature Materials* **2011**, *10*, 780.

(4) Schedin, F.; Geim, A. K.; Morozov, S. V.; Hill, E. W.; Blake, P.; Katsnelson, M. I.; Novoselov, K. S. *Nature Materials* **2007**, *6*, 652.

(5) Bonaccorso, F.; Sun, Z.; Hasan, T.; Ferrari, A. C. *Nature Photonics* **2010**, *4*, 611.

(6) Bae, S.; Kim, H.; Lee, Y.; Xu, X.; Park, J.-S.; Zheng, Y.; Balakrishnan, J.; Lei, T.; Kim, H. R.; Song, Y. I.; Kim, Y.-J.; Kim, K. S.; Ozyilmaz, B.; Ahn, J.-H.; Hong, B. H.; Iijima, S. *Nature Nanotechnology* **2010**, *5*, 574.

(7) Zhu, W.; Perebeinos, V.; Freitag, M.; Avouris, P. *Physical Review B* **2009**, *80*.

(8) Bao, W.; Jing, L.; Velasco, J., Jr.; Lee, Y.; Liu, G.; Tran, D.; Standley, B.; Aykol, M.; Cronin, S. B.; Smirnov, D.; Koshino, M.; McCann, E.; Bockrath, M.; Lau, C. N. *Nature Physics* **2011**, *7*, 948.

(9) Reina, A.; Jia, X.; Ho, J.; Nezich, D.; Son, H.; Bulovic, V.; Dresselhaus, M. S.; Kong, J. *Nano Letters* **2009**, *9*, 30.

(10) Ebejer, N.; Schnippering, M.; Colburn, A. W.; Edwards, M. A.; Unwin, P. R. *Analytical Chemistry* **2010**, *82*, 9141.

(11) Lai, S. C. S.; Dudin, P. V.; Macpherson, J. V.; Unwin, P. R. *Journal of the American Chemical Society* **2011**, *133*, 10744.

(12) Snowden, M. E.; Guell, A. G.; Lai, S. C. S.; McKelvey, K.; Ebejer, N.; O'Connell, M. A.; Colburn, A. W.; Unwin, P. R. *Anal. Chem.* **2012**.

(13) Lai, S. C. S.; Patel, A. N.; McKelvey, K.; Unwin, P. R. *Angewandte Chemie (International ed. in English)* **2012**, *51*, 5405.

(14) Xia, J.; Chen, F.; Li, J.; Tao, N. *Nature Nanotechnology* **2009**, *4*, 505.

(15) Li, W.; Tan, C.; Lowe, M. A.; Abruna, H. D.; Ralph, D. C. *Acs Nano* **2011**, *5*, 2264.

(16) Valota, A. T.; Kinloch, I. A.; Novoselov, K. S.; Casiraghi, C.; Eckmann, A.; Hill, E. W.; Dryfe, R. A. W. *Acs Nano* **2011**, *5*, 8809.

(17) Blake, P.; Hill, E. W.; Neto, A. H. C.; Novoselov, K. S.; Jiang, D.; Yang, R.; Booth, T. J.; Geim, A. K. *Applied Physics Letters* **2007**, *91*.

(18) Ni, Z. H.; Wang, H. M.; Kasim, J.; Fan, H. M.; Yu, T.; Wu, Y. H.; Feng, Y. P.; Shen, Z. X. *Nano Letters* **2007**, *7*, 2758.

(19) Dudin, P. V.; Snowden, M. E.; Macpherson, J. V.; Unwin, P. R. *Acs Nano* **2011**, *5*, 10017.

(20) Heller, I.; Kong, J.; Heering, H. A.; Williams, K. A.; Lemay, S. G.; Dekker, C. *Nano Letters* **2005**, *5*, 137.

(21) Rodolfa, K. T.; Bruckbauer, A.; Zhou, D. J.; Korchev, Y. E.; Klenerman, D. *Angewandte Chemie-International Edition* **2005**, *44*, 6854.

(22) Nielson, R. M.; McManis, G. E.; Weaver, M. J. *Journal of Physical Chemistry* **1989**, *93*, 4703.

(23) Pimenta, M. A.; Dresselhaus, G.; Dresselhaus, M. S.; Cancado, L. G.; Jorio, A.; Saito, R. *Physical Chemistry Chemical Physics* **2007**, *9*, 1276.

(24) Ferrari, A. C.; Meyer, J. C.; Scardaci, V.; Casiraghi, C.; Lazzeri, M.; Mauri, F.; Piscanec, S.; Jiang, D.; Novoselov, K. S.; Roth, S.; Geim, A. K. *Physical Review Letters* **2006**, *97*.

(25) Malard, L. M.; Pimenta, M. A.; Dresselhaus, G.; Dresselhaus, M. S. *Physics Reports-Review Section of Physics Letters* **2009**, *473*, 51.

(26) Poncharal, P.; Ayari, A.; Michel, T.; Sauvajol, J. L. *Physical Review B* **2008**, *78*.

(27) Ni, Z. H.; Chen, W.; Fan, X. F.; Kuo, J. L.; Yu, T.; Wee, A. T. S.; Shen, Z. X. *Physical Review B* **2008**, *77*.

(28) Lopes Dos Santos, J. M. B.; Peres, N. M. R.; Castro Neto, A. H. *Physical Review Letters* **2007**, *99*, 256802.

(29) Latil, S.; Meunier, V.; Henrard, L. *Physical Review B* **2007**, *76*.

(30) Hass, J.; Varchon, F.; Millan-Otoya, J. E.; Sprinkle, M.; Sharma, N.; De Heer, W. A.; Berger, C.; First, P. N.; Magaud, L.; Conrad, E. H. *Physical Review Letters* **2008**, *100*.

(31) Bard, A. J.; Faulkner, L. R. *Electrochemical methods fundamentals and applications*; Wiley: Weinheim, 2001.

(32) Heller, I.; Kong, J.; Williams, K. A.; Dekker, C.; Lemay, S. G. *Journal of the American Chemical Society* **2006**, *128*, 7353.

(33) Ohta, T.; Bostwick, A.; McChesney, J. L.; Seyller, T.; Horn, K.; Rotenberg, E. *Physical Review Letters* **2007**, *98*.

(34) Xu, K.; Cao, P.; Heath, J. R. *Nano Letters* **2009**, *9*, 4446.

(35) Graf, D.; Molitor, F.; Ensslin, K.; Stampfer, C.; Jungen, A.; Hierold, C.; Wirtz, L. *Nano Letters* **2007**, *7*, 238.

(36) Yu, Q.; Jauregui, L. A.; Wu, W.; Colby, R.; Tian, J.; Su, Z.; Cao, H.; Liu, Z.; Pandey, D.; Wei, D.; Chung, T. F.; Peng, P.; Guisinger, N. P.; Stach, E. A.; Bao, J.; Pei, S.-S.; Chen, Y. P. *Nature Materials* **2011**, *10*, 443.

Chapter 5

High Resolution electrochemical interrogation of complex Single Walled Carbon Nanotube (SWNT) structures

This chapter investigates the intrinsic electrochemical properties of single walled carbon nanotubes (SWNTs). SECCM is applied to two different configurations which have found to have widespread applications in electrochemistry, but for which the underpinning intrinsic response is unknown. In the first instance, a 3 dimensional SWNT forest arrangement is studied. It had been previously proposed that the sidewalls of SWNTs are electrochemically inactive, or are active only at gross defect sites, and furthermore, that only open carbon nanotube ends allow electron transfer. In the arrangement studied herein, it has been possible to test this model directly and unambiguously. In the second part of this chapter high resolution imaging is used to investigate the nature of electron transfer in 2-dimensional arrays of SWNTs. In this system it has been possible to investigate individual SWNTs having a large number of sidewalls, crossing points of SWNTs and ends at high spatial resolution and determine their contribution to the electrochemical response.

5.1 Introduction

Within the family of nanostructured materials, carbon nanotubes (CNTs) have attracted particular attention because they are readily synthesised at low cost, have exceptional electronic properties, exhibit chemical and mechanical stability, and are amenable to a wide range of simple chemical functionalization routes.[1-3] These characteristics have led to CNTs being considered ideal substrates for electronics,[4] sensing systems,[5-6] electrocatalytic supports,[7] and batteries.[8] Furthermore, the different configurations in which CNTs can be arranged broaden their versatility and allow custom design of devices for specific applications. Individual single-walled carbon nanotubes (SWNTs),[9] 2D networks,[10-12] and 3D nanostructures[13] have all been employed successfully.

Understanding heterogeneous electron transfer (HET) at CNTs is of considerable importance, due to the wide range of electroanalytical and electrocatalytic systems based on CNTs,[14-17] and also because electrochemistry provides an attractive route to functionalize and tailor the properties of CNTs.[18-20] Probing HET in 1D electrode materials is interesting fundamentally, given their inherent electronic structure and properties.[21-22] However, as highlighted herein, despite many studies aimed at characterizing HET at CNTs, substantial questions remain unanswered, such as the location and rate of HET.

A popular approach for studying electrochemistry at CNTs involves drop-casting the material onto an electroactive support,[23-24] but this makes it difficult to unambiguously identify the contribution from CNTs alone. These voltammetric studies have led to an interpretation that CNTs are active only at edge-plane like defects in multiwalled nanotubes (MWNTs) and at the open oxygenated ends of MWNTs and SWNTs,[23-25] with the sidewall inactive, even for simple redox couples.

A separate approach has been to study CNTs on an inert substrate to ensure that the electrochemical (EC) signal measured can be uniquely attributed to the CNT material used. Both 2D networks of SWNTs[12,26-28] and individual SWNT devices[29-30] have been employed, and facile HET has been reported for several redox complexes at a majority of SWNTs assessed.

In order to more fully assess and understand the electrochemical behavior of SWNTs, it is necessary to measure HET of different components, e.g., sidewalls and ends, at very high spatial resolution, allowing the spread of activity to be identified. The use of scanning electrochemical cell microscopy (SECCM),[31-32] enables such analysis to be performed, utilizing a theta pipet probe filled with an electrolyte solution and a QRCE in each channel, for the EC interrogation of a substrate. The meniscus created at the end of the probe defines a local and mobile EC cell, confining the measurement of the substrate to the dimensions of the pulled pipet.[33] The technique is used in two configurations, making single spot voltammetric measurements and high resolution electrochemical imaging. In the latter case, using feedback protocols, the tip maintains a constant distance from the sample to produce EC maps, specifically of redox reactions at the SWNT network biased at a defined potential with respect to the QRCEs. This allows EC data to be collected across a range of characteristic SWNT sites while accessing only a very small part of the electrode material at a time.

The focus herein, were 3D forests and 2D networks of SWNTs grown by chemical vapor deposition (CVD). In addition to the pristine and low-defect nature of such SWNTs,[26,34] both arrangements expose a large quantity of characteristic sidewalls and ends for investigation, without the need for any post-processing. The forest is particularly interesting with wide ranging applications.[35-37] In the

electrochemical arena, forests have been proposed for sensing and energy applications,[38] with the vast majority of studies focusing on forests with open ends. Two-dimensional networks of SWNTs are also of interest for at least two further reasons: (i) There is now ample evidence that such an electrode arrangement is optimal for maximizing signal to noise in voltammetric and amperometric measurements,[26,39] and so understanding the intrinsic activity is valuable; and (ii) this arrangement presents a rather challenging array of closely spaced active elements for electrochemical imaging and highlights the capabilities of SECCM in resolving such complexity. More generally, the configuration of SECCM is shown on a number of challenging samples with the ability to perform localised electrochemical measurements. In the case of a 2D network of SWNTs on an inert substrate, the methodology, leads to ultrahigh mass-transport rates that allow incredibly high HET rate constants to be quantitatively determined, while also permitting distinction between different models of EC activity.

5.2 Results and discussion

5.2.1 3D forests

SWNT forest were investigated electrodes using a new nanoscale electrochemical cell technique,[31,40] which allows us to examine electrochemistry at characteristic sites, closed ends and sidewalls, in isolation. In essence, a nanopipet containing electrolyte solution and one or more reference/counter electrode(s) is used to make an electrochemical cell with a targeted region of a sample, which is connected as a working electrode. For the present application, this is particularly powerful, as any type of post processing, lithography[29] or mechanical cutting of the SWNTs is avoided,[41] allowing the study of the true electrochemical activity of the

forests in the native, pristine, unprocessed state. For the studies described herein, SWNT forests, were grown using chemical vapour deposition (CVD). CVD was chosen for forest growth, in preference to chemical processing and vertical alignment via chemical binding to a substrate, as CVD enables high density, pristine, closed-end SWNTs to be grown directly. Chemical processing, results in cutting and shortening of the SWNTs and incomplete coverage of the underlying conducting substrate.[25,42] Figure 5-1 shows a representative field emission-scanning electron microscopy (FE-SEM) image of a CVD as-grown SWNT forest (a) and a typical TEM image (b) of a SWNT extracted from the forest. CVD growth and characterisation details can be found in chapter 2.

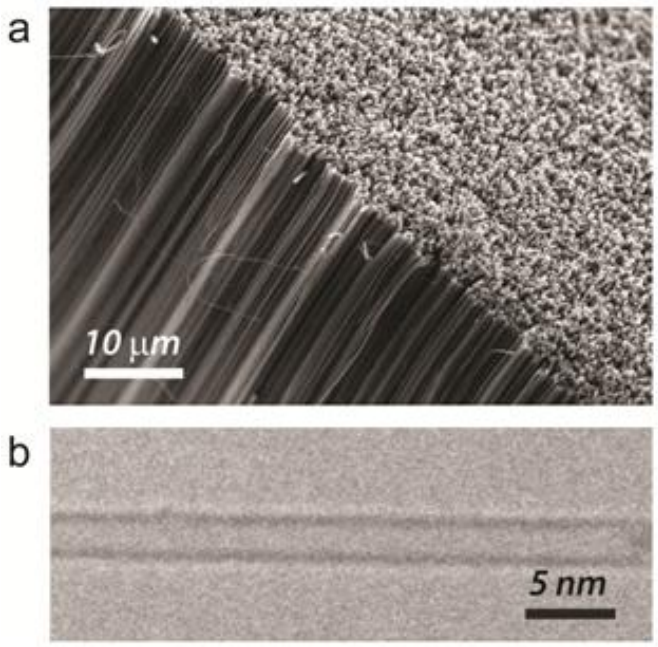

Figure 5-1: *(a) FE-SEM image of a SWNT forest. (b) typical TEM image of a SWNT extracted from a forest.*

The high quality of the forests was further proven using micro-Raman spectroscopy on intact forests, recorded from both the SWNT ends and the sidewalls. The shape and location of the G band (sp^2 carbon) at 1589 cm^{-1}, in both spectra in

Figure 5-2, is indicative of SWNTs.[43-44] Whilst small D peaks (sp^3 carbon) are visible, G / D ratios for the ends and the sidewalls, 7:1 and 9:1 respectively, indicate significantly higher quality forests (*i.e.* cleaner, lower defect density) than those previously described in literature.[41,44]

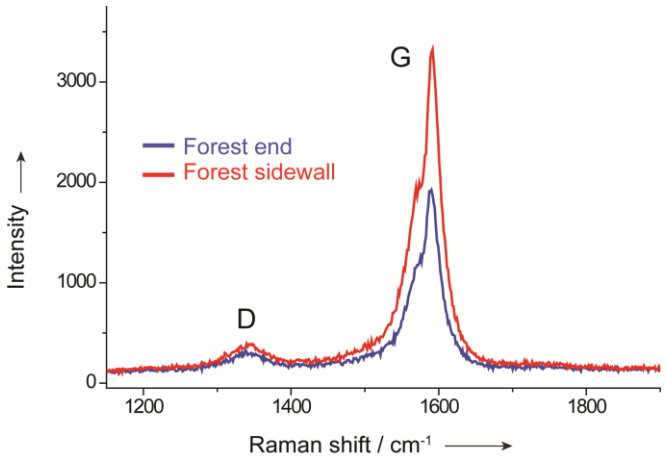

Figure 5-2: *Micro-Raman spectra of an intact SWNT forest focusing on the sidewalls and tube ends.*

It was also particularly important to confirm that the ends of the forests were free from catalytic metal nanoparticles (NPs), since these can impact significantly on the electrochemical response of SWNTs.[45-48] The results of X-ray photoelectron spectroscopy (XPS) are shown in Figure 5-3 a), for the top surface of the forest (black line), and the surface of the cobalt (Co) catalyst (red line) after subjecting it to 'growth' conditions but without a carbon source (i.e. no actual growth). The catalyst sample shows a distinct cobalt 2p peak at 780 eV. Peaks at 75 eV and 530 eV are for aluminium (Al 2p) and oxygen (O 1s), respectively, from the aluminium oxide under-layer. In contrast, for the forest, the Co peak disappears and the spectrum is dominated by a carbon 1s peak at 290 eV.

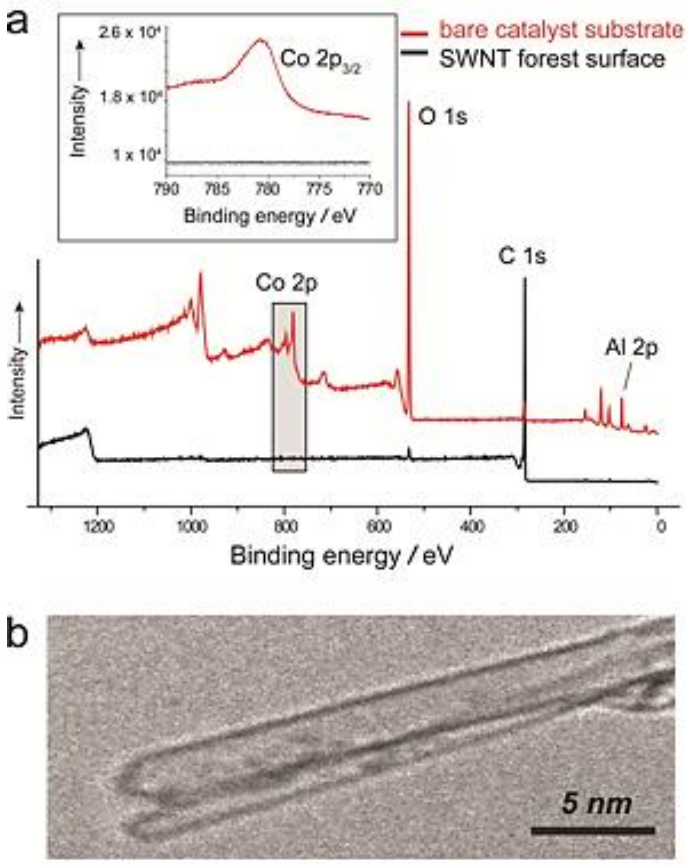

Figure 5-3: *(a) XPS spectra of bare catalyst substrate (red line) and SWNT forest surface (black line). The inset shows the spectral range corresponding to Co* $2p_{3/2}$ *for both SWNT forest (black line) and catalyst (red line) surfaces. (b) Typical TEM image of SWNT ends.*

Since the penetration depth of XPS is ca. 10 nm and the forest was ~ 500 mm thick, this analysis proves that these SWNT forests exhibit a root growth process,[49] where the catalytic NPs reside at the base of the SWNT, i.e. on the substrate. There is a very small oxygen 1s peak, relative to C 1s, originating from the top 10 nm of the SWNT forest. This most likely results from a small degree of oxygenation of the SWNT forest under ambient conditions, but is insignificant compared to the signals obtained when a SWNT end is deliberately opened.[25,41] Further TEM images of

SWNT ends, e.g. Figure 5-3 b), confirmed that they were closed and free from catalyst NPs, the latter in agreement with the XPS data.

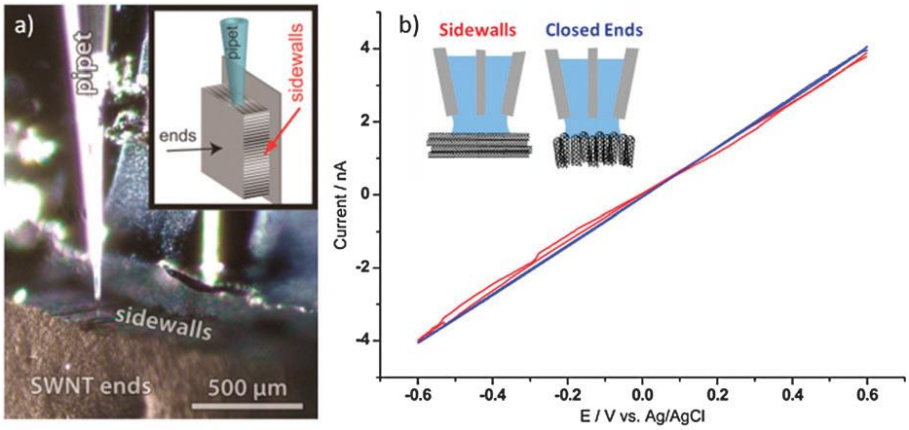

Figure 5-4: *a) Digital photograph and schematic of the pipet in contact with the forest sidewalls, for voltammetric and conductance analysis. b) Current-voltage curves (forward and reverse) recorded on the closed ends (blue) and sidewalls (red), with a pipet of inner diameter 400 nm, containing 50 mM KCl at 100 mV* s^{-1}.

To produce an electrical contact to the SWNT forest, a 200 nm thick gold film was evaporated onto half of the sample, covering both the tops and sides, by means of a shadow mask, leaving the rest of the sample intact for electrochemical analysis. The sample was then mounted to align either the top of the forest or the sidewalls, for electrochemical interrogation. The theta glass (double barrelled) pipet tips, of typical inner diameter ~ 400 nm (accurately characterised using FE-SEM) were filled with the solution of interest, and Ag–AgCl quasi-reference counter electrodes (QRCEs) were placed in each barrel. With a bias applied between the two barrels the conductance current, which flows between barrels, via the meniscus at the end of the pipet tip, could be monitored. This enabled: (i) accurate positioning of the tip, keeping the tip and meniscus in a fixed position during voltammetric

measurements;[31,40] and (ii) assess the contact area of the meniscus with the area of interest on the SWNT forest. Figure 5-4 b) shows typical conductance current–voltage curves, recorded by sweeping the potential of one QCRE with respect to the other (held at ground), with 50 mM potassium chloride solution in the pipet. The pipet was maintained in a fixed position on the SWNT forest over the closed ends (blue line) and sidewalls (red line). A similar response is seen in both locations, which is close to that recorded for similar sized theta pipet tips on hydrophobic impermeable substrates.[33] This was an indication that the SNWT forest is not permeated to any significant extent by electrolyte from the pipet tip.

For redox measurements, the pipet was filled with solution containing both supporting electrolyte and the redox species of interest. Once contact had been made between the pipet meniscus and forest, cyclic voltammetric (CV) measurements were carried out at different spots on several samples, at both the forest ends and the sidewalls, with the SWNT forest connected as the working electrode. Two well-known outer sphere, redox couples, with very different formal potentials ($E^{0'}$ values), $FcTMA^{+/2+}$[29] and hexaammineruthenium ($Ru(NH_3)_6^{3+/2+}$), were used to probe the local electrochemical response. Figures 5-5 and 5-6 show typical CVs recorded at the SWNT ends and sidewalls. These data clearly show that, for both couples, the electrochemical response is comparable with a difference in the $^1/_4$-wave and $^3/_4$-wave potential, $E_{1/4}–E_{3/4}$, in the range 57–64 mV, indicating that the reactions are close to reversible in all locations.

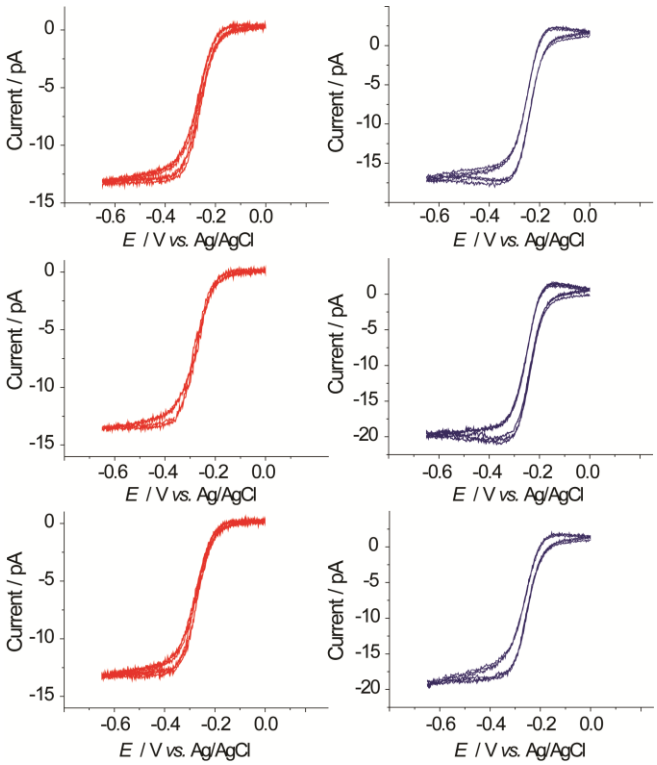

Figure 5-5: *Typical CVs of 5 mM* $Ru(NH_3)_6^{3+}$ *reduction in 50 mM KCl at a scan rate of 100 mV* s^{-1}*. Red lines indicate forest sidewalls, blue lines, forest closed ends. Measurements were performed at different spots on the surface.*

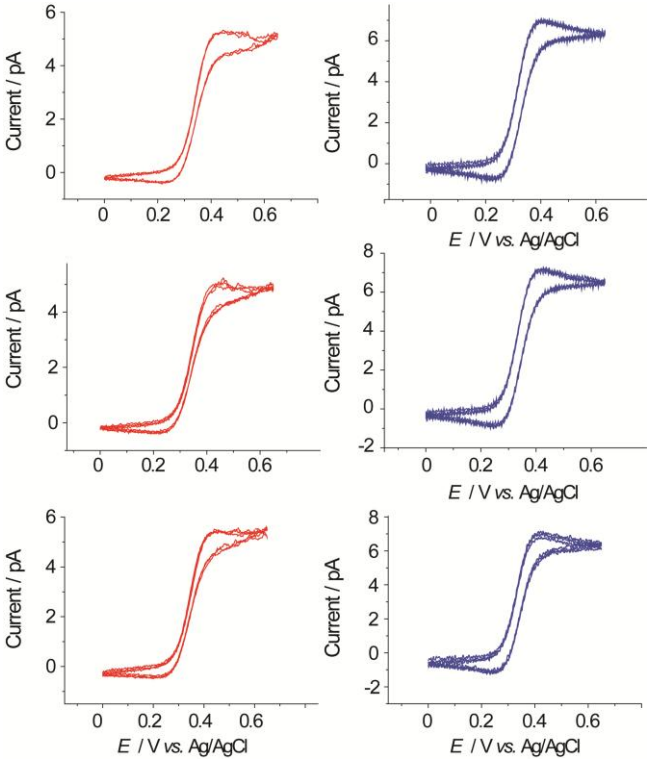

Figure 5-6: *CVs of 2 mM $FcTMA^{+/2+}$ oxidation in 50 mM KCl at a scan rate of 100 mV s^{-1}. Red lines indicate forest sidewalls, blue lines, the forest closed ends. Measurements were performed at different spots on the surface.*

The mass transfer rate coefficient (k_t) for this pipet electrode arrangement is estimated as ~ 0.03 cm s^{-1}, from simple analysis of the limiting current using equation 5.1:

$$i_{\text{lim}} = nFAk_tC_i \qquad 5.1$$

where i_{lim} is the limiting current, n is the number of electrons transferred, F is the Faraday constant, A is the electrode area k_t is the mass transfer coefficient and C is the concentration of the species i. Hence, the effective standard heterogeneous electron transfer rate constant in both areas is much larger. Since k_t is higher than that experienced in standard CV experiments, SWNT forests should display essentially reversible behaviour for most common electrochemical techniques for outer sphere redox couples. Thus, both the closed ends and sidewalls of CVD grown

SWNT forests should be considered highly electrochemically active, and capable of fast electron transfer. Furthermore, it should not be necessary, as has been suggested by others,[23-24,50-53] to carry out any pretreatment or activation of CVD-grown SWNTs for electrochemical studies and measurements with redox couples of this type. Note that for some inner sphere processes which may need to bind directly with the electrode surface in order to undergo efficient electron transfer,[54] the chemical nature of the surface (and whether the end is open or closed) may be more important.

5.2.2 2D SWNT networks

A scheme of the SECCM setup is depicted in Figure 5-7 a). Taking into account the characteristic separation between SWNTs, it was essential that the SECCM probe was of the order of ca. 250 nm in diameter (SEM image in Figure 5-7 a)), since this dimension defines the size of the EC cell[33] when the electrolyte at the end of the pipet comes into contact with the substrate. At this length scale, individual SWNTs could be resolved, and it should be possible to distinguish between sidewalls, nanotube ends, and crossing SWNTs. The 2D SWNT network is comprised of randomly distributed interconnected SWNTs, as seen in Figure 7b. Each SWNT is grown from a single catalytic nanoparticle that is embedded at one end of the SWNT.[55-56] The density of SWNTs was above the metallic percolation threshold,[57] so after establishing macroscopic electrical contacts to the network, the sample was ready to be used without any need of post-processing cleaning steps. This was particularly important because the number of defects present in the SWNTs remains at the as grown value. Naturally, SWNTs contain no edge-plane-like sites of the type held responsible for the EC response in MWNTs;[53] also, for SWNTs grown by CVD, the ends are likely to be closed, which might be expected to lead to very

slow HET kinetics.[24-25] The only other type of defect site that one could reasonably consider is point defects in the sidewall, identified through electrodeposition.[58] These have a spacing of 100 nm – 4 μm (averaging approximately 400 nm) along the sidewall.

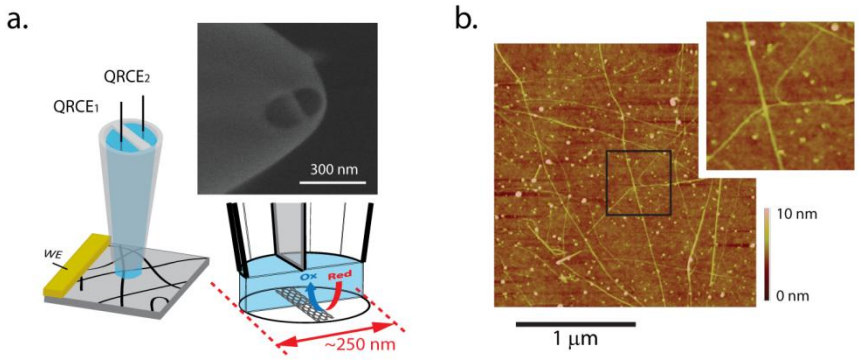

Figure 5-7: *Depiction of the SECCM setup and the 2D SWNT network samples on which studies were performed. (a) Schematic (not to scale) of the SECCM setup, showing the SECCM tip with QRCEs over a 2D SWNT network sample connected as the working electrode with a gold contact. FE-SEM image of a typical SECCM tip and the geometry for the FEM is also shown [3D simulation, making use of the symmetry plane perpendicular to the tip septum[33]]. (b) representative AFM image of SWNT network samples, with an expanded image of a junction and a bundle splitting. Catalyst particles can be seen in the AFM image but are not connected to the SWNTs and are electrochemically inactive.*

Samples were routinely characterized with atomic force microscopy (AFM), confirming a typical coverage of SWNT of approximately 4 μm/μm^2 (SWNT length / substrate area) and heights of approximately 1 nm, with high monodispersity (*vide infra*). Some SWNT bundles were also observed, as shown in the zoomed image of Figure 5-7 b), where the splitting of a bundle is seen. Further analysis of the sample with Raman spectroscopy (Figure 5-8) confirmed the presence of high quality SWNTs. The shape and position of the G peak confirmed the presence of

semiconducting (G band shoulder) and metallic SWNTs. The very small D peak intensity indicates that the SWNTs are of high quality.[59]

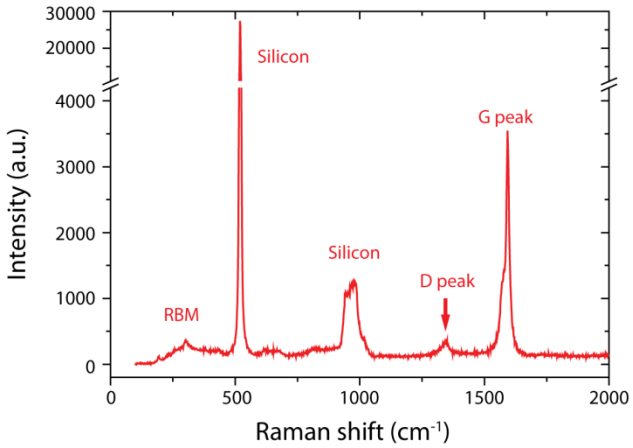

Figure 5-8: *Raman spectra for the SWNT network on a Si/SiO_2 substrate*.

Two simple one-electron processes with widely different redox potentials were employed: ferrocenylmethyl trimethylammonium ($FcTMA^+$) oxidation and ruthenium (III) hexamine ($Ru(NH_3)_6^{3+}$) reduction (in phosphate buffer pH 7.2 as supporting electrolyte). Figure 5-9 a) and b) show EC current maps, together with linescans, for these processes, with the SWNT substrates biased at the formal potential of the redox couple. The formal potentials were determined using ca 1 µm SECCM tips on freshly cleaved highly oriented pyrolytic graphite (HOPG), SPI-1 grade (SPI supplies) (Figure 5-10). In each case, the EC activity of the substrate is clearly similar to the characteristic topography of SWNT network geometries. The data show that the EC activity is mostly uniform along the length of SWNTs.

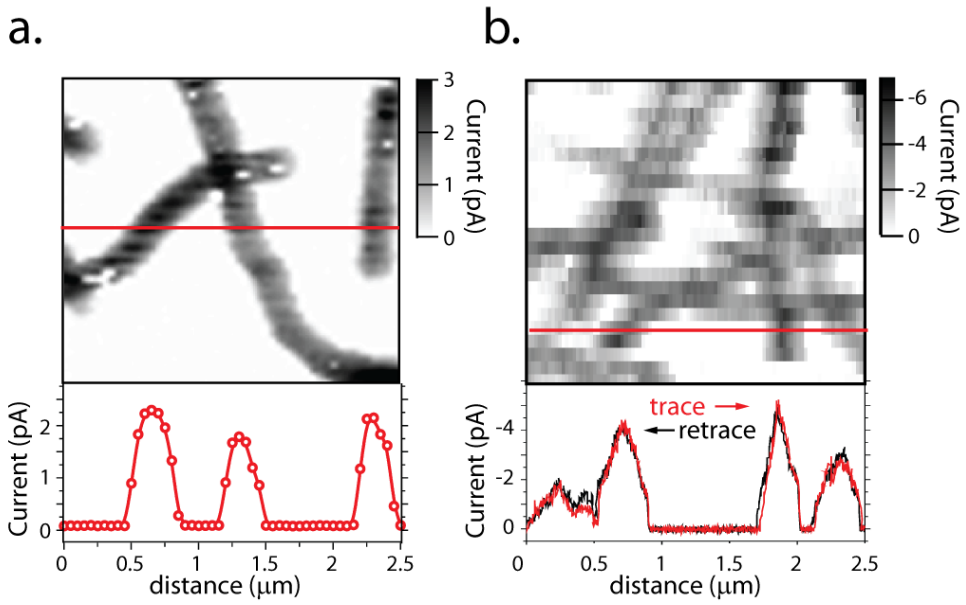

Figure 5-9: *Experimental data obtained using SECCM of the SWNT network. SECCM images (2.5 µm x 2.5 µm) of SWNT networks at the formal potential for* $FcTMA^{+/2+}$ *(2 mM) (a) and* $Ru(NH_3)_6^{3+/2+}$ *(5 mM) (b). Representative trace (a, b) and retrace (b) linescans are shown below.*

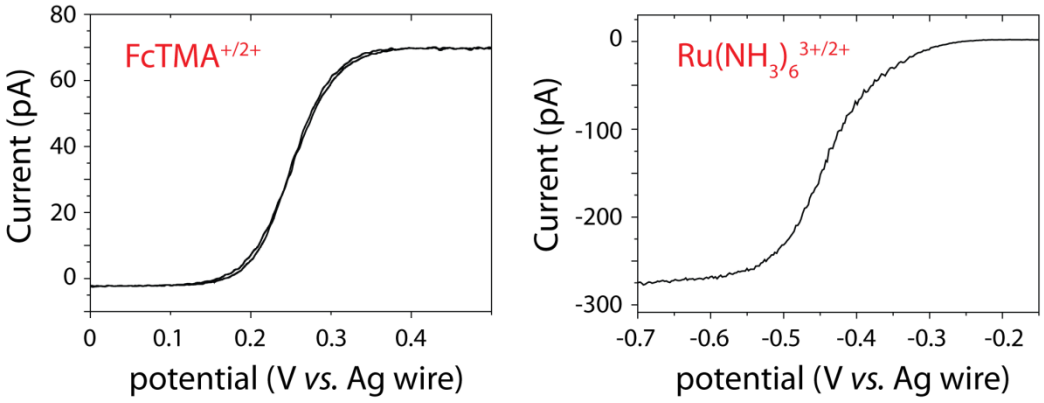

Figure 5-10: *CV (left) and LSV (right) on HOPG employing the SECCM setup, for 2 mM* $FcTMA^{+}$ *and 5 mM* $Ru(NH_3)_6^{3+}$*, respectively in phosphate buffer.*

The EC map for $FcTMA^{+}$ oxidation (Figure 5-9 a)) shows only a small variation in current across the nanotubes. This is consistent with the similar density

of states of metallic and semiconducting nanotubes[29] at this positive potential, so that electrochemistry with this mediator is relatively insensitive to the electronic nature of the SWNT. Although a highly active SWNT network is also evident for ($Ru(NH_3)_6^{3+}$) reduction (Figure 5-10 b)), there also appears to be a small proportion of SWNTs with lower ET activity (for examples, see the left hand side of the line profile in Figure 5-10 b), the EC image in Figure 5-11 and the EC current histogram in Figure 5-16 a)). This could be because the formal potential of $Ru(NH_3)_6^{3+/2+}$ lies in the charge depletion region of some of the semiconducting SWNTs,[60] diminishing HET activity;[61] and because some SWNTs may be highly defective or poorly connected[62] in the network.

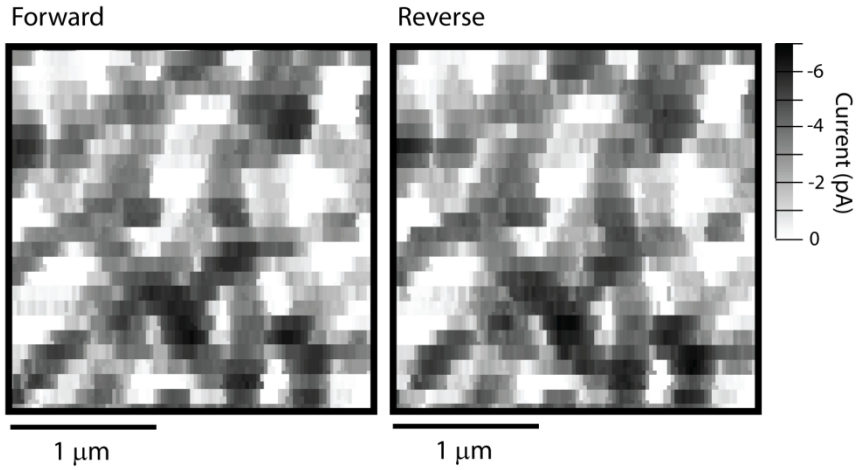

Figure 5-11: *Forward (trace) and reverse (retrace) scans of an EC map on a SWNT network for $Ru(NH_3)_6^{3+}$ reduction at the formal potential. The image area is 2.5 μm x 2.5 μm.*

The SECCM imaging procedure consisted of a bias of 500 mV applied between the two QRCEs in the SECCM pipet, inducing an ion current between the two barrels. The conductance cell was floated with respect to the working electrode surface, held at ground, so that the driving force for HET was at the formal potential

for the particular redox couple of interest. A meniscus forms at the end of the SECCM tip and acts as the electrochemical cell that is scanned across the sample.[31-33]

The instrument[31] used for the $FcTMA^{+/2+}$ studies produced an image with data points evenly spaced (typically 50 nm). The second instrument employed a continuous scanning method, providing higher spatial resolution in the tip-scan direction. The SECCM tip speed was 300 nm s^{-1}, and data were acquired at a rate of 78 Hz, yielding a spatial resolution of *ca*. 4 nm in the direction of the line scan. This imaging procedure was used for $Ru(NH_3)_6^{3+/2+}$ studies. For the studies with $Ru(NH_3)_6^{3+}$ reduction, each line scan covered the same area twice, first in the forward (trace) direction and second in the reverse (retrace) direction. Comparing the forward and reverse scans over the same area enabled us to identify any scan artifacts. Figure 5-11 shows typical images of the forward and reverse scans. Almost identical images can be seen, indicating almost no hysteresis and no contamination by the scanning probe. SECCM also acquires three complementary maps (Figures 5-12, 5-13, 5-14) simultaneously with the EC maps: *z*-piezo displacement, ion conductance, and the AC component of the ion conductance. These extra data can be viewed to confirm the stability of the meniscus size and the constancy of the tip-sample separation during an SECCM scan.

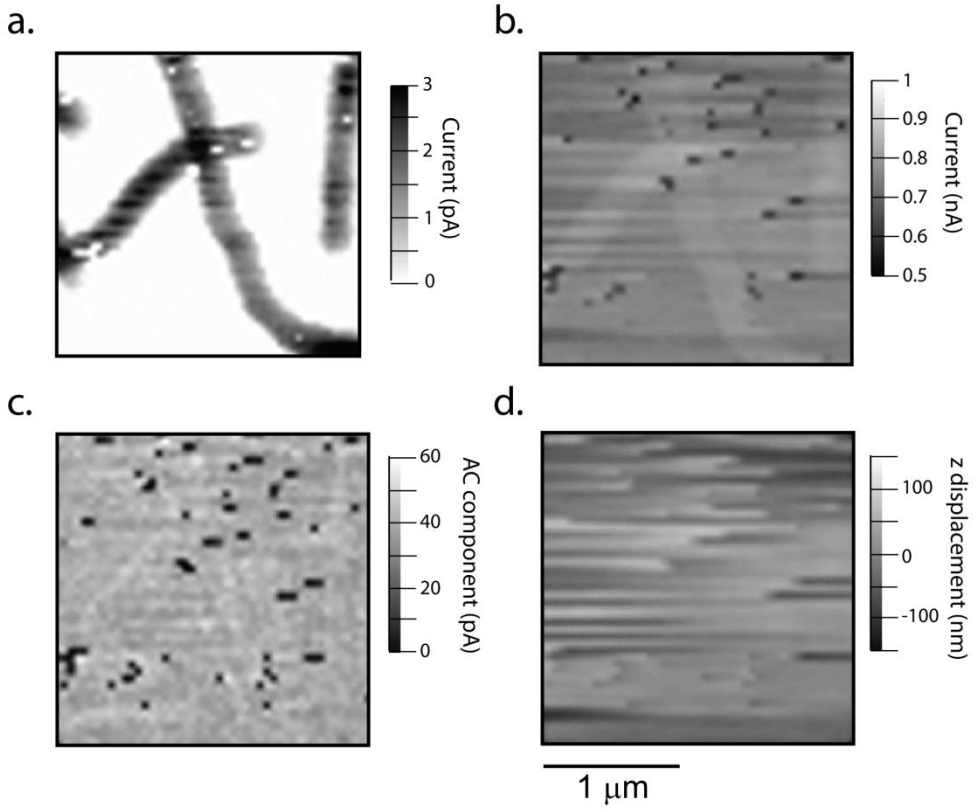

Figure 5-12: *Four complementary maps obtained by SECCM simultaneously on a SWNT network for $FcTMA^+$ oxidation at the formal potential. (a) EC current, (b) ion current, (c) AC component of the ion current, and (d) z-displacement of the SECCM probe (flattened).*

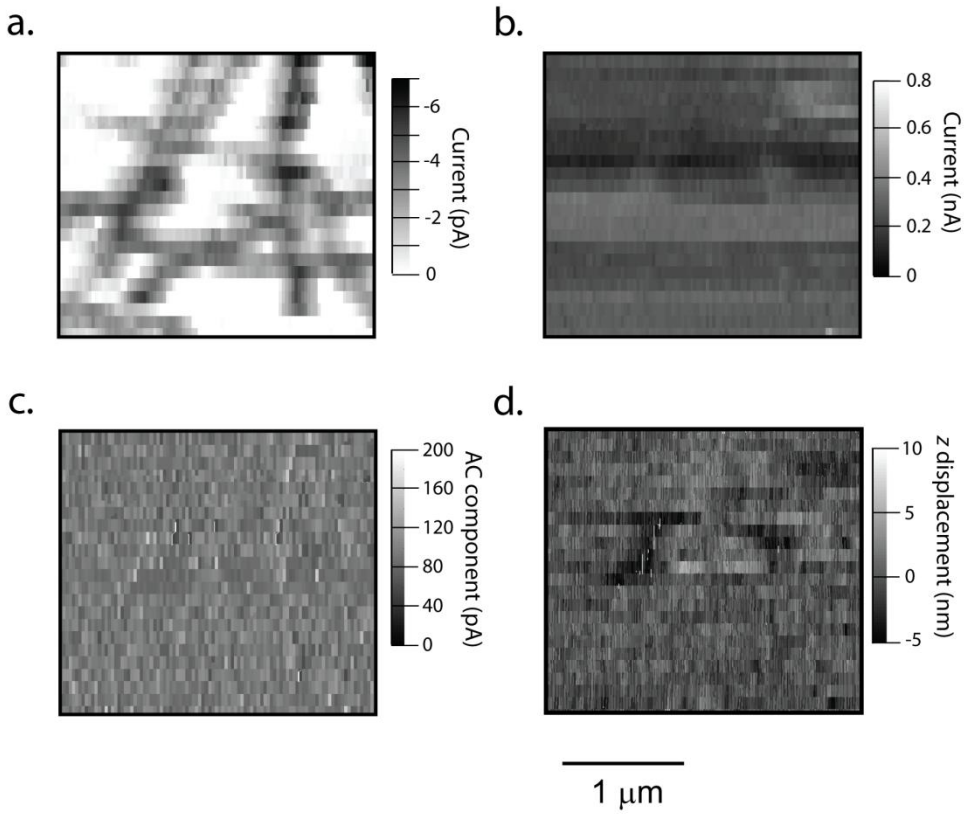

Figure 5-13: *Four maps obtained by SECCM simultaneously on a SWNT network for* $Ru(NH_3)_6^{3+}$ *reduction. (a) EC current, (b) ion current, (c) AC component of the ion current, and (d) z-displacement of the SECCM probe (flattened).*

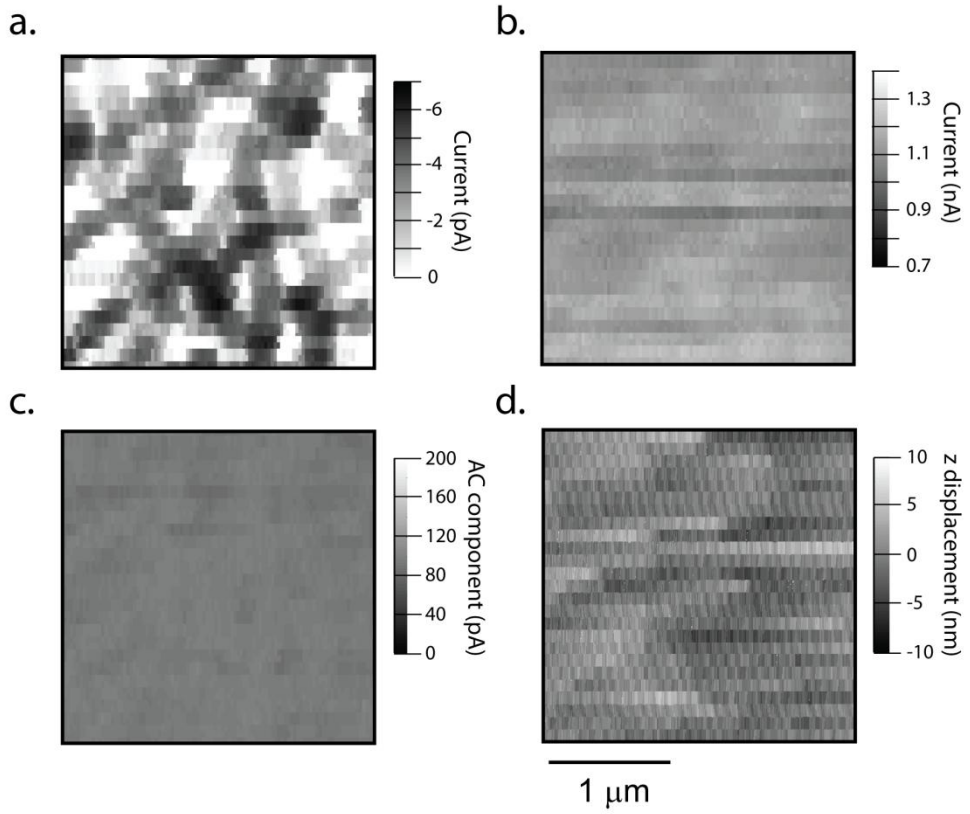

***Figure 5-14**: Four maps obtained by SECCM simultaneously on a SWNT network for $Ru(NH_3)_6^{3+}$ reduction. (a) EC current, (b) ion current, (c) AC component of the ion current, and (d) z-displacement of the SECCM probe (flattened).*

Along with the trace image in Figure 5-10 b), examples of trace and retrace linescans are also shown, with each line comprising points obtained every 4 nm. The trace and retrace linescans overlay, confirming the consistency of the measurements, accurate tracking of the surface, the absence of blocking or fouling of the SWNT, and of meniscus dragging effects.

To assign standard HET rate constants, k^0, a finite element method model of the SECCM system was developed by Dr. Michael Snowden.[33] The SECCM probe geometry was approximated to a circular based cone of radius 125 nm. Initially, the potential field and ion migration current between the two QRCEs in the SECCM

pipet were determined in the absence of a working electrode reaction by solving the steady-state Nernst–Planck equations:

$$\nabla(-D_j \nabla c_j - z_j u_j F c_j \nabla V) = 0 \quad (1)$$

$$\sum_j z_j c_j = 0 \quad (2)$$

where D_j, c_j , z_j , and u_j are the diffusion coefficient, concentration, charge, and ionic mobility of species, *j*, respectively. *F* is the Faraday constant, and *V* is the electric field (provided by the bias applied between $QRCE_1$ and $QRCE_2$, E_f, as depicted in Figure 5-7 a)). The boundary conditions were as outlined previously[33] and the potential field was calculated for a solution containing either 2 mM $FcTMA^+$ ($PF6^-$ salt) or 5 mM $Ru(NH_3)_6^{3+}$ (chloride salt) in 50 mM phosphate buffer at pH 7.2 using ion mobilities and diffusion coefficients obtained from the literature[63-64] and summarized in Table 5-1.

Species	λ_j (S cm^2 mol^{-1})	z_j	D_j (10^{-6} cm^2 s^{-1})
$Ru(NH_3)_6^{3+}$	92.4	3+	8.2
$Ru(NH_3)_6^{2+}$	61.6	2+	8.2
$FcTMA^+$	22.5	1+	6.0
$FcTMA^{2+}$	45.1	2+	6.0
PF_6^-	56.9	1-	15.1
Cl^-	76.31	1-	20.3
$H_2PO_4^-$	57	1-	9.59
HPO_4^{2-}	36	2-	7.59
H^+	349.65	1+	93.11
OH^-	198	1-	52.73

Na^+	50.08	1+	13.34
K^+	73.48	1+	19.57

Table 5-1: *Values for mobility, charge and diffusion coefficient of solution species*.

The cylindrical SWNT (diameter, d_{nt}) was approximated to a band electrode in the plane of the inert substrate, with an equivalent width $w_{nt} = (\pi/2) \cdot d_{nt}$ and a length defined by the substrate-meniscus contact area, as shown in Figure 7A. To determine the EC response at the formal potential, the majority of the substrate was considered to be insulating, with the SWNT defined as a rectangle of width w_{nt} in the plane of the substrate with a length determined by the substrate-meniscus contact area. A band approximation is reasonable,[65] especially when the HET kinetics are close to surface-limited . The width of the rectangle was related to the height of the SWNT, d_{nt}, as defined earlier. Butler-Volmer kinetics were applied to the SWNT electrode, assuming a transfer coefficient $\alpha = 0.5$, with the remainder of the surface (Si/SiO_2) inert. Mass transport to the working electrode surface was calculated by solving Eq. 1 for the electrode reactant and product species, for a typical barrel current of ca. 1 nA, using protocols described in full.[33]

When the SWNT lies across the center of the SECCM meniscus, the relative orientation between the SWNT and the SECCM probe barrels (defined by the orientation of the septum) was found to be negligible. This was assessed using simulations for the SECCM probe over an SWNT in the center of the meniscus running either along the axis of symmetry or perpendicular. The working electrode current remained at 4 pA for both orientations showing a negligible influence. Thus, unless stated otherwise, the SWNT was considered to be parallel with the septum

between the SECCM probe barrels (Figure 5-7 a)). Based on previous experimental studies,[31-33] typical tip-substrate separations in SECCM are between 25 % and 50 % of the tip radius, and a tip-substrate separation of 50 nm was considered in the present study, which was most consistent with the ion current response.[33] Further simulations proved that the effect on the current at the formal potential of changing the tip-substrate separation by up to ± 20 nm was less than 3 % for a constant ion current.

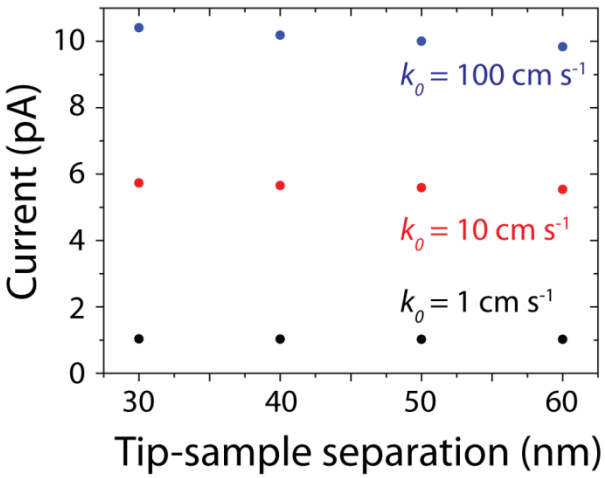

Figure 5-15: *Effect of tip-sample separation on the EC response of an SWNT of w_{nt} = 1.5 nm, held at the formal potential and positioned in the center of the SECCM meniscus. The pipet was of radius, r_p = 125 nm, filled with 5 mM $Ru(NH_3)_6^{3+}$ and 50 mM phosphate buffer solution (pH 7.2) and a barrel current of 1 nA for all heights. The response is shown for different k^0 indicated.*

SECCM images were analyzed to extract current values where the pipet most likely passed over individual SWNTs and crosspoints of SWNTs in networks. These data are summarized in Figure 5-16 as histograms of peak currents in the images at these locations. A corresponding AFM of SWNT height (equivalent to diameter, d_{nt})

is also shown for comparison. The working curves of EC current vs. Log (k^0) (with a transfer coefficient of $\alpha = 0.5$) for $d_{nt} = 1$ nm ($w_{nt} = 1.57$ nm) used to analyze these data are shown in Figure 5-16 b) and c (pipet radius of 125 nm). These curves indicate that, if SWNT heights are well-defined, k^0 approaching 30 cm s^{-1} may be accessible (where the current is ca. 90 % of the maximum transport-limited value and so distinguishable from the limit). The modal value of the current distribution for the individual SWNTs with ($Ru(NH_3)_6^{3+/2+}$) (Figure 3A) is $i_{we} = 4$ pA (± 1 pA accounts for 40% of the values) yielding $k^0 = 4 \pm 2$ cm s^{-1}. For $FcTMA^{+/2+}$, a modal current of $i_{we} = 1.8$ pA (± 0.2 pA accounts for 42% of the values) yields $k^0 = 9 \pm 2$ cm s^{-1}. Confidence in these assignments is high because these kinetic values are so far away from the reversible limit with the high mass-transport rates of SECCM. Interestingly, the value determined for $Ru(NH_3)_6^{3+/2+}$ is of the order of that found on gold nanoelectrodes, $k^0 = 13.5 \pm 2$ cm s^{-1}.[66] For $FcTMA^{+/2+}$ $k^0 = 4 \pm 2$ cm s^{-1} has been found for individual SWNT devices, with previously estimated $k^0 > 1.0 \pm 0.6$ cm s^{-1} or $k^0 > 2 \pm 1$ cm s^{-1} for this couple.[28,39]

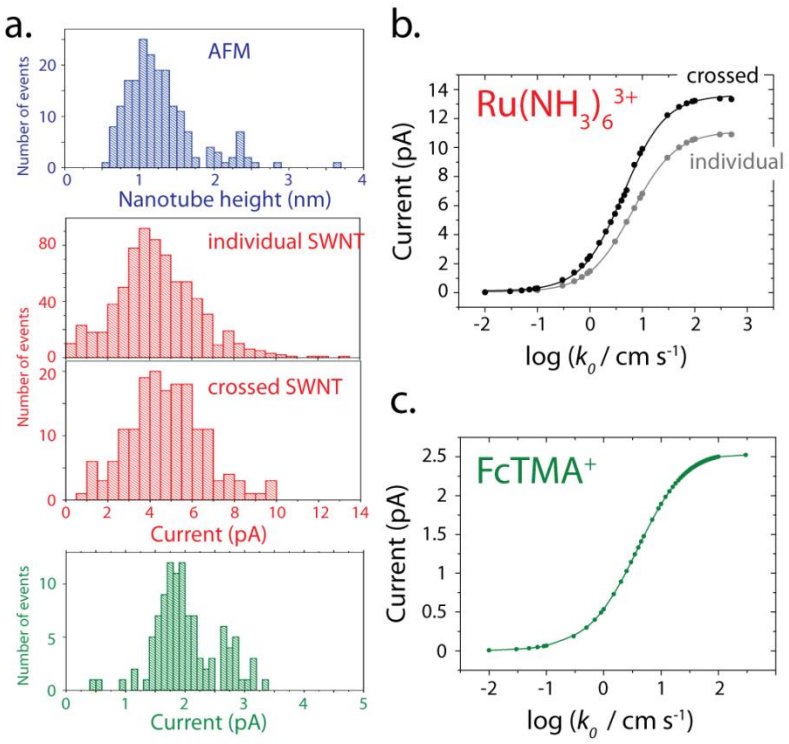

Figure 5-16: *Summary of the experimental peak EC current data and simulation results. (a) The SWNT height distribution from the AFM images. Histograms of peak current populations from SECCM images for* $Ru(NH_3)_6^{3+}$ *reduction (red) and* $FcTMA^+$ *oxidation (green) from regions of the image where individual SWNT peaks were identified. For* $Ru(NH_3)_6^{3+}$ *reduction the peak current population is also shown for points where more than one nanotube is under the tip (crossed SWNT), (b) and (c) Working curves of EC current vs standard rate constant for HET at a fully active individual SWNT of height 1 nm with* $Ru(NH_3)_6^{3+}$ *and* $FcTMA^+$ *as the redox mediator, respectively. The simulations were at the formal potential and a transfer coefficient of* $\alpha = 0.5$ *was assumed.*

The samples used for the present study were found to have a narrow range of SWNT heights, as shown in Figure 3A (blue histogram). To investigate how this variation might impact on the EC response, simulations were performed for the range of nanotube heights (converted to w_{nt} in the model) for d_{nt} between 0.8 nm and 2.75 nm, using $k^0 = 4 \pm 2$ cm s^{-1} for $Ru(NH_3)_6^{3+/2+}$ and 9 ± 2 cm s^{-1} for $FcTMA^{+/2+}$. The results, presented in Figure 5-17, indicate that the EC response changes with

nanotube diameter, from 3.5 pA to 7.5 pA for $Ru(NH_3)_6^{3+/2+}$ and from 1.7 pA to 2.4 pA for $FcTMA^{+/2+}$. This variation is thus a plausible explanation for the main part of the distributions of peak current, in which more than half of the values lie, although this is a simple analysis and k^0 may change with nanotube height.[22]

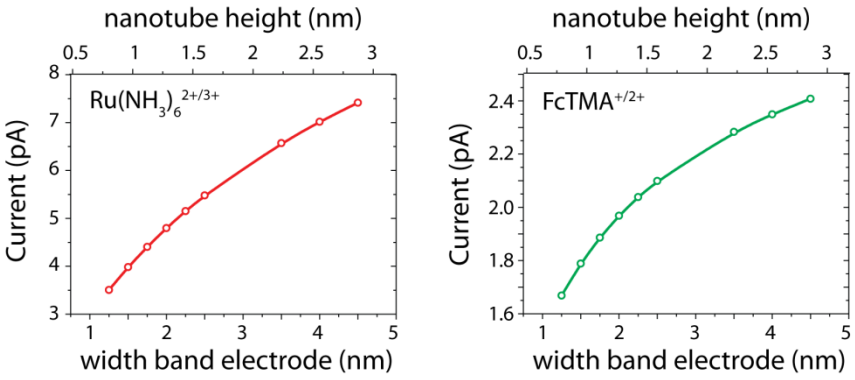

Figure 5-17: *Effect of the simulated SWNT width (equivalent height) on the working electrode current for $Ru(NH_3)_6^{3+}$ reduction (k^0 = 4 cm s^{-1}) and $FcTMA^+$ oxidation (k^0 = 9 cm s^{-1}).*

On the other hand, particularly for $Ru(NH_3)_6^{3+/2+}$, there is a small but detectable population of low currents that cannot be accounted for simply from the height distribution. This can reasonably be attributed to the presence of some semiconducting SWNTs and SWNTs with high resistance drop within parts of the ensemble. Indeed, SWNT densities from SECCM (2.6 ± 0.3 µm / µm^2) are lower than densities from AFM (3.8 ± 0.4 µm / µm^2). While this difference could partly be due to the lower spatial resolution of SECCM, it is also reasonable to postulate a proportion of SWNTs not being electrically connected[26] and low HET rates at some semiconducting nanotubes . One of the characteristic features of 2D SWNT networks is the presence of nanotube junctions. The mapping feature of SECCM allowed for the viewing of the EC activity of such arrangements. A slight increase in the modal current was observed, compared to the individual SWNT case (Figure 5-16 a)), but

taking account of the extra active area (compare individual and crossed SWNT working curves in Figure 5-16 b)), the corresponding k^0 value was similar, $k^0 = 3 \pm 2$ cm s^{-1}.

It has been suggested[24-25,50,53,67] that sidewalls are electrochemically inactive in CNTs and that only edge-plane-like sites and open oxygenated nanotube ends are active. Our work shows this earlier hypothesis is incorrect. For the SWNT network, there were no obvious edge-plane sites, and the ends are most likely to be closed.[55] High and similar activity across different sites in SWNT networks was observed.

The possibility if defects in the sidewall could be solely responsible for the SECCM observations was considered. Given the defect density attributed from selective electrodeposition,[58] vide supra, the SECCM pipet would be expected to encounter only one defect when passing over an SWNT. This case was considered, simulating a defect (at most) as a square of length 1 nm positioned in the plane of an inert substrate, for $Ru(NH_3)_6^{3+/2+}$. The resulting working curve (Figure 5-18 a)) of EC current vs. Log (k^0) at the formal potential provides two important observations: (i) the discernible range of k^0 values is now up to 1000 cm s^{-1}, due the very high mass transport to a nm-scale electrode; and (ii) the maximum mass-transport limited current for a 1 nm sized defect is 0.46 pA (for $k^0 > 1000$ cm s^{-1}), an order of magnitude lower than the modal value observed experimentally, and this is for an unfeasibly high rate constant.

Next, an increase in the number of side-wall defects was considered, up to three in the area under interrogation, to simulate a maximum possible EC response for an SWNT with defects spaced ca. 100 nm. The EC current vs. Log (k^0) working curve for this case yields a maximum current $i_{we} = 1.5$ pA, but only for $k^0 > 1000$ cm s^{-1}. This rate constant is unfeasibly high, yet this current and lower values are only

evident in < 10 % of the nanotubes visualized. Thus, the overwhelming majority of SWNTs have an EC activity that can only reasonably be explained based on considerable intrinsic SWNT sidewall activity. The high spatial resolution of SECCM during scanning allowed tracking of EC currents across individual SWNTs. The resulting peak profiles also indicate that the EC current response is best explained by HET activity intrinsic to SWNT sidewalls. Figure 5-18 b) compares a simulation for scanning over a fully active SWNT (w_{nt} = 1.5 nm and k^0 = 4 cm s^{-1}) with a typical, and frequently observe, experimental example linescan for $Ru(NH_3)_6^{3+}$ reduction. It is evident that there is a good match to the shape and magnitude of the profile, assuming a uniformly active tube. Note that such profiles provide an excellent test of the uniformity of SWNT activity as the SWNT length accessed changes in a systematic manner as the SECCM meniscus scans over it.

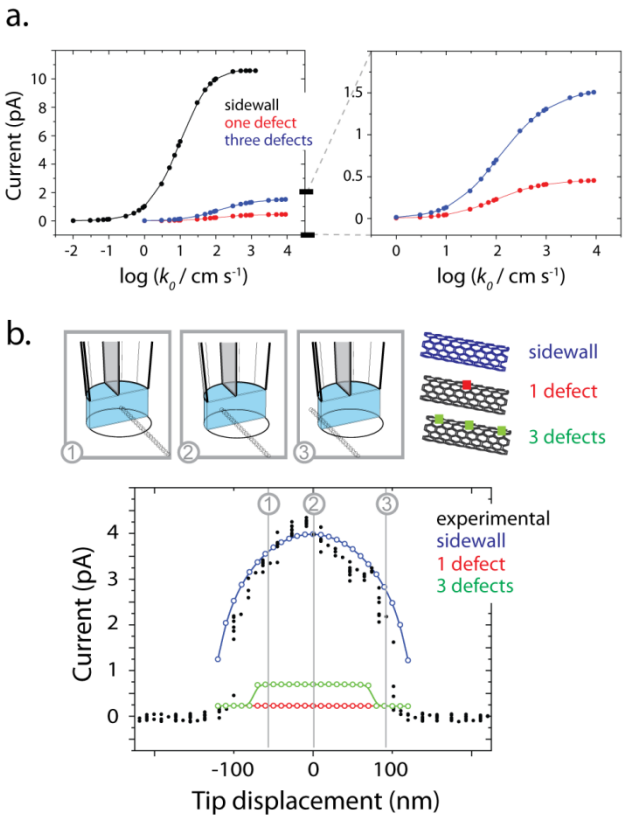

Figure 5-18: *Comparison of experimental data with simulated data for fully active SWNT sidewall, one defect and three defects. (a) Working curves of EC current vs, standard rate constant for HET of a fully active individual SWNT, one point defect and three point defects (with the SWNT central under the pipet meniscus). (b) Experimental (points) for the current response of an SECCM probe translated over a portion of an individual SWNT, compared to simulations for full sidewall activity (blue, k^0 = 4 cm s^{-1}), one active defect (red, k^0 = 100 cm s^{-1}) and three active defects (green, k^0 = 100 cm s^{-1}).*

Simulations of moving the SECCM probe across an SWNT containing one and three sidewall defects with an exaggerated value of k^0 = 100 cm s^{-1} were also performed and compared (Figure 5-18 b)). Besides the large difference in the EC response compared to the sidewall active case, there is also a significant difference in the shape of the line scan profile, with an abrupt change in current for the defect,

depending on whether or not a defect is accessed. Furthermore, there is negligible variation of the EC current response for the single active site. Note, additionally, that the defect simulations are for the most favorable case where the defect is located central to the scanned meniscus of the SECCM pipet. On this basis, it was further deduced that the most appropriate model for electrochemistry at pristine, untreated SWNTs is one where the large majority of the sidewalls display high intrinsic EC activity.

5.3 Conclusions

In summary, a novel approach for interrogating the electrochemistry of different parts of SWNTs in a forest arrangement and a 2-dimensional network, using a mobile nanoscopic electrochemical cell, has been demonstrated. In this way the electrochemical activity of the mentioned SWNT arrangements, can be studied in their native state, in any desired location, at high spatial resolution, without the need for sample processing. Using this arrangement, it has been proven that a SWNT end does not need to be open for it support fast electrochemistry with outer sphere redox couples. Furthermore, by measuring the EC currents as a function of probe position at the formal potential of two redox couples, it was determined that the majority of SWNTs within a network are more or less uniformly active on the length scale of high resolution SECCM. The images provided striking quantitative information on EC activity across different types of sites in SWNTs (sidewall and ends) and in 2D networks (crosspoints). Quantitative information has not only come from the analysis of peak currents in SECCM maps (when the SWNT lies under the center of the SECCM pipet) but also from the analysis of line profiles in which the line shape

across an SWNT running across the Si/SiO_2 substrate perpendicular to the linescan direction can be fitted to a single rate constant for a uniformly active SWNT.

SECCM accesses very high mass-transport rates, which allows the ready assignment of rate constants with high accuracy, and proves that a high proportion of the SWNTs detected had k^0 in the narrow range 4 ± 2 cm s^{-1} for $Ru(NH_3)_6^{3+/2+}$ and 9 ± 2 cm s^{-1} for $FcTMA^{+/2+}$. Furthermore, for both couples, all SWNTs detected by SECCM show $k^0 > 0.1$ cm s^{-1}. Thus, in practical terms, SWNT sidewalls will show fast HET for most common electrochemical techniques that operate with much lower mass transport coefficients than these standard rate constants. As such, SWNTs should be viewed as highly active electrochemical materials, at least for outer-sphere redox couples of the type studied herein. This new understanding of electrochemistry at SWNTs clarifies misconceptions that have arisen from different views in the literature on the electroactivity of SWNT materials; also, it has implications for related materials such as graphene[68] and graphite.[40]

5.4 References

(1) Sun, Y. P.; Fu, K. F.; Lin, Y.; Huang, W. J. *Accounts of Chemical Research* **2002**, *35*, 1096.

(2) Chen, R. J.; Bangsaruntip, S.; Drouvalakis, K. A.; Wong Shi Kam, N.; Shim, M.; Li, Y.; Kim, W.; Utz, P. J.; Dai, H. *Proceedings of the National Academy of Sciences* **2003**, *100*, 4984.

(3) Williams, K. A.; Veenhuizen, P. T. M.; de la Torre, B. G.; Eritja, R.; Dekker, C. *Nature* **2002**, *420*, 761.

(4) Avouris, P.; Chen, Z. H.; Perebeinos, V. *Nat. Nanotechnol.* **2007**, *2*, 605.

(5) Kong, J.; Franklin, N. R.; Zhou, C. W.; Chapline, M. G.; Peng, S.; Cho, K. J.; Dai, H. J. *Science* **2000**, *287*, 622.

(6) Heller, I.; Janssens, A. M.; Mannik, J.; Minot, E. D.; Lemay, S. G.; Dekker, C. *Nano Lett.* **2008**, *8*, 591.

(7) Toma, F. M.; Sartorel, A.; Iurlo, M.; Carraro, M.; Parisse, P.; Maccato, C.; Rapino, S.; Rodriguez Gonzalez, B.; Amenitsch, H.; Da Ros, T.; Casalis, L.; Goldoni, A.; Marcaccio, M.; Scorrano, G.; Scoles, G.; Paolucci, F.; Prato, M.; Bonchio, M. *Nature Chemistry* **2010**, *2*, 826.

(8) Lee, S. W.; Yabuuchi, N.; Gallant, B. M.; Chen, S.; Kim, B.-S.; Hammond, P. T.; Shao-Horn, Y. *Nat. Nanotechnol.* **2010**, *5*, 531.

(9) Choi, Y.; Moody, I. S.; Sims, P. C.; Hunt, S. R.; Corso, B. L.; Perez, I.; Weiss, G. A.; Collins, P. G. *Science* **2012**, *335*, 319.

(10) Star, A.; Tu, E.; Niemann, J.; Gabriel, J.-C. P.; Joiner, C. S.; Valcke, C. *Proceedings of the National Academy of Sciences of the United States of America* **2006**, *103*, 921.

(11) Snow, E. S.; Perkins, F. K.; Houser, E. J.; Badescu, S. C.; Reinecke, T. L. *Science* **2005**, *307*, 1942.

(12) Dumitrescu, I.; Edgeworth, J. P.; Unwin, P. R.; Macpherson, J. V. *Adv. Mater.* **2009**, *21*, 3105.

(13) Gong, K.; Du, F.; Xia, Z.; Durstock, M.; Dai, L. *Science* **2009**, *323*, 760.

(14) Hambourger, M.; Moore, T. A. *Science* **2009**, *326*, 1355.

(15) Kauffman, D. R.; Shade, C. M.; Uh, H.; Petoud, S.; Star, A. *Nature Chemistry* **2009**, *1*, 500.

(16) Ding, M.; Tang, Y.; Gou, P.; Reber, M. J.; Star, A. *Adv. Mater.* **2011**, *23*, 536.

(17) Xu, W.; Shen, H.; Kim, Y. J.; Zhou, X.; Liu, G.; Park, J.; Chen, P. *Nano Lett.* **2009**, *9*, 3968.

(18) Quinn, B. M.; Dekker, C.; Lemay, S. G. *J. Am. Chem. Soc.* **2005**, *127*, 6146.

(19) Day, T. M.; Unwin, P. R.; Macpherson, J. V. *Nano Lett.* **2007**, *7*, 51.

(20) Bahr, J. L.; Yang, J. P.; Kosynkin, D. V.; Bronikowski, M. J.; Smalley, R. E.; Tour, J. M. *J. Am. Chem. Soc.* **2001**, *123*, 6536.

(21) Odom, T. W.; Huang, J. L.; Kim, P.; Lieber, C. M. *J. Phys. Chem. B* **2000**, *104*, 2794.

(22) Heller, I.; Kong, J.; Williams, K. A.; Dekker, C.; Lemay, S. G. *J. Am. Chem. Soc.* **2006**, *128*, 7353.

(23) Banks, C. E.; Moore, R. R.; Davies, T. J.; Compton, R. G. *Chem. Commun.* **2004**, 1804.

(24) Holloway, A. F.; Toghill, K.; Wildgoose, G. G.; Compton, R. G.; Ward, M. A. H.; Tobias, G.; Llewellyn, S. A.; Ballesteros, B.; Green, M. L. H.; Crossley, A. *J. Phys. Chem. C* **2008**, *112*, 10389.

(25) Chou, A.; Bocking, T.; Singh, N. K.; Gooding, J. J. *Chem. Commun.* **2005**, 842.

(26) Bertoncello, P.; Edgeworth, J. P.; Macpherson, J. V.; Unwin, P. R. *J. Am. Chem. Soc.* **2007**, *129*, 10982.

(27) Dumitrescu, I.; Unwin, P. R.; Wilson, N. R.; Macpherson, J. V. *Anal. Chem.* **2008**, *80*, 3598.

(28) Dudin, P. V.; Snowden, M. E.; Macpherson, J. V.; Unwin, P. R. *Acs Nano* **2011**, *5*, 10017.

(29) Heller, I.; Kong, J.; Heering, H. A.; Williams, K. A.; Lemay, S. G.; Dekker, C. *Nano Lett.* **2005**, *5*, 137.

(30) Kim, J.; Xiong, H.; Hofmann, M.; Kong, J.; Amemiya, S. *Anal. Chem.* **2010**, *82*, 1605.

(31) Ebejer, N.; Schnippering, M.; Colburn, A. W.; Edwards, M. A.; Unwin, P. R. *Anal. Chem.* **2010**, *82*, 9141.

(32) Lai, S. C. S.; Dudin, P. V.; Macpherson, J. V.; Unwin, P. R. *J. Am. Chem. Soc.* **2011**, *133*, 10744.

(33) Snowden, M. E.; Guell, A. G.; Lai, S. C. S.; McKelvey, K.; Ebejer, N.; O'Connell, M. A.; Colburn, A. W.; Unwin, P. R. *Anal. Chem.* **2012**.

(34) Edgeworth, J. P.; Wilson, N. R.; Macpherson, J. V. *Small* **2007**, *3*, 860.

(35) Futaba, D. N.; Hata, K.; Yamada, T.; Hiraoka, T.; Hayamizu, Y.; Kakudate, Y.; Tanaike, O.; Hatori, H.; Yumura, M.; Iijima, S. *Nat. Mater.* **2006**, *5*, 987.

(36) Fan, S. S.; Chapline, M. G.; Franklin, N. R.; Tombler, T. W.; Cassell, A. M.; Dai, H. J. *Science* **1999**, *283*, 512.

(37) Huang, H.; Liu, C. H.; Wu, Y.; Fan, S. S. *Adv. Mater.* **2005**, *17*, 1652.

(38) Wang, J. *Electroanalysis* **2005**, *17*, 7.

(39) Dumitrescu, I.; Dudin, P. V.; Edgeworth, J. P.; Macpherson, J. V.; Unwin, P. R. *J. Phys. Chem. C* **2010**, *114*, 2633.

(40) Lai, S. C. S.; Patel, A. N.; McKelvey, K.; Unwin, P. R. *Angewandte Chemie (International ed. in English)* **2012**, *51*, 5405.

(41) Gong, K.; Chakrabarti, S.; Dai, L. *Angewandte Chemie International Edition* **2008**, *47*, 5446.

(42) Huang, X.-J.; Im, H.-S.; Yarimaga, O.; Kim, J.-H.; Jang, D.-Y.; Lee, D.-H.; Kim, H.-S.; Choi, Y.-K. *J. Electroanal. Chem.* **2006**, *594*, 27.

(43) Dresselhaus, M. S.; Dresselhaus, G.; Saito, R.; Jorio, A. *Phys. Rep.-Rev. Sec. Phys. Lett.* **2005**, *409*, 47.

(44) Burt, D. P.; Whyte, W. M.; Weaver, J. M. R.; Glidle, A.; Edgeworth, J. P.; Macpherson, J. V.; Dobson, P. S. *J. Phys. Chem. C* **2009**, *113*, 15133.

(45) Pumera, M. *Langmuir* **2007**, *23*, 6453.

(46) Kruusma, J.; Mould, N.; Jurkschat, K.; Crossley, A.; Banks, C. E. *Electrochem. Commun.* **2007**, *9*, 2330.

(47) Pumera, M.; Iwai, H. *J. Phys. Chem. C* **2009**, *113*, 4401.

(48) Stuart, E. J. E.; Pumera, M. *J. Phys. Chem. C* **2010**, *114*, 21296.

(49) Hata, K.; Futaba, D. N.; Mizuno, K.; Namai, T.; Yumura, M.; Iijima, S. *Science* **2004**, *306*, 1362.

(50) McCreery, R. L. *Chemical Reviews* **2008**, *108*, 2646.

(51) Pumera, M. *Chem.-Eur. J.* **2009**, *15*, 4970.

(52) Banks, C. E.; Compton, R. G. *Analyst* **2006**, *131*, 15.

(53) Banks, C. E.; Davies, T. J.; Wildgoose, G. G.; Compton, R. G. *Chem. Commun.* **2005**, 829.

(54) Bard, A. J. *J. Am. Chem. Soc.* **2010**, *132*, 7559.

(55) Hofmann, S.; Sharma, R.; Ducati, C.; Du, G.; Mattevi, C.; Cepek, C.; Cantoro, M.; Pisana, S.; Parvez, A.; Cervantes-Sodi, F.; Ferrari, A. C.; Dunin-Borkowski, R.; Lizzit, S.; Petaccia, L.; Goldoni, A.; Robertson, J. *Nano Lett.* **2007**, *7*, 602.

(56) Colomer, J. F.; Stephan, C.; Lefrant, S.; Van Tendeloo, G.; Willems, I.; Konya, Z.; Fonseca, A.; Laurent, C.; Nagy, J. B. *Chem. Phys. Lett.* **2000**, *317*, 83.

(57) Wilson, N. R.; Guille, M.; Dumitrescu, I.; Fernandez, V. R.; Rudd, N. C.; Williams, C. G.; Unwin, P. R.; Macpherson, J. V. *Anal. Chem.* **2006**, *78*, 7006.

(58) Fan, Y. W.; Goldsmith, B. R.; Collins, P. G. *Nat. Mater.* **2005**, *4*, 906.

(59) Dudin, P. V.; Unwin, P. R.; Macpherson, J. V. *Physical Chemistry Chemical Physics* **2011**, *13*, 17146.

(60) Day, T. M.; Unwin, P. R.; Wilson, N. R.; Macpherson, J. V. *J. Am. Chem. Soc.* **2005**, *127*, 10639.

(61) Gerischer, H. *Electrochimica Acta* **1990**, *35*, 1677.

(62) Fuhrer, M. S.; Nygard, J.; Shih, L.; Forero, M.; Yoon, Y. G.; Mazzoni, M. S. C.; Choi, H. J.; Ihm, J.; Louie, S. G.; Zettl, A.; McEuen, P. L. *Science* **2000**, *288*, 494.

(63) Lide, D. *CRC Handbook of Chemistry and Physics*; CRC Press: Cleveland OH, 2001.

(64) Newman, JS.; Thomas-Alyea, KE. *Electrochemical Systems*; Wiley-Interscience: New York, 2004.

(65) Amatore, C.; Deakin, M. R.; Wightman, R. M. *J. Electroanal. Chem.* **1987**, *225*, 49.

(66) Velmurugan, J.; Sun, P.; Mirkin, M. V. *J. Phys. Chem. C* **2009**, *113*, 459.

(67) Gooding, J. J.; Chou, A.; Liu, J.; Losic, D.; Shapter, J. G.; Hibbert, D. B. *Electrochem. Commun.* **2007**, *9*, 1677.

(68) Güell, A. G.; Ebejer, N.; Snowden, M. E.; Macpherson, J. V.; Unwin, P. R. *J. Am. Chem. Soc.* **2012**, *134*, 7258.

CHAPTER 6

Fabrication and characterisation of dual barrel SECM – SICM probes

This chapter focuses on the fabrication of dual barrel carbon nanoprobes DBCNP. These comprise of a dual barrel (theta) capillary, with one side filled with pyrolytic carbon, for use as an SECM electrode, and the other left open for use as an SICM probe. A detailed characterisation of the carbon electrode will be presented using electrochemistry, electron microscopy and brief spectroscopic analysis. Examples of the DBCNP probes being used in combined SECM-SICM imaging are demonstrated by reference to experiments performed by Dr. Y. Takahashi (Imperial College, London and the work presented performed at the National Physical Laboratory (NPL).

6.1 Introduction

The dynamics of chemical and biological, interfacial processes are of great interest, with the basic processes occurring at the nanoscale. To truly understand the behaviour of these systems, measurements must be performed at this level and have high temporal resolution. One such technique for probing interfacial processes is scanning electrochemical microscopy (SECM), overviewed in Chapter 1, but the lack of a reliable distance control method has made it extremely difficult to migrate from microscale to nanoscale electrodes.[1] Various attempts have been made using

hybrid techniques, such as SECM-AFM,[2-5] shear force SECM[6] and also SECM-SICM[7-8] but all these variants required specialist probes that are difficult and time consuming to make.[9] In this chapter a method for fabricating nanoscale SECM-SICM probes within a couple of minutes is described, making use of the precise positioning and distance regulation of SICM, whilst adding the chemical selectivity of SECM (both techniques are described in detail in Chapter 1.

6.2 Experimental

The probe fabrication method developed involved the pulling of quartz theta capillaries down to required dimensions (typically in the range of 20 nm to 200 nm) using a laser puller (Sutter instrument P-2000). Once pulled, one side of the theta pipet was sealed using 'Blu-Tack' and the other side left open. The pipet was then fixed to a rubber tube, again using 'Blu-Tack', with a carbon feedstock flowing through (methane or butane) and placed in a holder with another quartz pipet fixed opposite, through which argon was flowed, as shown in Figure 6-1. The two pipets were then pushed close together with the pipet flowing argon through covering the end of the theta pipet. A blowtorch (culinary type) was then used to heat the covered end, igniting the carbon feedstock to produce a solid carbon electrode, pyrolytically. Care should be taken when heating the capillary, making sure all gas connections were sealed, using a methane sensor (Crowcon tetra) in the vicinity of the experiment.

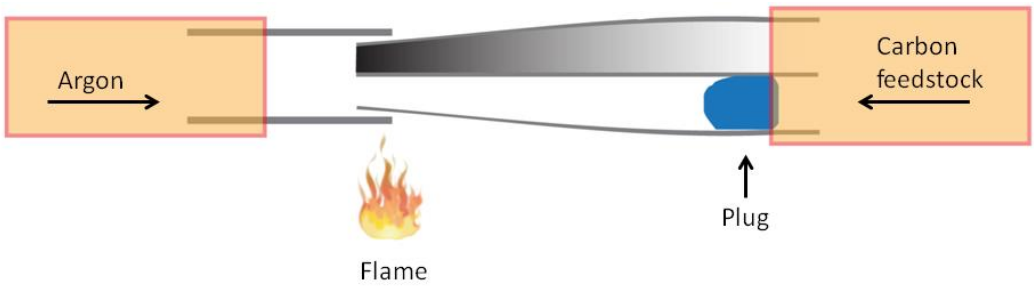

Figure 6-1: *A Schematic of the setup used to fabricate DBCNP.*

6.4 Results and discussion

This method was then further improved by using omnifit plastic fitting and O-rings, creating a much tighter seal around the theta pipet, shown in Figure 6-2. It was found that the success rate of the carbon probe fabrication improved.

Figure 6-2: *An optical image of the holder used for DBCNP fabrication.*

The Raman spectra shown in Figure 6-3 indicating shows the different data obtained for two types of probes the red line using the 'Blu Tack' sealing method and the black line, the omnifit sealing method. Peaks were fit to a Lorenztian distribution, to yield D to G peak ratios of 3.17:1 for the red line and 1.93:1 for the black line. The G peak (around 1580 cm^{-1}) is indicative of graphitic carbon present (sp^2), whilst the D peak (around 1300 cm^{-1}) describes the sp^3 carbon, a lower D to G

peak ratio is indicative of a higher quality electrode due to the larger amount of graphitic carbon present. The increase in electrode quality is most likely due to a lower feedstock to air mixture.

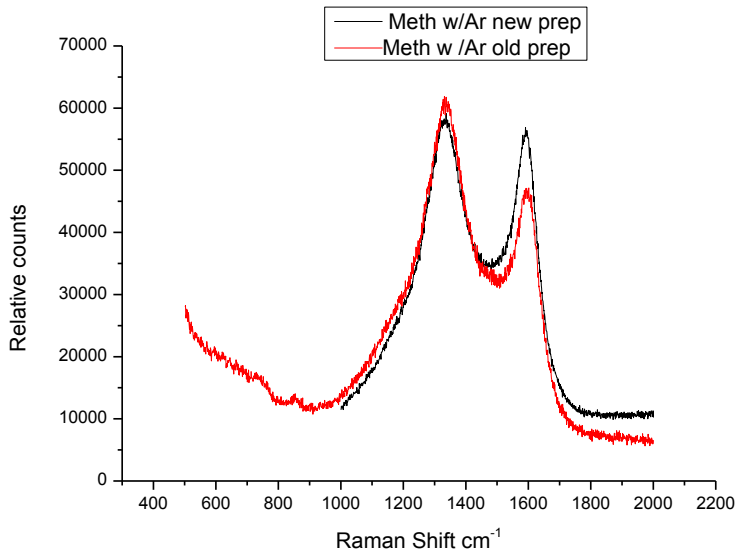

Figure 6-3: *Raman spectra of the deposited carbon with one of the dual capillary channels. Black line represents the effect of the omnifit sealing method compared to the 'Blu Tack' sealing method (red line).*

Electrodes were also characterised using scanning electron microscopy (SEM), with typical examples shown in Figure 6-4. Figure 6-4 a) shows the DBCNP with the left side filled a solid carbon electrode. This particular probe was used experimentally, hence the salt crystals around the edges, the carbon electrode appears quite solid with little to no recession (subject to resolution). Figure 6-4 b) shows a case where the quartz surrounding broke off revealing a solid carbon structure. Figure c shows that probes can be fabricated down to radii less than 10 nm.

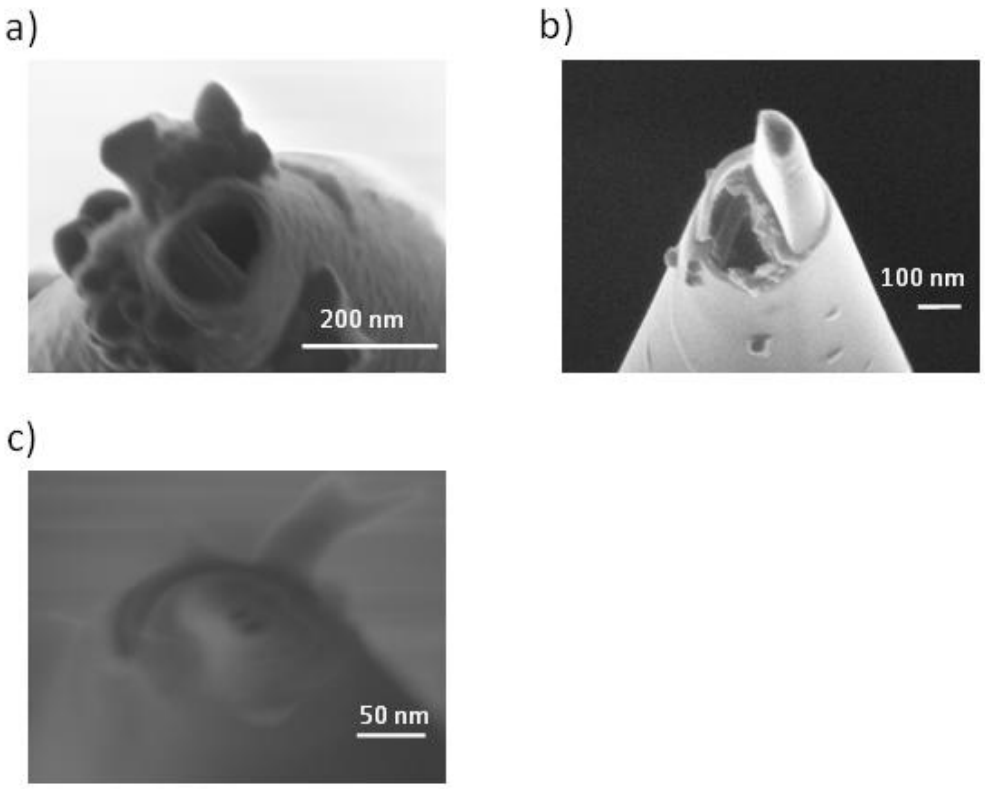

Figure 6-4: *SEM images of typical DBCNPs a) shows a DBCNP image after being used with salt crystals around the edges, b) a probe with the quartz end broken off*[10] *and c) probes down to 20 nm total diameter*.[10]

In order to characterise the probes electrochemically, a copper wire was inserted into the channel where the carbon had been deposited and using a patch clamp current amplifier (AXON instruments) a potential was applied using a LabView interface (described in Chapter 2) and the current at the electrode measured. Cyclic voltammetry (CV) was used to assess the quality of the electrodes and also the effective tip radius, using both ferocenemethanol ($FcCH_2OH$) oxidation and ruthenium (iii) hexamine chloride ($Ru(NH_3)_6^{3+}$) reduction as redox processes. CVs were typically run at 100 mV s^{-1}, although occasionally a range of scan rates were used, up to 1 Vs^{-1}, to determine the quality of the electrode. The probes were assumed to be disk type electrodes with a glass radius to electrode radius (RG) value

of 1.5 (determined from FE-SEM images) and the steady state currents were described by the equation:[11]

$$i_d = 4.64nFC^*Da \qquad 6.1$$

where n is the number of electrons transferred, F is the Faraday constant, D = 6.5 x 10^{-6} cm^2 s^{-1} is the diffusion coefficient of $FcCH_2OH$ and D = 8.2 x 10^{-6} cm^2 s^{-1} for $Ru(NH_3)_6^{3+}$, C^* is the concentration of the redox mediator and a is the tip radius.

Using equation 6.1 the effective radii of the carbon electrodes were calculated yielding an 87 nm radius for the electrode described by the voltammogram in figure 6-5 a), 19 nm for b) 1.63 nm for c) and 34 nm for d). Figure 6-5 d) shows the electrochemical response for a DBCNP at different scan rates (100 mV s^{-1}, 500 mV s^{-1} and 1V s^{-1}), a steady-state diffusion limited response is observed even for high scan rates, indicating that the electrodes are of planar geometry. The values determined for the radii are only approximate values and the small sizes could also be due to recessed electrodes or only a small part of the carbon being electrochemically active.

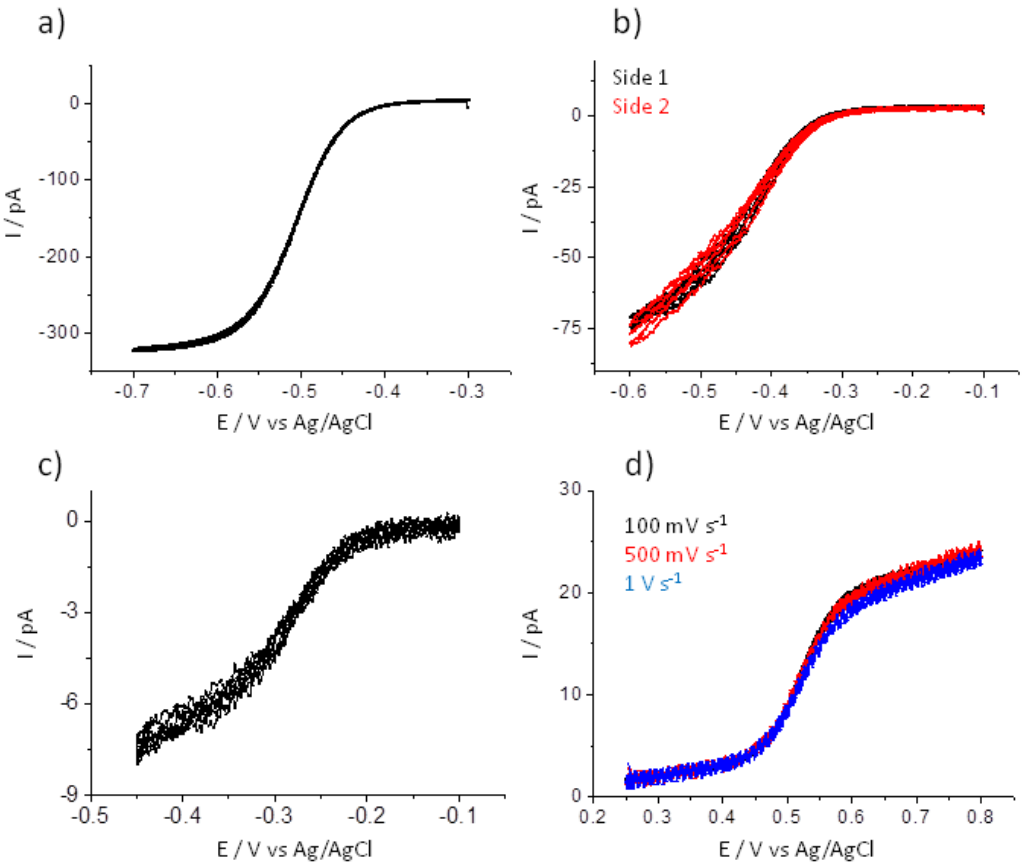

Figure 6-5: *Typical cyclic voltammograms for the DBCNP. Parts a to c are performed using 10 mM* $Ru(NH_3)_6^{3+/2+}$*, whilst d is using 2 mM FcMeOH with a scan rate of 100 mV* s^{-1} *unless indicated. Figure b overlays two half of a pipet fabricated into carbon electrodes showing a high rate of reproducibility, with d showing similar behaviour for different scan rates.*

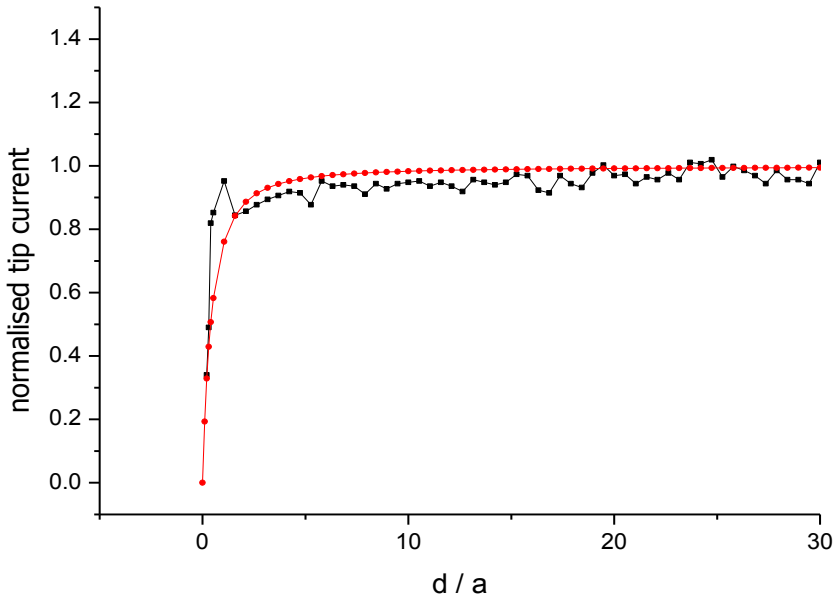

Figure 6-6: *An approach curve in negative feedback for the DBCNP analysed by CV in figure 6-4 b) (black line), overlayed with a theoretical approach curve (red line) using an RG value of 1.51.*

Using approach curves, operated in SECM negative feedback mode, the carbon electrodes were characterised and a typical one is shown in Figure 6-5 for the electrode described in figure 6-4 b. The limiting current drops to 33% of its original value, which is a reasonable value for this size probe (19 nm radius). The theoretical approach curve fits reasonably well indicating that an RG value of 1.51 is a realistic approximation also that the electrode was of planar geometry.[12]

Once the behaviour of the electrodes was understood, combined SECM-SICM imaging was performed in a hopping mode type regime, described in chapter 1. The open channel of the theta probe was filled with phosphate buffer and a silver / silver chloride wire was inserted. A potential was applied between the SICM electrode and a reference electrode, held at ground, in solution, typically 100 - 200

mV and an ion current was measured between them. The SECM part of the probe was connected as described previously and a potential was applied again with respect to the reference electrode in solution. Imaging was performed on an Ionscope SICM platform in which the imaging operation is described in detail elsewhere.[10,13]

The capability of the probes was demonstrated by imaging nanopores (pore radii ca. 100nm) in polyethylene terephthalate (PET) membranes where simultaneous topographical and electrochemical images were recorded (figure 6-6 a). Both sides of the membrane contained phosphate buffer saline and 1 mM $FcCH_2OH$. The topographical features correlate well with the electrochemical ones and a decrease in SECM current is observed over the pores due to the position of the probe entering the pore and blocking the diffusion of species, when controlled by SICM feedback. The system was also demonstrated on an interdigitated platinum array showing an increase in current over the bands, corresponding to the redox cycling of $FcCH_2OH$ (figure 6b)). Figure 6-6 c) shows the corresponding topographical and electrochemical maps of neurons visualising the permeation of $FcCH_2OH$ through the cell membrane. These images demonstrate the power of this technique, showing the ability to study soft tissue samples by means of non contact scanned probe microscopy, controlled by SICM feedback. Details of the experimentation are described by Takahashi et al.[10]

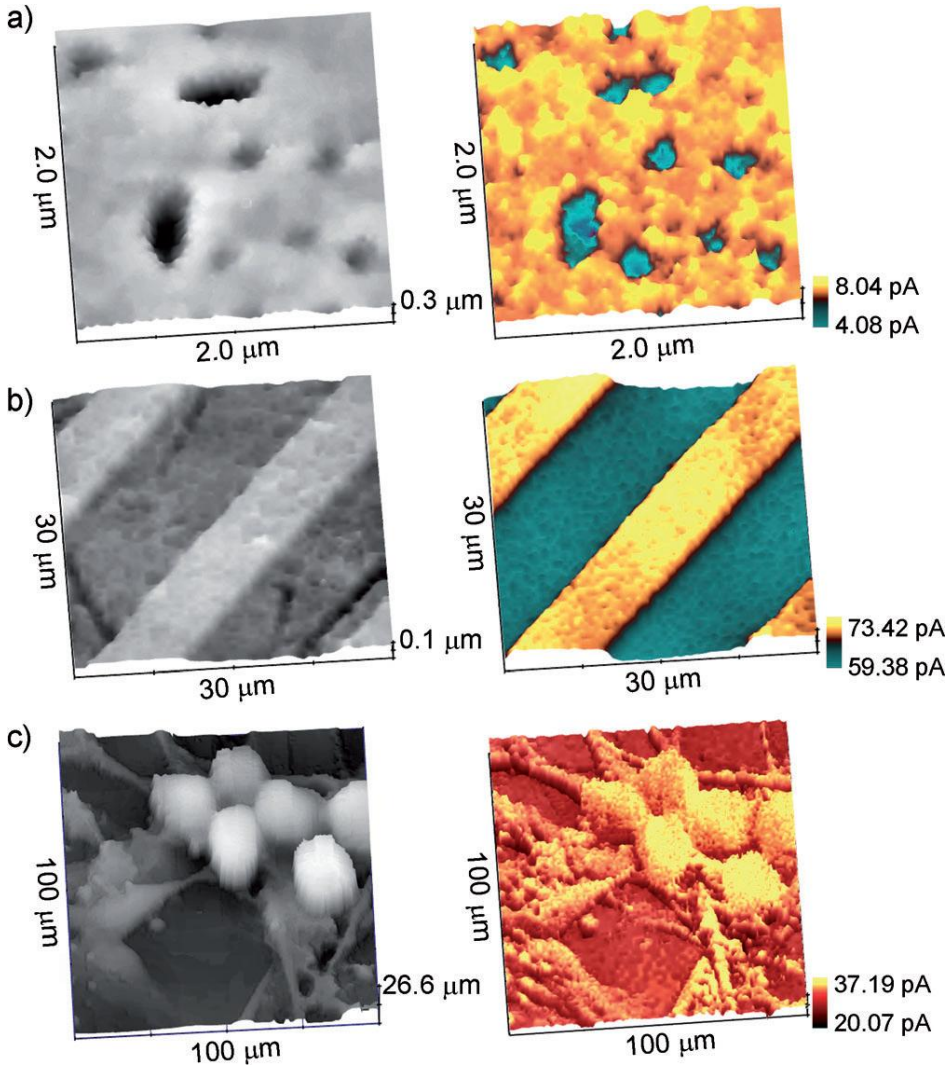

Figure 6-7: *Simultaneous topographical (left) and electrochemical (right) images. a) PET in 1 mM $FcCH_2OH$ in PBS. b) Pt interdigitated array in 1 m $FcCH_2OH$ in PBS. c) Living sensory neurons in 0.5 mm $FcCH_2OH$ in HBSS. The SECM and SICM electrodes were held at 500 and 200 mV versus a reference Ag/AgCl electrode, respectively. Electrochemical images were based on an oxidation current of $FcCH_2OH$.*[10]

6.4 Conclusions

In conclusion, a quick method for fabricating combined SECM – SICM probes of varied electrode radii, was developed. With this method nanoscale electrochemical imaging can be performed and in future functionalisation the carbon electrode will be explored, to allow for more varied and useful electrochemical detection of species. This is advantageous for use in life sciences being able to correlate electroactivity with topographical features giving a greater understanding on nanoscale biological processes, the probes can also be used to pierce cell membranes and possibly give insight to intracellular processes.

6.6 References:

(1) Amemiya, S.; Bard, A. J.; Fan, F. R. F.; Mirkin, M. V.; Unwin, P. R. In *Annual Review of Analytical Chemistry*; Annual Reviews: Palo Alto, 2008; Vol. 1, p 95.

(2) Dobson, P. S.; Weaver, J. M. R.; Holder, M. N.; Unwin, P. R.; Macpherson, J. V. *Anal. Chem.* **2005**, *77*, 424.

(3) Burt, D. P.; Wilson, N. R.; Weaver, J. M. R.; Dobson, P. S.; Macpherson, J. V. *Nano Lett.* **2005**, *5*, 639.

(4) Kueng, A.; Kranz, C.; Lugstein, A.; Bertagnolli, E.; Mizaikoff, B. *Angew. Chem.-Int. Edit.* **2005**, *44*, 3419.

(5) Gardner, C. E.; Unwin, P. R.; Macpherson, J. V. *Electrochem. Commun.* **2005**, *7*, 612.

(6) Hengstenberg, A.; Kranz, C.; Schuhmann, W. *Chem.-Eur. J.* **2000**, *6*, 1547.

(7) Takahashi, Y.; Shevchuk, A. I.; Novak, P.; Murakami, Y.; Shiku, H.; Korchev, Y. E.; Matsue, T. *J. Am. Chem. Soc.* **2010**, *132*, 10118.

(8) Comstock, D. J.; Elam, J. W.; Pellin, M. J.; Hersam, M. C. *Anal. Chem.* **2010**, *82*, 1270.

(9) Katemann, B. B.; Schuhmann, W. *Electroanalysis* **2002**, *14*, 22.

(10) Takahashi, Y.; Shevchuk, A. I.; Novak, P.; Zhang, Y.; Ebejer, N.; Macpherson, J. V.; Unwin, P. R.; Pollard, A. J.; Roy, D.; Clifford, C. A.; Shiku, H.; Matsue, T.; Klenerman, D.; Korchev, Y. E. *Angewandte Chemie International Edition* **2011**, *50*, 9638.

(11) Shao, Y. H.; Mirkin, M. V. *Anal. Chem.* **1998**, *70*, 3155.

(12) Amphlett, J. L.; Denuault, G. *J. Phys. Chem. B* **1998**, *102*, 9946.

(13) Novak, P.; Li, C.; Shevchuk, A. I.; Stepanyan, R.; Caldwell, M.; Hughes, S.; Smart, T. G.; Gorelik, J.; Ostanin, V. P.; Lab, M. J.; Moss, G. W. J.; Frolenkov, G. I.; Klenerman, D.; Korchev, Y. E. *Nature Methods* **2009**, *6*, 935.

CHAPTER 7

Conclusions

Electrochemical scanned probe microscopy techniques have been used to study a number of chemical and biological processes, with the most prominent one being SECM. Due to a lack of reliable distance control, it has been difficult to migrate to nanoscale electrodes and although various attempts have been made to incorporate positional feedback methodologies, they require specialist probes, as reviewed in Chapter 1.

This thesis has focussed on the development of SECCM, its proof of concept and its application. Chapter 2 highlighted all the equipment needed to develop and construct such a system, with detailed description on the hardware and the development of scanned probe control software. Chapter 3 provided a detailed description on the operation of the technique together with the response observed over model test substrates, including the development of a finite element model to quantify the observed response.

Chapter 4 focused on the understanding of the fundamental behaviour of CVD graphene as an electrode material. This study was of extreme importance, as until the nature of electron transfer at CVD grown graphene is fully understood, the development and optimisation of electrochemical devices cannot be achieved. With the use of a multimicroscopy approach, the studies showed how the electrochemical response evolved with the number of graphene layers and also the interlayer stacking. Using finite element modelling heterogeneous rate constants were assigned

to the number of layers within the ensemble. The results show that the electrochemical response increases with the number of layers, until the threshold for bulk graphite is reached, where the response becomes essentially reversible.

The fundamental electrochemical nature of SWNTs was determined in Chapter 5, by investigating two different morphologies, a 3D forest and a 2D network. In the first approach an SECCM probe was positioned carefully at both the SWNT ends and sidewalls of a SWNT forest, exhibiting a very similar electrochemical response. In the 2D network SECCM was used in an imaging mode using a 250 nm sized probe which was able to determine the individual contributions from both SWNT sidewalls, ends and crosspoints. Using finite element model a rate constant was assigned for the SWNTs using two different mediators, also comparing the response to a scenario where point defects would have been the sole contributors to the electrochemical current. The magnitude of the current and shape of an individual SWNT profile agreed with the case where the sidewall was electrochemically active, providing conclusive evidence that SWNT sidewalls undergo fast electron transfer making such an arrangement ideal for sensing applications.

Chapter 6 is a brief description of the fabrication of SECM-SICM probes. Probes were fabricated easily and cheaply within a couple of minutes and characterised using electrochemical techniques and also electron microscopy and Raman spectroscopy.